

# INAUGURAL – DISSERTATION

zur  
Erlangung der Doktorwürde  
der  
Naturwissenschaftlich-Mathematischen Gesamtfakultät  
der  
Ruprecht – Karls – Universität  
Heidelberg

vorgelegt von  
**Diplom-Physiker Andrés Chavarría Krauser**  
aus Mexiko-Stadt

Tag der mündlichen Prüfung:  
15.12.2006



# Thema

## Transport phenomena in plant-internal processes: growth and carbon dioxide transport

Gutachter:

**Herr Prof. Dr. Willi Jäger** (Universität Heidelberg)

**Herr Prof. Dr. Ulrich Schurr** (Forschungszentrum Jülich und Universität Düsseldorf)



# Transport phenomena in plant-internal processes: growth and carbon dioxide transport

## Summary

Aim of the here presented work was the quantitative modeling of plant-internal processes. Growth of cells and tissues was one of the central themes, although the lateral transport of carbon dioxide (CO<sub>2</sub>) was also treated. These processes depend strongly on fluxes of water, hormones and/or CO<sub>2</sub>. Thus, suitable transport equations were sought for to describe these processes.

Using the Lockhart-Equations, which are well known in biology to describe the growth of a whole cell, local formulations of energy and mass conservation were obtained. These formulations can be used to determine local growth patterns in cells. This was shown through a numerical example of a spherical cell. Finally, the conservation equations found, were shown to be consistent with the empirical Lockhart-Equations.

Plant organs, such as roots and hypocotyls, have spatial and temporal growth patterns. For example, the spatial distributions of growth in primary roots is given by a bell-shaped distribution along the organ axis. This particular one dimensional growth pattern was modeled here through the transport of two hypothetical phytohormones and using the Lockhart-Equations as the underlying growth equations. Because the hypothetical hormones were chosen to have auxin and cytokinin (two of the most important plant hormones) properties, the model stays in a plant physiological context.

Not only one dimensional growth patterns are found in roots and hypocotyls. These tend to have organ curvature and torsion, as becomes clear particularly in tropisms (e.g. gravitropism, hydrotropisms and phototropism). Although these processes are known for a long time in biology, no suitable measures to characterize the production of curvature and torsion have been defined. Using a curvature and torsion conservation equation, a measure for their production was found here. These measures were then exemplified in a simple model of the root gravitropic reaction, and applied in the characterization of the gravitropic reaction of *Arabidopsis thaliana* (L.) Heynh. wild-type and *pin3* mutant roots. The gravitropic reaction is believed to be regulated by the hormone auxin. *pin3* mutants are deficient in the PIN3 protein, which is essential in the transport of auxin in the root tip. Through comparison of the reaction of wild-type and *pin3* roots, it was shown here that the gravitropic reaction is not solely regulated by auxin, so that other regulation mechanisms need to exist.

Finally, transport equations were found, which describe the transport and assimilation of CO<sub>2</sub> in leaves. Using gas-exchange and chlorophyll fluorescence measurements, the homogenized lateral diffusion coefficient of leaves was determined. Moreover, the strategy behind the existence of lateral diffusion in leaves was discussed (plants differ in the porosity of their leaves).

Throughout the work presented here, it became clear how fructiferous the application of transport equations in biology is. The importance of a quantitative description in biology became also clear. Everyday new questions arise in biology. An answer to these may only be found using an interdisciplinary approach.

# Transportphänomene in pflanzeninternen Prozessen: Wachstum und Transport von Kohlendioxid

## Zusammenfassung

Ziel dieser Arbeit war die quantitative Modellierung von pflanzeninternen Prozessen. Die Modellierung des Wachstums von Zellen und Zellverbunden war eines der zentralen Themen der Arbeit, aber auch die Modellierung des lateralen Transports von Kohlendioxid ( $\text{CO}_2$ ) in Blättern wurde behandelt. Diese Prozesse werden in der Pflanze durch Wasser-, Hormon- bzw.  $\text{CO}_2$ -Transportflüsse geprägt, weshalb zur Modellierung passende Transportgleichungen gesucht wurden.

Basierend auf den in der Biologie wohlbekannten empirischen Lockhart-Gleichungen, die das Wachstum einer gesamteten Zelle beschreiben, wurden Energie- und Masseerhaltungsgleichungen gewonnen, mit denen lokale Wachstumsmuster in einer Zelle bestimmt werden können. Diese Gleichungen wurden dann exemplarisch für eine sphärische Zelle numerisch gelöst und die gefundenen Muster diskutiert. Anschließend wurde gezeigt, dass diese Gleichungen tatsächlich eine konsistente Erweiterung der Lockhart-Gleichungen darstellen.

Pflanzenorgane, wie Wurzeln und Hypokotyle, weisen räumliche und zeitliche Wachstumsmuster auf. So ist z.B. die örtliche Verteilung von Wachstum in Wurzelspitzen von einer glockenförmigen Verteilung entlang des Organs geprägt. Dieses eindimensionale Wachstumsmuster wurde hier anhand des Transports von zwei hypothetischen Phytohormonen und der Lockhart-Gleichungen beschrieben. Diesen hypothetischen Hormonen wurden Auxin- und Cytokinin-ähnliche Eigenschaften gegeben (zwei der wichtigsten Pflanzenhormone), womit das Modell einen pflanzenphysiologischen Bezug behält.

Wurzeln und Hypocotyle weisen nicht nur eindimensionale Wachstumsmuster auf, sondern können Krümmungs- und Windungsprozesse aufweisen, wie im Falle von Tropismen (Gravi-, Hydro- und Phototropismus). Obwohl diese Prozesse schon lange in der Biologie bekannt sind, gibt es keine zufriedenstellenden Maße zur Charakterisierung ihrer Produktion. Anhand einer Krümmungs- und Windungserhaltungsgleichung wurden hier solche Maße bestimmt und exemplarisch an einem einfachen Modell der gravitropen Reaktion von Wurzelspitzen getestet. Daraufhin wurde dieses Maß verwendet, um die Gravitropismus-Reaktion von *Arabidopsis thaliana* (L.) Heynh. Wurzeln (Wildtyp und *pin3* Mutanten) zu charakterisieren. Das gängige biologische Modell der gravitropen Reaktion von Wurzeln geht davon aus, dass diese vom Pflanzenhormon Auxin reguliert wird. *pin3* Mutanten produzieren das für den Auxintransport wichtige Protein PIN3 nicht. Damit gelang es hier zu zeigen, dass die Reaktion nicht nur ausschließlich von Auxin reguliert wird, sondern auch andere Regulationsmechanismen vorhanden sind.

Abschließend wurden Transportgleichungen zur Beschreibung des Transportes und der Bindung von  $\text{CO}_2$  in Blättern aufgestellt. Anhand von Gaswechsel- und Chlorophyllfluoreszenzmessungen wurden dann der laterale homogenisierte Diffusionskoeffizient in Blätter bestimmt und die Vorteile von lateraler Diffusion für das Blatt diskutiert.

Im Allgemeinen zeigt sich, wie fruchtbar die Anwendung von Transportgleichungen in der Biologie ist. Vor allem wird aber klar, wie notwendig eine quantitative Beschreibung in der Biologie geworden ist. Tagtäglich entstehen neue Fragestellungen, die einen interdisziplinären Ansatz bedürfen.

# Preface

*All movement is accomplished in six stages,  
And the seventh brings return  
The seven is the number of the young light  
It forms when darkness is increased by one*

Syd Barrett, 1967

The purpose of this manuscript is to present the use of transport equations in models of plant-internal processes and to point out possible future applications of this concept. The manuscript is focused mostly on cell and root growth, although an application in CO<sub>2</sub> transport is also presented. Chapter 1 gives a short introduction into transport equations and why these are important in plant biology. Chapter 2 presents an application of a binary-mixture transport equation to model cell growth and to obtain subcellular growth patterns. In Chapter 3 a model of growing root tips, controlled by the transport of two phytohormones, is assembled. Chapter 4 presents a new measure of curvature production in curving organs and a simple model of the gravitropic reaction of roots. These findings are then applied in Chapter 5 to characterize the gravitropic reaction of *Arabidopsis thaliana* (L.) Heynh. roots. This reaction is believed to be mediated by transport patterns of the phytohormone *auxin*, so that Chapter 5 can be understood as a sound basis for future modeling of the gravitropic reaction using transport equations. Chapter 6 applies a simple CO<sub>2</sub> transport equation to determine the effect of lateral diffusion on heterogeneous photosynthetic assimilation patterns in leaves. And at last, Chapter 7 presents some conclusions and perspectives found throughout this manuscript.

The author wishes to thank Prof. Willi Jäger (Universität Heidelberg) and Prof. Ulrich Schurr (Forschungszentrum Jülich and Universität Düsseldorf) for making it possible to work on this manuscript. I also would like to thank heartily all the members of the *Growth Group* of the ICG-III (Forschungszentrum Jülich). I wish to thank in particular Kerstin Nagel and Roland Pieruschka for helping me with their excellent experimental skills, and Maja Christ for being there when I needed moral support.

Jülich, Germany  
April 2006

Andrés Chavarría Krauser



# Contents

<b>1</b>	<b>Introduction</b>	<b>1</b>
<b>2</b>	<b>Cell Growth Model</b>	<b>3</b>
2.1	Introduction . . . . .	3
2.1.1	Cell proliferation and growth . . . . .	4
2.1.2	Measure of growth . . . . .	4
2.1.3	Wall extension and water uptake . . . . .	5
2.2	Modeling cell growth . . . . .	7
2.2.1	Mass conservation . . . . .	7
2.2.2	Energy conservation . . . . .	19
2.2.3	Simplifications . . . . .	22
<b>3</b>	<b>Root Growth Model</b>	<b>23</b>
3.1	Introduction . . . . .	23
3.2	Biophysical equations . . . . .	26
3.2.1	Approximations . . . . .	27
3.2.2	Osmotic potential $\psi_s$ . . . . .	28
3.2.3	Wall extensibility $\phi$ . . . . .	29
3.2.4	Phytohormone transport . . . . .	30
3.2.5	Cell division . . . . .	36
3.2.6	Assembling the model . . . . .	37
3.3	Simulation, results and discussion . . . . .	39
3.3.1	Growth distribution and cell properties . . . . .	39
3.3.2	Auxin change . . . . .	45
3.3.3	Conclusion . . . . .	48
<b>4</b>	<b>Curvature Phenomena</b>	<b>49</b>
4.1	Introduction . . . . .	49
4.2	Curvature production in $\mathbb{R}^2$ . . . . .	50
4.3	Differential growth in $\mathbb{R}^2$ . . . . .	52
4.4	Curvature in $\mathbb{R}^3$ . . . . .	54

<b>5</b>	<b>Root Gravitropism</b>	<b>61</b>
5.1	Introduction . . . . .	61
5.2	Advances in curvature analysis . . . . .	64
5.2.1	Calculation of spatio-temporal distributions . . . . .	65
5.2.2	Relative elemental growth rate . . . . .	66
5.2.3	Differential growth curvature rate . . . . .	67
5.2.4	Denoising of spatio-temporal distributions . . . . .	67
5.2.5	Normalization and averaging of distributions . . . . .	68
5.3	Characterization of root gravitropism . . . . .	69
5.3.1	Kinetics of growth and curvature . . . . .	69
5.3.2	Discussion . . . . .	77
<b>6</b>	<b>Lateral CO<sub>2</sub> Diffusion Inside Leaves</b>	<b>79</b>
6.1	Introduction . . . . .	79
6.2	Calibration model . . . . .	81
6.3	Lateral diffusion model . . . . .	82
6.4	Diffusion coefficients from concentration profiles . . . . .	85
6.5	Lateral diffusion effect . . . . .	86
<b>7</b>	<b>Concluding remarks and perspectives</b>	<b>91</b>

# List of Figures

2.1	Plant cell scheme . . . . .	4
2.2	Cell model domain . . . . .	8
2.3	Loose cell turgor recovery: $Y_C$ . . . . .	13
2.4	Loose cell turgor recovery: $RGR$ . . . . .	14
2.5	Stiff cell turgor recovery: $Y_C$ . . . . .	15
2.6	Stiff cell turgor recovery: $RGR$ . . . . .	16
2.7	Cell turgor recovery . . . . .	17
3.1	$REGR$ distribution along roots . . . . .	24
3.2	Root tip . . . . .	24
3.3	Scheme of auxin and cytokinin transport equations . . . . .	30
3.4	Velocity and $REGR$ distributions . . . . .	39
3.5	Hormone distribution . . . . .	42
3.6	Turgor, cell length distribution . . . . .	42
3.7	Transition positions . . . . .	43
3.8	Root tip's velocity . . . . .	43
3.9	Wall extensibility and velocity evolution . . . . .	46
3.10	Cell length and osmotic potential evolution . . . . .	46
3.11	Auxin increase . . . . .	47
3.12	Transitions upon auxin increase . . . . .	47
4.1	Growing and curving cylindrical organ . . . . .	49
4.2	Curved cylindrical organ scheme . . . . .	53
4.3	Root growth and model of gravitropism motors . . . . .	56
4.4	Simulation of $\kappa$ , $d_t\kappa$ and $DGCR$ . . . . .	59
5.1	Fountain model of auxin transport . . . . .	62
5.2	Curvature kinetics of roots . . . . .	62
5.3	Curvature analysis denoise . . . . .	67
5.4	Curvature angle . . . . .	70
5.5	Root tip velocity . . . . .	71
5.6	Angular velocity . . . . .	71
5.7	$REGR$ distribution . . . . .	72
5.8	$DGCR$ distribution . . . . .	72

5.9	Spatio-temporal distributions . . . . .	75
5.10	<i>REGR</i> and gravitropism motors . . . . .	76
6.1	Homo- and heterobaric leaves . . . . .	80
6.2	Calibration model . . . . .	80
6.3	Chlorophyll fluorescence imaging . . . . .	81
6.4	CO <sub>2</sub> diffusion model . . . . .	83
6.5	Fitting results . . . . .	85
6.6	CO <sub>2</sub> diffusion effect . . . . .	87
6.7	$D'$ vs. $\Delta K$ . . . . .	89

# Abbreviations and Definitions

$\chi_A$  indicator function of set  $A$ , i.e.  $\chi_A(x) = 1$  for  $x \in A$ , zero elsewhere., page 83

$\partial_t \circ$  partial time derivative  $\frac{\partial}{\partial t} \circ$ , page 5

$DGCR$  differential growth curvature rate, page 52 and, page 52

$DGTR$  differential growth torsion rate, page 55

$\text{div } \circ$  divergence operator,  $\text{div } \circ = \nabla \cdot \circ$ , page 5

$d_t \circ$  total time derivative  $\frac{d}{dt} \circ = \partial_t \circ + \mathbf{v} \cdot \nabla \circ$ , page 5

$D_t$  material derivative, page 10

$\mathcal{F}$  diffusion flux, page 8

$\mathcal{V}$  species diffusion velocity, page 9

$\Gamma(t)$  boundary of  $\Omega(t)$ , page 10

$\Delta_d \circ$  discrete Laplace operator.  $\Delta_d \circ := \nabla_d^+ \nabla_d^- \circ = (\circ_{k+1} - 2 \circ_k + \circ_{k-1})/l_k^2$ , page 31

$\mathcal{C}^0(X, Y)$  set of all continuous functions from vector space  $X$  to vector space  $Y$ , page 26

$\mathcal{C}^2(X, Y)$  set of all two times continuously differentiable mappings from the vector space  $X$  to the vector space  $Y$ , page 50

$\nabla \circ$  Nabla operator, page 9

$\nabla_d^\pm \circ$  forward (+) and backward (-) difference operators.  $\nabla_d^\pm \circ := \pm(\circ_{k\pm 1} - \circ_k)/l_k$ , page 31

$\Omega(t)$  time dependent domain, page 7

$O(\varepsilon)$  terms of order  $\varepsilon$ , page 27

$\overline{\Omega}(t)$  closure of  $\Omega(t)$ , page 10

- $\phi$  wall extensibility ( $MPa h^{-1}$ ), page 6
- $\psi_s$  osmotic potential ( $MPa$ ), page 6
- $\rho$  total density, page 8
- $\varepsilon$  strain tensor, page 20
- $\sigma$  stress tensor, page 20
- $\eta$  viscosity tensor, page 21
- $\mathbf{A} : \mathbf{B}$  is defined as  $\mathbf{A} : \mathbf{B} = \sum_{i,j} A_{ij} B_{ij}$ , page 20
- $\theta(x)$  Heaviside function, defined as  $\theta(x) = 1$  for  $x \geq 0$  and  $\theta(x) = 0$  else., page 38
- $\varphi(s(t), t)$  sufficiently differentiable curve in  $\mathbb{R}^3$ , i.e.  $\varphi \in \mathcal{C}^2(\mathbb{R} \times \mathbb{R}, \mathbb{R}^3)$ , page 50
- $\mathbf{n}$  normal vector of boundary  $\Gamma(t)$ , page 10
- $\mathbf{u}$  displacement vector, page 20
- $\mathbf{v}$  mass average flow velocity, page 8
- $B_r(x)$  ball of radius  $r \in \mathbb{R}^+$  around  $x \in \mathbb{R}^n$ , page 18
- $c_\alpha$  species molar concentrations,  $c_\alpha = \frac{\rho_\alpha}{m_\alpha}$ , where  $\alpha \in S$ , page 26
- $C_i$   $\text{CO}_2$  partial pressure inside leaf, page 81
- $D^{ap}$  apparent diffusion coefficient, page 9
- $L_p$  water conductivity coefficient ( $m h^{-1} MPa^{-1}$ ), page 6
- $m_k$  molar weight of the  $k$ -th species, page 8
- $p$  turgor pressure ( $MPa$ ), page 3
- $REGR$  relative elemental growth rate ( $\% h^{-1}$ ), page 5
- $RGR$  relative growth rate ( $\% h^{-1}$ ), page 5
- $S$  set of species indexes, page 8
- $Y$  yield threshold ( $MPa$ ), page 6
- $Y_k$  species mass fraction,  $k \in S$ , page 8
- Phloem* living vascular tissue mainly for transport of sugars, page 1
- Xylem* dead vascular tissue mainly for water and inorganic ion transport, page 1

*ABBREVIATIONS AND DEFINITIONS*

vii

AUX proteins involved in cellular influx of auxin, page 32

IAA Indole-3-acetic-acid, the most relevant auxin., page 41

PIN proteins involved in cellular efflux of auxin, page 32

PIN3 auxin efflux facilitator of the PIN family proteins., page 61

RubisCO D-Ribulose-1,5-bisphosphate-Carboxilase/Oxygenase, page 82



# Chapter 1

## Introduction

Transport equations have an established position in engineering models, such as in combustion problems, pollutant distribution, (chemical)-reactor modeling and many more. However, biological systems have not been treated as thorough and experience recently more attention. In plant biology, reaction-diffusion systems are enjoying recent interest (e.g. Chavarría-Krauser and Schurr 2004; Roussel and Roussel 2004; Chavarría-Krauser et al. 2005; Swarup et al. 2005; Galloët and Herbin 2005; Prusinkiewicz and Rolland-Lagan 2006; and many more). In future, transport equations will have even a more important role in *Plant Physiology* and *Molecular Biology*.

Biological systems, either cells or tissues, can be treated as porous media in which flow, reaction and diffusion occurs. Cell walls and membranes have a complex structure full of either non-tightly packed microstructures or specialized transport channels. Thousands of compounds travel in the symplast and apoplast<sup>1</sup>, including signal relevant phytohormones. Hence, plant development and function are determined essentially by these processes. Actually, many plant processes, such as photosynthesis and growth, rely on specialized transport systems (xylem and phloem transport, but also polar auxin transport). Already with the first multicellular plants transport systems had to be established.

The manuscript presented here aims at demonstrating application of transport equations on plant growth and photosynthesis related gas transport. The set of equations applied here can be generalized as species conservation equations (Giovangigli 1999)

$$\partial_t \rho_k + \operatorname{div}(\rho_k \mathbf{v}) + \operatorname{div} \mathcal{F}_k = m_k \omega_k, \quad k \in S \quad (1.1)$$

where  $\rho_k$  is the mass density of the k-th species,  $\mathbf{v}$  is the mass average flow velocity,  $\mathcal{F}_k$  is the diffusion flux of the k-th species,  $m_k$  is the molar mass of the k-th

---

<sup>1</sup>Apoplast: the medium outside a cell membrane, e.g. the whole cell wall structure of a tissue. Symplast: the cell's inside.

species,  $\omega_k$  is the molar production rate of the  $k$ -th species,  $S$  is the set of species. Depending on the treated problem, several simplifications of (1.1) are used. For example, Fick's empirical law for the diffusion flux is a frequent approximation

$$\mathcal{F}_k = -\rho D_k^{app} \nabla Y_k, \quad k \in S, \quad (1.2)$$

where  $\rho$  is the total density,  $D_k^{app}$  is the apparent diffusion coefficient of the  $k$ -th species,  $Y_k$  is the  $k$ -th species mass fraction. However, the treatment of some cases needs a more complex diffusion flux than (1.2), such as in polar auxin transport (Chapter 3).

The chemical reaction terms  $m_k \omega_k$ , where  $k \in S$ , need also to be adapted to the biological problem. Because not necessarily all species and reactions are known or want to be modelled, the set of species  $S$  is reduced to a minimum. Hence, production rates may become functions of the species concentration, e.g. in CO<sub>2</sub> assimilation (Chapter 6). Eq. (1.1) will not always be used here in the strict sense of species conservation. For example, in Chapter 4 a measure of curvature production in curving organs is sought for, and based on a curvature conservation equation.

Mathematical modeling of plant processes should always evolve hand in hand with biological models. This implies the use of physiological parameters to allow a clear and straightforward interpretation. Integration of mathematical and biological models is challenging. The work presented here should be thus understood as a basis for further developments.

# Chapter 2

## Cell Growth Model

### 2.1 Introduction

All plant tissues consist of cells. It is thus not astonishing that growth and development of a tissue is given by growth and divisions of single cells. To understand tissue growth, it is essential to have a clear picture of the cell structure. We will see below, that the cell structure determines how cells grow.

Plant cells differ substantially from animal cells. Probably the most outstanding differences are the presence of cell walls, vacuoles and plastides (Fig. 2.1 A). Cell walls supply rigidity and are composed mostly of cellulose microfibrills interconnected by xyloglucan and arabinogalactan molecules (Lüttge and Kluge, 2002). This microstructure of the cell wall results in a complicated mechanical behavior of cell walls (Cosgrove 1992; Niklas 1992). Vacuoles compose up to 90% of the volume of mature cells, and are mainly inorganic salts in water. The high osmolarity of the salts produces a high osmotic pressure inside vacuoles. Here one of the largest differences between plant and animal cells becomes clear, plant cells have a high internal pressure denominated *turgor* (Fig. 2.1 B). The turgor of cells assumes normally values between 0.1 *MPa* and 1 *MPa*.<sup>1</sup> This high pressure is possible due to the rigid cell wall surrounding the cell. Beside the cell wall, the pressurized vacuoles are perhaps one of the most important agents in cell expansion. There are several types of plastides in plant cells, the most characteristic ones for plants are chloroplasts, which are responsible for photosynthesis. Another type of plastides are the amyloplasts, found mainly in non-photosynthetic tissues, such as roots. These are used for starch storage and play an important role as sedimentation bodies in root gravitropism.

---

<sup>1</sup>1 *MPa* is approximately 10 *bar*.

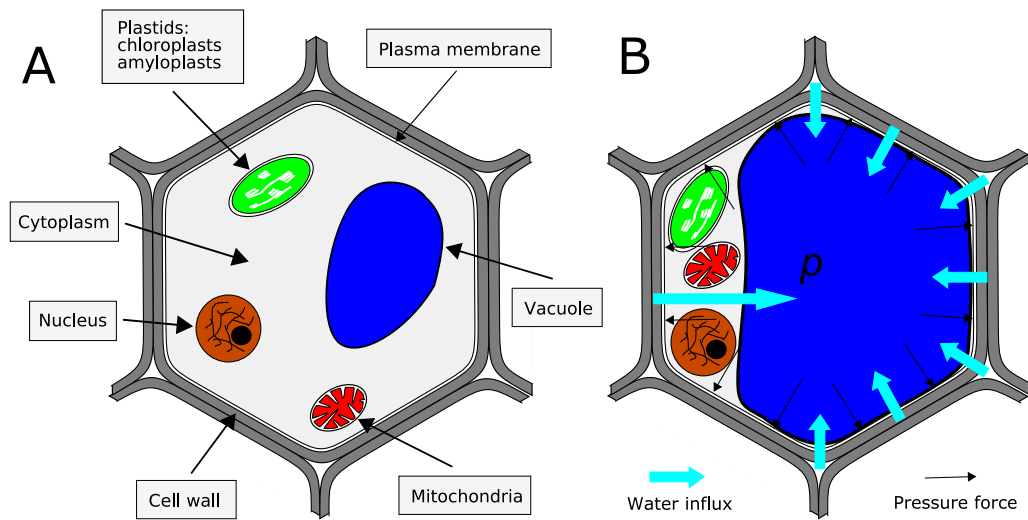


**Figure 2.1:** A, Simplified scheme of a plant cell. B, Water influx and turgor pressure  $p$  build-up in cell.

### 2.1.1 Cell proliferation and growth

Tissues develop through the coordinated interplay of two processes: cell expansion and cell division (Beemster et al. 2003; del Pozo et al. 2005). However, tissues do not have to be packed densely and may have intercellular spaces, which may compose a substantial part of the tissue volume (e.g. leaves, refer to Chapter 6). Depending on the tissue, age and position, one or the other may dominate. Division of plant cells is similar to the division of animal cells. However, in plant cells the primary cell wall has to be synthesized between the duplicated nuclei (Lüttge and Kluge 2002), so that a high polarity of cell division is found. Roots show in particular a strong polarity in cell division, as most divisions occur in the plane perpendicular to the root axis<sup>2</sup> (Fig. 3.2 page 24). Cell division is coupled to growth, else the dividing cells would constantly lose size. Young cells have small vacuoles, so that cytoplasm composes most of their volume (Fig. 2.1 A). Thus, growth due to cell proliferation is mainly due to cytoplasm production, in contrast to cell expansion, which occurs mainly due to water and salt/nutrient uptake of the vacuole (Fig. 2.1 B; Brumfield 1942).

### 2.1.2 Measure of growth

Several measures have been used to characterize growth in biology: absolute change in length or area, rate of change of length or area and the relative growth

<sup>2</sup>Divisions parallel to the root axis are found in the apical meristem and are the basis of the different cell lineages.

rate (*RGR*). However, the *RGR* has been the most fructiferous in the characterization of leaf and root growth (e.g. Erickson and Sax 1956; Pritchard et al. 1993; Schmundt et al. 1998; Walter et al. 2002), and is from a mathematical point of view the most reasonable. Moreover, a thermodynamic approach to elucidation of the cell wall expansion rate, has shown that the *RGR* is independent of cell dimension (Section 2.2; Veytsman and Cosgrove 1998). The *RGR* is defined as follows

$$RGR = \frac{1}{J} \partial_t J = \partial_t \ln J \quad (2.1)$$

where  $J$  is a measure, e.g. cell length, area or volume. Roots and hypocotyls grow almost unidirectional, therefore the cell length is used for characterization of their growth, while leaves expand areally, so that the area is suited better. This definition of *RGR* allows a very simple average method, because the *RGR* is given by a total derivative:

$$\overline{RGR} = \frac{1}{T} \int_0^T RGR dt = \frac{1}{T} \ln \left( \frac{J(T)}{J(0)} \right) . \quad (2.2)$$

Eq. (2.1) can be generalized into  $n$ -dimensions. Assuming that growth is a flow generated by the vector field  $\mathbf{v}(\mathbf{x}, t) : \mathbb{R}^n \times \mathbb{R} \mapsto \mathbb{R}^n$ , i.e.  $d_t \mathbf{x} = \mathbf{v}(\mathbf{x}, t)$ , the *RGR* can be related to the divergence of the vector field:

$$RGR = \partial_t \ln J = \operatorname{div} \mathbf{v} , \quad (2.3)$$

This was probably shown more than 150 years ago by either L. Euler or J. L. Lagrange and is equivalent to the equation of continuity for a measure-preserving flow (Gerlich 1991).

In the biological literature a distinction between relative elemental growth rate *REGR* and relative growth rate *RGR* is done. These differ in the dimension of the vector field they work on, *REGR* is used in 1D while *RGR* is used in 2D and 3D. Throughout the work presented here we will not follow this convention strictly, as the definition in Eq. (2.3) does not depend on the dimension and a distinction seems unnecessary.

### 2.1.3 Wall extension and water uptake

In the last decade new insight into cell wall extension was gained (see e.g. Pritchard 1994; Cosgrove 2000). Several controlling factors have been found, e.g. the wall proteins *expansins*, but the complete mechanism and control mechanisms of wall extension are still unknown. It is up to date unclear how cells can extend tenfold or more without their wall losing stability. The general accepted model of cell wall expansion is that extension occurs through wall loosening and confirmed cell

wall production – otherwise cell walls would become thinner with expansion. The osmotic pressure in the cell produces a tension on the wall (Fig. 2.1 B). A creeping condition is then achieved through cell wall yielding (Lockhart 1965; Cosgrove 1986; Cosgrove 2000).

Extension growth is composed of two overlaying processes: water uptake and cell wall yielding. While turgor  $p$  is increased by water uptake, cell wall yielding tends to decrease it. It becomes evident, that depending on the water influx and cell wall yielding, a certain  $p$  is established in the cell (Fig. 2.1 B).

Lockhart (1965) proposed the following empirical equation for the elongation rate of cells

$$d_t l = l \phi (p - Y) , \quad (2.4)$$

where  $l$  is the cell length,  $\phi$  is the wall extensibility and  $Y$  is the yield threshold. Many measurements support Eq. (2.4), although some do not. See Cosgrove (1992) for a discussion on this issue. The discrepancies may be due to the varying interpretation of growth rate and to different measurement methods. Pritchard et al. (1990) and Pritchard (1994) showed that growth of a root section fulfills Eq. (2.4).

The cell can be described as a simple osmometer, water uptake is then given by

$$d_t V_{ol} = -A_s L_p (\psi_s + p) , \quad (2.5)$$

where  $V_{ol}$  is the volume of the cell,  $A_s$  is the area of the cell surface,  $L_p$  is the conductivity coefficient and  $\psi_s$  is the osmotic potential (see Lockhart 1965; Cosgrove 1986; Cosgrove 1993; Nobel 1999).

For simple cell geometries, e.g. cylindrical, both Eqs. (2.4) and (2.5) can be related. A cylindrical cell of base area  $a_0$ , perimeter  $a_1$  and length  $l$ , has the volume and surface area

$$V_{ol} = a_0 l \quad (2.6)$$

$$A_s = 2 a_0 + a_1 l . \quad (2.7)$$

From Eqs. (2.4) to (2.7), an expression for the “working” turgor is found

$$p = \frac{V_{ol} \phi Y - A_s L_p \psi_s}{V_{ol} \phi + A_s L_p} . \quad (2.8)$$

Lockhart (1965) and Cosgrove (1986) found similar expressions. If we solve Eq. (2.5) for turgor pressure, insert it into Eq. (2.4) and use Eqs. (2.6) and (2.7), an expression for the growth rate can be calculated

$$d_t l = -\frac{A_s L_p l \phi (\psi_s + Y)}{V_{ol} \phi + A_s L_p}. \quad (2.9)$$

Eq. (2.9) shows that the elongation of a cylindrical cell depends directly on the osmotic potential and the yield threshold, but not on the turgor. As mentioned before, the turgor assumes a certain value for given extensibility  $\phi$  and water conductivity  $L_p$  [Eq. (2.8)]. As in the case of the pressure in fluid dynamics, which is a separation variable between the momentum and the mass conservation equations (Landau and Lifschitz 1991b), the turgor is the separation variable between the “mass” conservation Eq. (2.5) and the “momentum” conservation Eq. (2.4).

Cells in a tissue are interconnected with a pectinuous layer, and can thus not slide against each other. The wall of a mature cell is composed of three mayor layers: primary, secondary and tertiary cell wall (Lüttge and Kluge 2002). Each of these layers is composed by themself of countless thin layers of cellulose and different incrustations. Throughout the extension process, new cellulose material is deposited continuously on the inner side of the wall, so that the outmost layers are simultaneously the oldest (Niklas 1992). The orientation of the microfibrills determines the direction of growth. These change during expansion their orientation angle, which becomes shallower relative to the cell axis during maturation (Pritchard et al. 1993). Here again a strong polarity of cell growth is found. Altogether, we conclude that Eqs. (2.8) and (2.9) can only be rough approximations of cell growth.

## 2.2 Modeling cell growth

In Section 2.1 we saw that growth of a cell can be described by two equations, one representing the mass conservation and the other the momentum or energy conservation [Eqs. (2.4) and (2.5)]. We would like to derive here local expressions of these equations.

### 2.2.1 Mass conservation

The simplified cell model used in this section is given by a cell inside  $\Omega(t)$  and a cell wall  $\Omega_w(t)$  that includes the plasma membrane (Fig. 2.2). In this section we present the conservation equations and boundary conditions involved in water uptake of cells. In Section 2.2.3 we will show that these equations simplify into the well known osmometer equations proposed by Lockhart 1965.

### Species conservation

The conservation of non-reactive species is expressed by the set of equations (Giovangigli 1999)

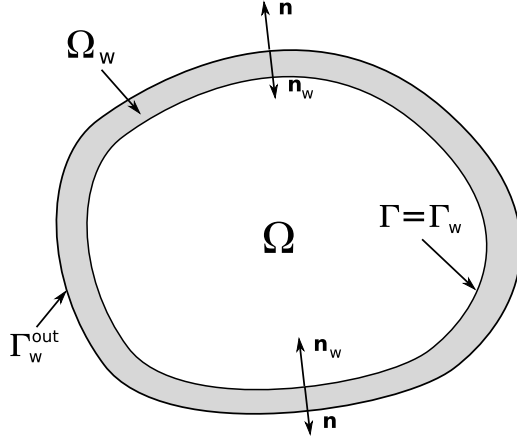


**Figure 2.2:** Simple cell model.  $\Omega$  composes the cell inside and  $\Omega_w$  the cell wall. The boundaries,  $\Gamma = \Gamma_w$  and  $\Gamma_w^{out}$ , and the corresponding normal vectors  $\mathbf{n} = -\mathbf{n}_w$  are shown.

$$\partial_t \rho_k + \operatorname{div}(\rho_k \mathbf{v}) + \operatorname{div} \mathcal{F}_k = 0 \quad (2.10)$$

where  $k \in S$ ,  $\rho_k$  is the mass density of the  $k$ -th species,  $\mathbf{v}$  is the mass average flow velocity,  $\mathcal{F}_k$  is the diffusion flux of the  $k$ -th species and  $S$  is the set of species. Instead of the mass density, the species mass fractions

$$Y_k = \frac{\rho_k}{\rho}, \quad k \in S,$$

can be used. These satisfy the relation  $\sum_{k \in S} Y_k = 1$ , which follows from the definition of the total density

$$\rho = \sum_{k \in S} \rho_k.$$

The mole fractions are also used to describe the distribution of species

$$X_k = \frac{\bar{m}}{m_k} Y_k, \quad k \in S,$$

where  $\bar{m}$  is the average molar weight of the mixture and  $m_k$  is the molar weight of the  $k$ -th species.

Summation of all species conservation equations (2.10) delivers, using the mass constraint (Giovangigli 1999)

$$\sum_{k \in S} \mathcal{F}_k = 0, \quad k \in S, \quad (2.11)$$

the total density  $\rho$  conservation equation

$$\partial_t \rho + \operatorname{div}(\rho \mathbf{v}) = 0. \quad (2.12)$$

The diffusion flux  $\mathcal{F}_k$  of the  $k$ -th species, in absence of large temperature gradients, is given by

$$\mathcal{F}_k = - \sum_{l \in S} C_{kl} \mathbf{d}_l, \quad k \in S \quad (2.13)$$

where  $C_{kl}$ ,  $k, l \in S$  are the multicomponent flux diffusion coefficients,  $\mathbf{d}_k$  is the diffusion driving force of the  $k$ -th species

$$\mathbf{d}_k = \nabla (X_k) + (X_k - Y_k) \nabla \ln p, \quad k \in S. \quad (2.14)$$

Eq. (2.14) is valid only when external forces, if at all present, act equivalently on all species. The diffusion flux can be used to define a species diffusion velocity

$$\mathbf{v}_k = \frac{\mathcal{F}_k}{\rho_k}, \quad k \in S. \quad (2.15)$$

These obey, similarly to the  $\mathcal{F}_k$ s, a mass conservation constraint

$$\rho \mathbf{v} = \sum_{k \in S} \rho_k \mathbf{v}_k = \sum_{k \in S} \mathcal{F}_k = 0,$$

which means that diffusion does not produce a mass average flow velocity.

### Water uptake

The diffusion forces (2.13) can be simplified considerably by considering the structure of the cell. Inside the cell  $\Omega(t)$  the pressure gradient can be assumed to be small, as it would produce a flow of a viscous fluid and would decrease in strength promptly. This means that in  $\Omega(t)$  local growth can be assumed to be mostly driven by concentration gradients. Note that this is only a rough approximation. A *cytoplasmic flow* is present in cells. This flow is particularly evident and strong in cells of the *Chara* algae, in which a velocity of up to  $5 \text{ cm h}^{-1}$  is found. This flow occurs, however, in the cytoplasm and not in the vacuole and can thus be neglected. In the cell wall/membrane  $\Omega_w(t)$  the pressure gradients can assume considerable values (pressure outside  $0.1 \text{ MPa}$ , inside  $0.5$  to  $1 \text{ MPa}$ ), so that these two cases must be treated separately.

### Cell inside

We approximate the solution in the vacuole as a binary mixture of water  $W$  and an osmotically active compound  $C$  (i.e.  $S = \{W, C\}$ ). The diffusion velocities can be approximated by Fick's empirical law (Giovangigli 1999)

$$\mathcal{F}_k = \rho_k \mathbf{v}_k = -\rho D_k^{ap} \nabla Y_k, \quad k \in S = \{W, C\}, \quad (2.16)$$

where  $D_k^{ap}$  denotes the apparent diffusion coefficient of the  $k$ -th species. The diffusion coefficients are not independent, because the fluxes have to fulfill the mass constraint (2.11). A simple calculation based on  $Y_W + Y_C = 1$  shows that

$$D := D_W^{ap} = D_C^{ap}. \quad (2.17)$$

Only one conservation equation is needed to describe the problem in  $\Omega(t)$ , as the mass fraction of e.g. the water can be determined through  $Y_W = 1 - Y_C$ . The effect of water inflow is then taken into account through suitable boundary conditions applied to the compound's problem.

Taking in mind that inside the cell no pressure gradient is present and that pure diffusion does not produce an average mass flow velocity ( $\mathbf{v} = \mathbf{V} = 0$ ), the transport term in Eq. (2.10) is zero. Using the continuity equation (2.12) and  $\mathbf{v} = 0$ , a short calculation shows that the density does not depend on time, i.e. it is only a function of the spatial coordinates. We assume here that no initial gradient in density was present, i.e.  $\rho = \text{const}$ . The species conservation simplifies substantially

$$\partial_t Y_C - D \Delta Y_C = 0, \quad \text{in } \Omega(t), \quad (2.18)$$

where  $D = \text{const}$  and Fick's law (2.16) were used. We have to mention here that, although the problem assumed a simple form of a diffusion equation, it is posed on the time dependent domain  $\Omega(t)$ . This difficulty can be by treated by introducing material coordinates.

We introduce the material velocity  $\mathbf{v}_b$  defined in  $\bar{\Omega}(t)$ , and choose it so that it corresponds on  $\Gamma(t)$  to the velocity of the boundary. Applying mass conservation on the boundary, an expression for the boundary velocity is found

$$\rho \mathbf{v}_b \cdot \mathbf{n} = -\mathbf{j}_W^{in} \cdot \mathbf{n}, \quad \text{on } \Gamma(t),$$

where  $\mathbf{j}_W^{in}$  is the water flux into the cell and  $\mathbf{n}$  is the normal vector of  $\Omega(t)$  boundary. To obtain an expression of  $\mathbf{v}_b$  in  $\Omega(t)$ , we use

$$\mathbf{j}_W^{in} \cdot \mathbf{n} = \mathcal{F}_W \cdot \mathbf{n} = -\mathcal{F}_C \cdot \mathbf{n} = \rho D \nabla Y_C \cdot \mathbf{n}, \quad \text{on } \Gamma(t). \quad (2.19)$$

and define the material velocity in  $\bar{\Omega}(t)$  as

$$\mathbf{v}_b := -D \nabla Y_C = Y_C \mathbf{V}_C. \quad (2.20)$$

This allows to define a suitable material derivative

$$D_t \circ := \partial_t \circ + \mathbf{v}_b \cdot \nabla \circ. \quad (2.21)$$

Using the diffusion equation (2.18), the boundary condition (2.19), the material velocity (2.20) and the material derivative (2.21), the species conservation problem obtains the following form

$$\boxed{\begin{aligned} D_t Y_C + D \nabla Y_C \cdot \nabla Y_C - D \Delta Y_C &= 0, & \text{in } \Omega(t), \\ \rho D \nabla Y_C \cdot \mathbf{n} - \mathbf{j}_W^{in} \cdot \mathbf{n} &= 0, & \text{on } \Gamma(t). \end{aligned}} \quad (2.22)$$

### Growth

The rate of change in volume of a time dependent domain  $\Omega(t)$  is determined through the Reynolds-Transport formula (compare e.g. Quarteroni et al. 2000): for any differentiable function  $\xi$  defined on a time dependent domain  $\Omega(t)$  we find

$$d_t \int_{\Omega(t)} \xi dx = \int_{\Omega(t)} \partial_t \xi dx + \int_{\Gamma(t)} \mathbf{v}_b \cdot \mathbf{n} d\gamma, \quad (2.23)$$

where  $\mathbf{v}_b$  is the velocity of the boundary. Using Eq. (2.23) with  $\xi \equiv 1$  we find

$$d_t V_{ol} = d_t \int_{\Omega(t)} dx = \int_{\Gamma(t)} \mathbf{v}_b \cdot \mathbf{n} d\gamma = \int_{\Omega(t)} \operatorname{div} \mathbf{v}_b dx = \int_{\Omega(t)} RGR dx, \quad (2.24)$$

where the general definition of  $RGR$  (2.3) and Gauss' Theorem were used. The boundary velocity has to be continued into  $\Omega(t)$  by a meaningfully defined vector field, i.e. one that is able to represent local growth and one that continuously assumes the boundary velocity. Above such a continuation was found [Eq. (2.20)], so that a local expression for growth is

$$RGR = -D \Delta Y_C, \quad \text{in } \Omega(t). \quad (2.25)$$

As we will show later in Section 2.2.3, Eq. (2.5) follows from Eq. (2.25) by averaging over the cell volume.

### Cell membrane

Problem (2.22) allows the determination of the compound distribution in  $\Omega(t)$  and Eq. (2.25) gives a measure of the local growth. However, the water flux  $\mathbf{j}_W^{in}$  is still undetermined and depends on the sum of all concentrations of osmotically active substances inside and outside the cell, respectively. Inside the cell we assumed that the pressure gradient is small. Nonetheless, in the cell wall/membrane the pressure gradient is relevant for water transport. Instead of using Fick's law (2.16), the water flux  $\mathcal{F}_W$  in  $\Omega_w(t)$  can be approximated by an extended law (Chavarría-Krauser and Jäger 2005)

$$\mathcal{F}_W = -\rho \mathbf{D} \nabla Y_W - \rho \mathbf{K} \nabla p, \quad (2.26)$$

where  $\mathbf{D}$  and  $\mathbf{K}$  are the diffusion and barodiffusion tensors in the membrane. The plasma membrane has a complex structure, composed of a phospholipid bilayer resulting in an hydrophobic region surrounded by two hydrophilic regions (Taiz and Zeiger 1991). This prevents water diffusing easily directly through the membrane layers. Although the transport coefficient of water through the membrane is

small, it can be large enough to guarantee supply. The details behind membrane water transport are still not known. Specialized protein pores named *aquaporins* have been determined recently, but their exact function is still unknown (Maurel 1997; Nobel 1999; Tyerman et al. 1999). Therefore, tensorial diffusion and baro-diffusion coefficients may be needed. Here, we assume that water transport occurs only normal to the boundary  $\Gamma_w(t)$ , i.e.  $\mathbf{D} = \mathcal{D} \mathbf{n}_w \otimes \mathbf{n}_w$  and  $\mathbf{K} = \mathcal{K} \mathbf{n}_w \otimes \mathbf{n}_w$ , where  $\mathcal{D}, \mathcal{K} \in \mathbb{R}$  and  $\mathbf{n}_w$  is the normal vector of  $\Gamma_w(t)$ . The species conservation demands that the fluxes through the inner part of  $\Gamma_w(t)$  and  $\Gamma(t)$  must be equal

$$\mathbf{j}_W^{in} = \mathcal{F}_W = -\rho \mathcal{D} \nabla Y_W - \rho \mathcal{K} \nabla p, \quad \text{on } \Gamma_w(t). \quad (2.27)$$

Due to the complex structure of the membrane, the determination of the pressure and water concentration gradients is not trivial. However, these can be approximated by the difference in values between the inner and the outer sides of the membrane (Nobel 1999)

$$\begin{aligned} \nabla Y_W &\approx \frac{Y_W - Y_W^{out}}{h} \mathbf{n}_w = \frac{Y_C^{out} - Y_C}{h} \mathbf{n}_w, & \text{on } \Gamma_w(t), \\ \nabla p &\approx \frac{p - p^{out}}{h} \mathbf{n}_w, \end{aligned}$$

where  $h$  is the thickness of the membrane. Altogether renders the water flux approximation

$$\mathbf{j}_W^{in} \approx -\rho L_p \left( p - p^{out} - \frac{\mathcal{D}}{\mathcal{K}} (Y_C - Y_C^{out}) \right) \mathbf{n}_w, \quad \text{on } \Gamma_w(t) \quad (2.28)$$

where  $L_p = \mathcal{K}/h$  is the water conductivity coefficient. It should be kept in mind that the normal vectors of  $\Gamma(t)$  and  $\Gamma_w(t)$  show in opposite directions, i.e.  $\mathbf{n}_w = -\mathbf{n}$ . We should also mention here that  $\Gamma_w(t)$  was represented in a strongly simplified manner. The osmotic active compounds are stored in the vacuole of the cell, which is surrounded by a membrane separating it from the cytoplasm. The cytoplasm itself is contained in a protecting membrane, the plasma membrane, and the cell wall which spends rigidity to the whole complex (see Fig. 2.1).  $\Gamma_w(t)$  contains all these layers, so that  $\mathcal{D}$  and  $\mathcal{K}$  have to be understood as the average transport coefficients over the entire composite.

### Example

In this section we would like to present an example of a spherical cell suspended in water. We assume that the pressure in the water is small compared to the turgor in the cell ( $p^{out} \approx 0$ ) and that no compound is dissolved in the water ( $Y_c^{out} = 0$ ). The deformation of a pressurized hollow spherical body with a thin wall and vanishing outside pressure is given by (Landau and Lifschitz 1991a)

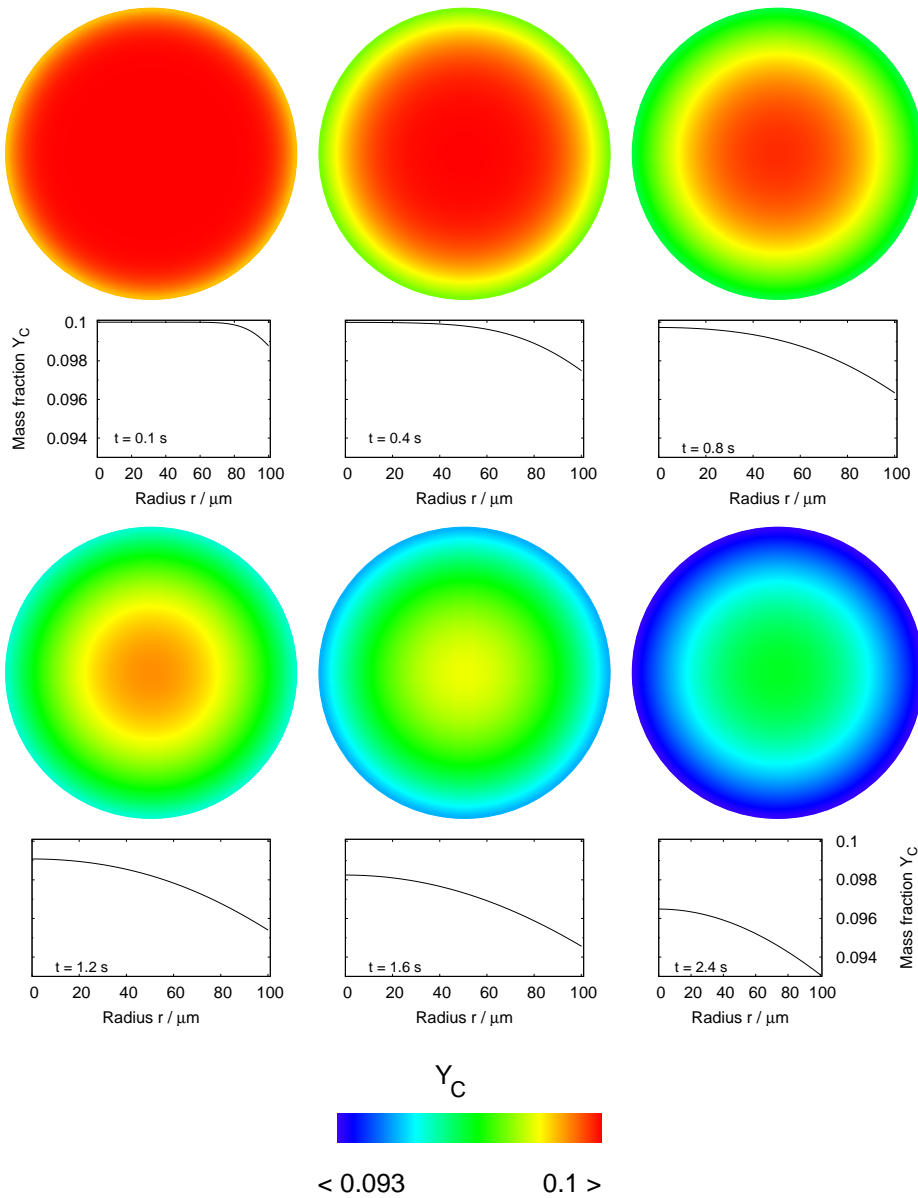


**Figure 2.3:** Modeled mass fraction  $Y_C$  during turgor recovery of a spherical cell with *loose cell wall* ( $\lambda = 10^{-4} \text{ m MPa}^{-1}$ ). Data visualized by cutting the sphere at the equator and subsequently colorcoding the values. Below the colorcoded images, the radial dependence is shown.

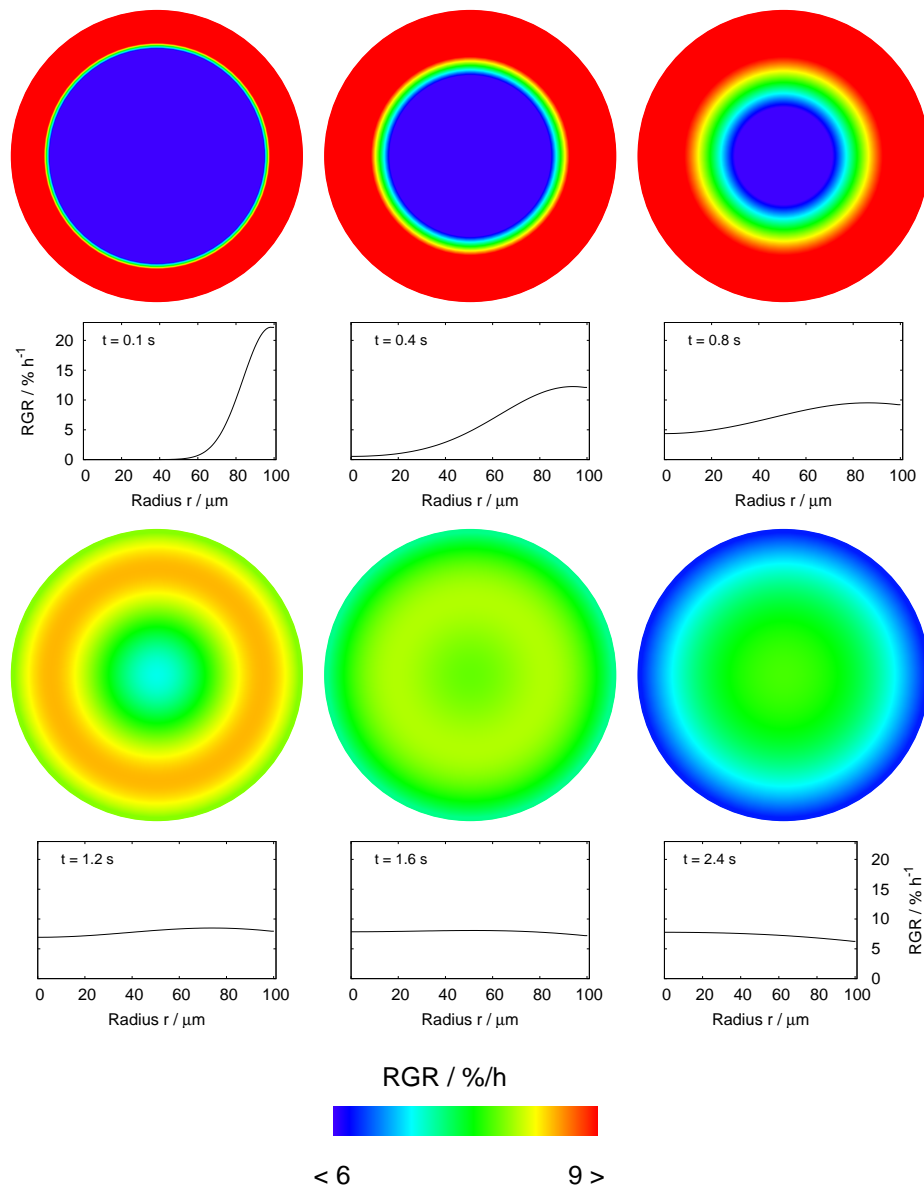


**Figure 2.4:** Simulated  $RGR$  during turgor recovery of a spherical cell with *loose cell wall* ( $\lambda = 10^{-4} \text{ m MPa}^{-1}$ ). Data visualized as in Fig. 2.3.

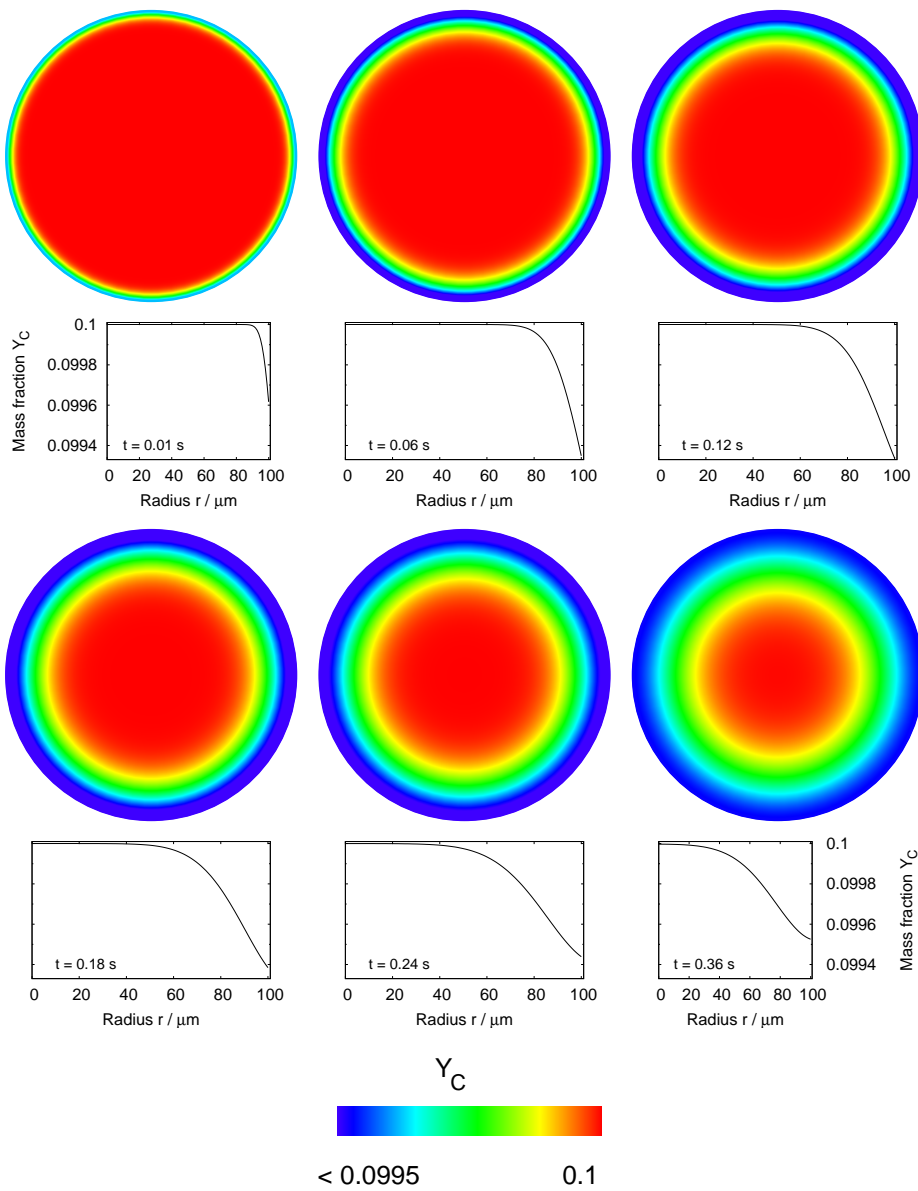


**Figure 2.5:** Simulated mass fraction  $Y_C$  during turgor recovery of a spherical cell with *stiff cell wall* ( $\lambda = 10^{-7} \text{ m MPa}^{-1}$ ). Data visualized as in Fig. 2.3.

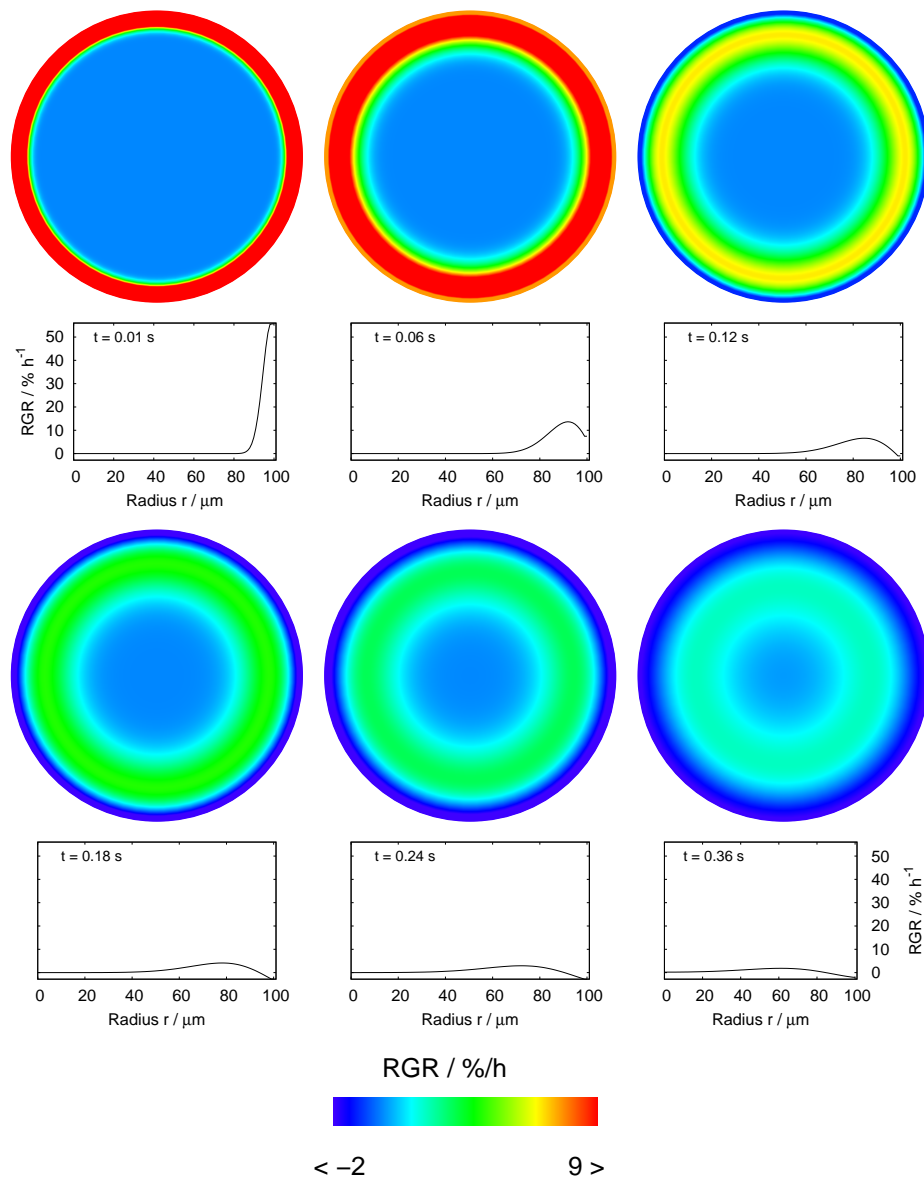


**Figure 2.6:** Simulates  $RGR$  during turgor recovery of a spherical cell with *stiff* cell wall ( $\lambda = 10^{-7} \text{ m MPa}^{-1}$ ). Data visualized as in Fig. 2.3.

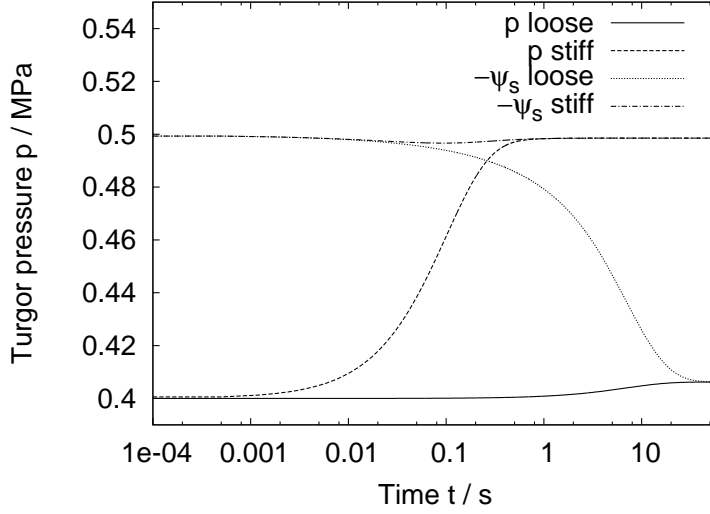


**Figure 2.7:** Recovery of cell turgor  $p$  in spherical cells of loose and stiff cell wall ( $\lambda = 10^{-4} \text{ m MPa}^{-1}$  and  $\lambda = 10^{-7} \text{ m MPa}^{-1}$ ). Initially, the cell had a turgor of  $p_0 = 0.4 \text{ MPa}$  and an osmotic potential of  $\psi_s^0 = -0.5 \text{ MPa}$ .

$$u = p \frac{R^2 (1 - \sigma)}{2 E h} = p \lambda, \quad (2.29)$$

where  $u$  is the radial deformation,  $R$  is the initial radius,  $\sigma$  is Poisson's ratio,  $E$  is Young's modulus of the material and  $\lambda := \frac{R^2 (1 - \sigma)}{2 E h} = \text{const}$ . Using (2.19), (2.20), (2.28) and the time derivative of (2.29) we find an ODE describing the pressure

$$\begin{aligned} d_t p &= -\frac{L_p}{\lambda} (p + \psi_s), & \text{for } t > t_0, \\ p &= p_0, & \text{for } t = t_0, \end{aligned} \quad (2.30)$$

where  $\psi_s = -\frac{\mathcal{Q}}{\mathcal{K}} Y_C$  is the osmotic potential. This equation allows together with Problem (2.22) the determination of the concentration distribution  $Y_C$  and the pressure. We introduce therefore spherical coordinates and assume that  $Y_C$  is only a function of the radius  $Y_C = Y_C(r)$ . We obtain the problem

$$\begin{aligned} D_t Y_C + D (\partial_r Y_C)^2 - D \frac{1}{r^2} \partial_r (r^2 \partial_r Y_C) &= 0, & \text{for } 0 < r < R + u(t), \\ \partial_r Y_C &= 0, & \text{for } r = 0, \\ \partial_r Y_C - \frac{L_p}{D} (p + \psi_s) &= 0, & \text{for } r = R + u(t). \end{aligned} \quad (2.31)$$

Problems (2.30) and (2.31) do not suffice to describe the here proposed problem, as the domain and hence  $r = r(t)$  depend on time. A geometric assumption is needed to solve this *free boundary problem*. In the here presented case, we included this assumption by using a spherical cell at all times. However, (2.31)

**Table 2.1:** Simulation parameters for cell turgor recovery. Poisson's ratio  $\sigma$  and Young's Modulus  $E$  vary considerably, the values obtained for onion cells (Wei et al. 2001) and wood (Vogel 1995) were taken to estimate the dimension of  $\lambda$ .

Cell wall	$R$ ( $\mu m$ )	$\sigma$	$E$ ( $MPa$ )	$h$ ( $\mu m$ )	$\lambda$ ( $m MPa^{-1}$ )	$L_p$ ( $m s^{-1} MPa^{-1}$ )
loose	100	0.2 to 0.3	3.5 to 8	ca. 1	$10^{-4}$	$10^{-6}$
stiff	100	ca. 0.3	ca. $15 \times 10^3$	ca. 1	$10^{-7}$	$10^{-6}$
Initial conditions	$\psi_s^0$ ( $MPa$ )	$p_0$ ( $MPa$ )	$\Omega_0$			
	-0.5	0.4	$B_R(0)$			

is still posed on a time dependent domain. A numerical solution can be obtained by using Lagrangian coordinates (i.e.  $D_t \rightarrow \partial_t$ ) and solving the resulting diffusion equation. This implies, however, that special care has to be taken during the numerical treatment of the problem. Using a finite difference approach on a non-uniform discretization is reasonable due to the simple implementation and the simplicity of the problem. To obtain the discretization at a certain point in time, the initial uniform discretization is deformed in time by assuming that the deformation is produced by a flow of velocity  $\mathbf{v}_b$

$$\begin{aligned} d_t \mathbf{x} &= -L_p (p + \psi_s) , & \mathbf{x} \in \Omega(t) & \text{ and } t > t_0 , \\ \mathbf{x} &= \mathbf{x}_0 , & \mathbf{x}_0 \in \Omega_0 & \text{ and } t = t_0 . \end{aligned} \quad (2.32)$$

After exchanging the spatial derivatives by suitable discrete difference operators for non-uniform discretizations (Großmann and Roos, 1994), Eqs. (2.30), (2.31) and (2.32) can be solved using an explicit Euler-Scheme.

Two examples were simulated, one of a loose and the other of a stiff cell wall (Figs. 2.3 to 2.7). The corresponding parameters are shown in Table 2.1. Measurement of Young's modulus  $E$  and Poisson's ratio  $\sigma$  for cell walls is not trivial, we therefore approximated roughly the coefficient  $\lambda$ . For the loose wall the values found for onion cells were used (Wei et al., 2001), while the values of wood were used for the stiff cell (Vogel 1995).

Both cells recover their turgor up to a certain value, which depends strongly on the stiffness factor  $\lambda$  (Fig. 2.7). The cells differ in the rate of turgor recovery and in the value reached after recovery. As expected, the stiff cell reaches much sooner full turgescence than the loose cell. It grows thereby much less, clearly shown in the higher turgescence and low dilution of  $\psi_s$  (Fig. 2.7). As a consequence of growth and hence dilution, the loose cell reaches a substantially lower turgor (Fig. 2.7). It becomes here clear, that a cell with loose wall is in need of an osmoregulation.<sup>3</sup>

<sup>3</sup>Osmoregulation: regulation of the cell's, in particular the vacuole's, osmotic potential. There

The compound distribution and the growth distribution inside the cell brings more insight into the differences between the stiff and loose cells (Figs. 2.3 to 2.6). The compound in the loose cell is slowly diluted from the boundary towards the center, until almost a constant curvature of the radial distribution is found (Fig. 2.3). This is clearly reflected in the  $RGR$  distribution (Fig. 2.4), which moves almost as a wave from the boundary into the center and becomes slowly almost constant along the radius (ca.  $7\% h^{-1}$  at  $t = 1.6 s$ ). Nonetheless, the region near the boundary starts slowly to grow less than the center ( $t = 2 s$ , Fig. 2.4), and the cell diminishes overall growth. The stiff cell shows a different recovery pattern (Fig. 2.5 and 2.6). As in the case of the loose cell, the compound is diluted from the boundary towards center. However, the radial compound distribution does not reach an almost constant curvature. An increase in concentration in the region near the boundary, due to the fast pressure increase, is found instead (Fig. 2.5). The  $RGR$  distribution shows this behavior more clearly. The growth moves from the boundary towards the center, as for the loose cell. Due to the increasing pressure (Fig 2.7), less water can enter the cell and growth near the boundary loses strength. There is even a certain critical time, when negative growth near the boundary is found ( $t > 0.12 s$ , Fig. 2.6). This is explained by the strongly reduced water influx, resulting in the boundary tending to lose water in favor of more central regions. The negative and positive growth approach zero, when the cell stops to grow.

### 2.2.2 Energy conservation

Energy conservation states that the rate of change of internal energy of a body  $\Omega_w$  is given by the sum of the work done by or on the body per unit time and of the rate of heat exchange (Landau and Lifschitz 1987). This can be generalized for continua by using the energy density

$$d_t \mathcal{E} = d_t \mathcal{R} + d_t \mathcal{Q} , \quad (2.33)$$

where  $\mathcal{R}$  is the work density and  $\mathcal{Q}$  is the heat density. The energy  $E$  of the complete body is obtained through integration of the density over the domain  $\Omega_w$

$$E = \int_{\Omega_w} \mathcal{E} dx .$$

Eq. (2.33) can be used to determine the rate of cell wall expansion (Veytsman and Cosgrove 1998). This is achieved by assuming that cell wall expansion is due to creeping of the wall. Creeping occurs when the stability condition for the volume dependence of the pressure is not fulfilled, i.e. when  $\frac{\partial p}{\partial V} \geq 0$  (Landau

---

are several choices of how this can be achieved, e.g. ion fluxes, osmotic activation of a compound by chemical reaction, etc. (see Kauss 1978 for algae).

and Lifschitz 1987; Veytsman and Cosgrove 1998). If the inner energy of the cell wall is assumed to be constant during creep, the rate of expansion is determined solely by the work rate  $d_t \mathcal{R}$  and the viscous dissipation of energy  $d_t \mathcal{Q}$ . Expansion changes the inner structure of the cell wall, e.g. the angle of the microfibrills changes in relation to the cell axis (see Section 2.1). A change of inner structure is accompanied by a change of inner energy, which is counteracted by deposition of new cell wall material. The above assumption of a constant inner energy, is therefore only a rough approximation to cell wall expansion.

### Deformation work

The work per unit time achieved by a deformation of a body  $\Omega_w$  is given by (Landau and Lifschitz 1991a)

$$\int_{\Omega_w} d_t \mathcal{R} dx = \int_{\Omega_w} \operatorname{div} \boldsymbol{\sigma} \cdot d_t \mathbf{u} dx ,$$

where  $\boldsymbol{\sigma}$  is the stress tensor<sup>4</sup> and  $\mathbf{u}$  is the displacement. As  $\operatorname{div} \boldsymbol{\sigma}$  is the force acting on a differential volume and  $d_t \mathbf{u}$  is the displacement per unit time, this equation is the continua version of the simple law *work = force  $\times$  displacement*. The integrand on the left side can be transformed into a total divergence and a correction term

$$\operatorname{div} \boldsymbol{\sigma} \cdot d_t \mathbf{u} = \operatorname{div} (\boldsymbol{\sigma} \mathbf{u}) - \boldsymbol{\sigma} : \nabla d_t \mathbf{u} ,$$

where  $\mathbf{A} : \mathbf{B} = \sum_{i,j} A_{ij} B_{ij}$  and  $(\nabla \mathbf{a})_{ij} = \partial_i a_j$ . Because the stress tensor  $\boldsymbol{\sigma}$  is symmetric,  $\nabla d_t \mathbf{u}$  can be symmetrized to obtain the time derivative of the strain tensor  $d_t \nabla \mathbf{u} = d_t \boldsymbol{\varepsilon}$ .<sup>5</sup> We find altogether for the work per unit time

$$\int_{\Omega_w} d_t \mathcal{R} dx = \int_{\Gamma_w \cup \Gamma_w^{out}} \mathbf{P} \cdot d_t \mathbf{u} d\gamma - \int_{\Omega_w} \boldsymbol{\sigma} : d_t \boldsymbol{\varepsilon} dx . \quad (2.34)$$

where  $\mathbf{P} = \boldsymbol{\sigma} \mathbf{n}$  is the force per unit area acting on  $\Gamma_w$ . The first term on the right of Eq. (2.34) represents the work achieved by the external forces, while the second term represents the work done by the stresses inside  $\Omega_w$ .

### Energy dissipation

Cell wall expansion is connected to energy dissipation due to the viscosity of the cell wall and to the finiteness of the expansion velocity. For small expansion

<sup>4</sup>Because the stress tensor is designed here by  $\boldsymbol{\sigma}$  and Poisson's ratio by  $\sigma$ , no danger of mistaking them arises. Moreover,  $\sigma$  does not appear in this Section.

<sup>5</sup>The displacement and the strain tensor are defined in relation to the original  $\Omega_w$ , so that the time and spatial derivatives commute.

velocities, the energy dissipation due to internal friction can be approximated by a *dissipation function* (Landau and Lifschitz 1991a), which is a quadratic function of the rate of deformation  $d_t \boldsymbol{\varepsilon}$ . The dissipated energy is

$$\int_{\Omega_w} \mathcal{R}_{dis} dx = \int_{\Omega_w} d_t \boldsymbol{\varepsilon} : \boldsymbol{\eta} : d_t \boldsymbol{\varepsilon} dx , \quad (2.35)$$

where the fourth order tensor  $\boldsymbol{\eta}$  is the viscosity tensor, which fulfills the symmetry conditions

$$(\boldsymbol{\eta})_{iklm} = (\boldsymbol{\eta})_{lmik} = (\boldsymbol{\eta})_{kilm} = (\boldsymbol{\eta})_{ikml} .$$

If no other processes are involved in heat production, the rate of change of heat and the rate of dissipation are equal  $d_t \mathcal{Q} = -d_t \mathcal{R}_{dis}$ .

### Non-Equilibrium

In non-equilibrium under the assumption that  $d_t \mathcal{E} = 0$ , the dissipated energy equals the work:  $d_t \mathcal{R} = d_t \mathcal{R}_{dis}$ . Using Eqs. (2.34) and (2.35) we obtain

$$\int_{\Omega_w} (\boldsymbol{\eta} : d_t \boldsymbol{\varepsilon} + \boldsymbol{\sigma}) : d_t \boldsymbol{\varepsilon} dx = \int_{\Gamma_w \cup \Gamma_w^{out}} \mathbf{P} \cdot d_t \mathbf{u} d\gamma .$$

The term on the right hand side represents the work achieved by the surrounding medium. For a pressurized cavity and a vanishing outside pressure, the surface forces are  $\mathbf{P} = -p \mathbf{n}_w$ , where  $p \neq 0$  for the inside and  $p = 0$  for the outside and  $\mathbf{n}_w$  is the normal of  $\Gamma_w$ . This term obtains then the usual form found in thermodynamics for an expanding gas:  $-p d_t V_{ol}$  (Landau and Lifschitz 1987). The integral over the inner boundary can be converted into an integral over the inner medium

$$\int_{\Gamma_w} \mathbf{P} \cdot d_t \mathbf{u} d\gamma = - \int_{\Gamma_w} p \mathbf{n}_w \cdot d_t \mathbf{u} d\gamma = \int_{\Gamma} p \mathbf{n} \cdot \mathbf{v}_b d\gamma = \int_{\Omega} \text{div} (p \mathbf{v}_b) dx ,$$

where  $\mathbf{n}_w = -\mathbf{n}$  and  $d_t \mathbf{u} \cdot \mathbf{n} = \mathbf{v}_b \cdot \mathbf{n}$  on  $\Gamma$  [compare (2.20)] were used. If the pressure is assumed to be constant, the energy balance obtains the following form

$$\boxed{\int_{\Omega_w} (\boldsymbol{\eta} : d_t \boldsymbol{\varepsilon} + \boldsymbol{\sigma}) : d_t \boldsymbol{\varepsilon} dx = p \int_{\Omega} RGR dx + \int_{\Gamma_w^{out}} \mathbf{P} \cdot d_t \mathbf{u} d\gamma ,} \quad (2.36)$$

where  $RGR = \text{div} \mathbf{v}_b$  was used [Eq. (2.3)]. Eq. (2.36) has to be understood as a method to determine the pressure in  $\Omega$ . However, it becomes again clear that a constant pressure is only a rough approximation. In reality, local variations in pressure are expected due to the not necessarily constant  $\boldsymbol{\eta}$  and  $\boldsymbol{\sigma}$ . The second term on the right of (2.36) models external forces. These forces may arise from friction with the outer medium or from growing neighbor cells. It represents thus a connection to biomechanical modeling of the tissue. However, these forces have to be determined, which is not straightforward for growing tissues.

### 2.2.3 Simplifications

The aim of this section is to show that the Lockhart Eq. (2.4) and the osmometer Eq. (2.5) follow from Eqs. (2.25) and (2.36) by using simple geometric simplifications.

#### Water uptake

The average relative growth rate  $\overline{RGR}$  of a cell can be obtained using Eq. (2.25) and applying Gauss' Theorem

$$\overline{RGR} = \frac{1}{V_{ol}} \int_{\Omega} RGR \, dx = -\frac{1}{V_{ol}} \int_{\Gamma} D \nabla Y_C \cdot \mathbf{n} \, d\gamma$$

Using the boundary conditions of Problem (2.22) and the approximation of the water influx (2.28), we find

$$\overline{RGR} = -\frac{A_s}{V_{ol}} L_p (p - p^{out} + \psi_s - \psi_s^{out}) , \quad (2.37)$$

where  $A_s$  is the measure of  $\Gamma$ , i.e. the surface area of  $\Omega$ , and  $\psi_s = -\frac{\mathcal{Q}}{\mathcal{K}} Y_C$  was used. In the intercellular spaces,  $\psi_s^{out}$  and  $p^{out}$  can be assumed to be small. Using  $d_t V_{ol} = V_{ol} \overline{RGR}$  shows finally that Eq. (2.37) is equivalent to the osmometer Eq. (2.5).

#### Elongation rate

If we assume a cylindrical geometry and a deformation along the cylinder ( $x_3$ -axis), the strain velocity tensor reduces into a scalar  $(d_t \boldsymbol{\varepsilon})_{33} = d_t \ln l$ , where  $l$  is the length of the cylinder. Only one component of the viscosity and stress tensors appear in the equation:  $(\boldsymbol{\eta})_{3333}$  and  $(\boldsymbol{\sigma})_{33}$ . Assuming that no forces act on the external boundary  $\Gamma_w^{out}$ , Eq. (2.36) reduces into

$$RGR = \phi (p - Y) , \quad (2.38)$$

where  $\phi = \frac{1}{(\boldsymbol{\eta})_{3333}} \frac{V_{ol}}{\mu(\Omega_w)}$ ,  $Y = \frac{\mu(\Omega_w)}{V_{ol}} (\boldsymbol{\sigma})_{33}$  and  $\mu(\Omega_w)$  is the measure of  $\Omega_w$ . Eq. (2.38) is nothing else than the Lockhart-Equation (2.4) (Lockhart 1965). For a cylindrical body with circular base of diameter  $D$  and wall thickness  $h$ , we find  $\mu(\Omega_w) \approx \pi D h l$  and  $V_{ol} = \frac{\pi}{4} D^2 l$ , so that  $V_{ol}/\mu(\Omega_w) \approx \frac{D}{4h}$ . Eq. (2.38) obtains then the form found by Veytsman and Cosgrove 1998.

# Chapter 3

## Root Growth Model

### 3.1 Introduction

Plants acquire essential nutrients and water through their roots. It is thus not astonishing that root growth serves as an instrument to overcome depletion of nutrients and/or water (Scheible et al. 1997). Root growth is therefore of particular interest for plant physiologists. Mechanisms essential for plants, such as *extension growth*, and tropisms such as *gravitropism*, *hydrotropism* and *phototropism*<sup>1</sup>, rely on both hormonal signaling and cell expansion (Cosgrove 1992; Perbal and Driss-Ecole 2003; Eapen et al. 2005). It is also well known that phytohormones control growth of plant organs by balancing cell proliferation and differentiation (Beemster et al. 2003; del Pozo et al. 2005). Thus, finding a connection between hormonal models (*fountain-model*; Chapter 5; Evans et al. 1986; Muday 2001; Perbal and Driss-Ecole 2003) and biophysical growth models (*Lockhart-Equation*; Chapter 2; Lockhart 1965; Cosgrove 1986; Passioura and Fry 1992) is a critical first step for an accurate model of root growth.

Two different characterizations of root growth are found: system expansion through branching and individual root elongation. Leading to two different classes of models, those describing the topology of root system (e.g. Pages et al. 1989; Fitter et al. 1991; Buckner et al. 1996; Berntson 1997), and those which focus on the distribution of growth properties of single roots, including velocity, rate and cell length (Goodwin and Stepka 1945; Erickson and Sax 1956; Beemster and Baskin 1998; Silk 1992; Pritchard et al. 1993; Evans et al. 2001; Walter et al. 2002).

The distribution of growth in primary roots has been traditionally measured

---

<sup>1</sup>*gravitropism*: tendency of a plant organ to grow either towards (positive) or away from (negative) the gravity vector. Roots are positively gravitropic while hypocotyls are negatively gravitropic. *hydrotropism*: tendency for a roots to follow gradients of humidity in the soil. *phototropism*: tendency to grow towards or away from light sources.

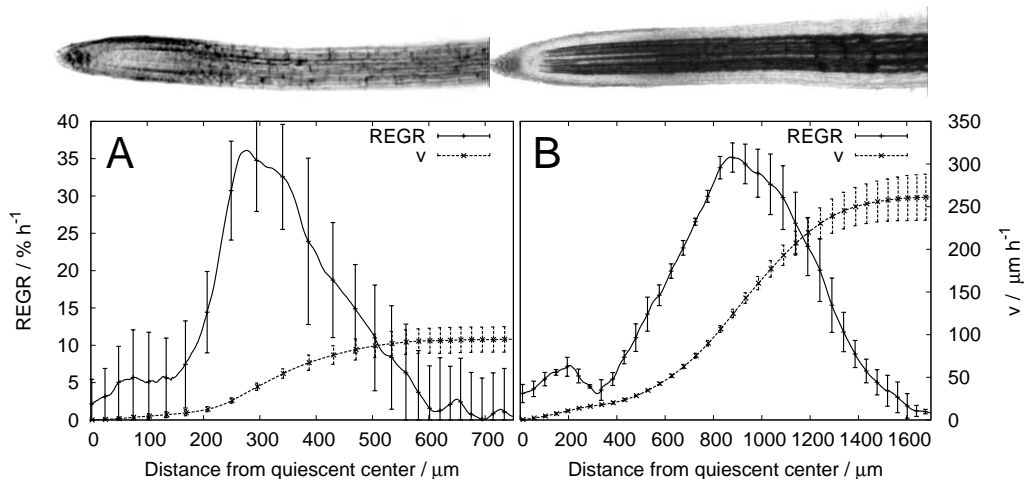


**Figure 3.1:** Relative elemental growth rate,  $REGR$ , and velocity distributions along typical root tips of A, *Arabidopsis thaliana* (L.) Heynh. and B, *Nicotiana tabacum* (L.) (Data courtesy of Kerstin Nagel, Forschungszentrum Jülich). The quiescent center, a region of mitotically inactive cells located apically of the meristem, was chosen as the frame of reference.

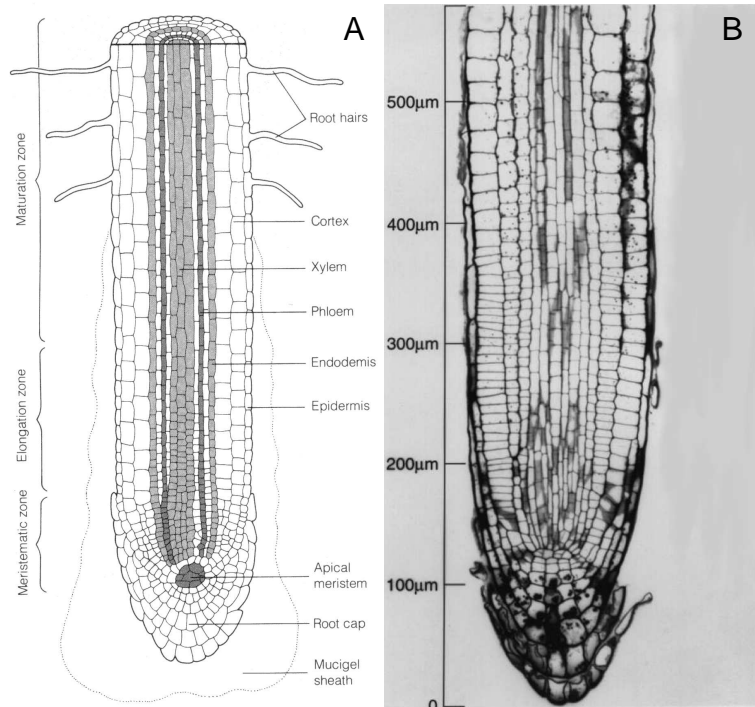


**Figure 3.2:** A, Schematic representation of a primary root tip with its different tissues and zones (Modified from Russell, 1977). B, Microscopic picture of an *Arabidopsis thaliana* (L.) Heynh. root (Modified from Ishikawa and Evans 1997).

using charcoal marks on the root surface (Erickson and Sax, 1956). The position of the marks are determined in time and the *REGR* is calculated through one of the Eqs. (2.1) or (2.2). This method allows only a poor spatial and temporal resolution. To obtain a *REGR* distribution, interpolating schemes on the positions have to be used leaving a wide range of error in the resulting distribution (Peters and Bernstein 1997). New techniques with high temporal and spatial resolution have recently become available to quantify growth fields (Schmundt et al. 1998; Walter et al. 2002; van der Weele et al. 2003). These techniques are based on image sequences produced by CCD or CMOS cameras. Through the determination of the movement of gray-value structures, the velocity vector field  $\mathbf{v}(\mathbf{x}, t)$  and the *REGR* are approximated.

Root tips, independent of the species, show a typical bell shaped *REGR* profile (Fig. 3.1 for *A. thaliana* and *Nicotiana tabacum* (L.) root tips). The increase in *REGR* along the root tip has traditionally been thought to be continuous (Morris and Silk 1992; Sacks et al. 1997). However, the new techniques of high spatial resolution show a more or less constant *REGR* in the meristem and a sudden transition into the elongation zone (Fig. 3.1; van der Weele et al. 2003), which is supported by cell length measurements (Ivanov and Maximov 1999). This suggests the existence of a critical condition to attain the transition into elongation and a correlation between cell size and division rate in the meristem (Ivanov and Maximov 1999). As we will show later, this allows to obtain a connection between the division rate and the average *REGR* in the meristem (Section 3.2.5).

Until now the approach to model *REGR* distributions along root tips (Fig. 3.1) has been based on conservation and kinetic equations, such as those used by Silk (1992). Empirical approaches, e.g. the use of a logistic fit, have also been used (Morris and Silk 1992). However, these approaches do not focus on modeling the control of the elongation zone, but rather on characterizing cell production and expansion rates under different environmental conditions: temperature, water stress, nutrient availability, etc. Moreover, mechanistic understanding of root growth needs to take into account the architecture of the root growth zone. The root tip is comprised of the apical and basal meristem, the elongation-only zone and the mature root (Fig. 3.2; Beemster et al. 2003). Most cell divisions occur in the apical meristem, although some are also found in the basal meristem. The elongation-only zone is characterized by cell elongating, most probably through water uptake of the vacuole (Brumfield 1942), and almost no dividing cell. In the mature part of the root cells do not divide or grow to produce elongation.<sup>2</sup>

This work presents a novel approach to model these distributions. The meristem and elongation-only zone of a root (Fig. 3.2) is described by a one dimensional string of cells. A cell is the smallest entity taken into account, i.e. the

---

<sup>2</sup>Cell division occurs in the mature root part mainly for secondary growth and root branching.

internal cell structure (cytoplasm, vacuole, plastides, etc.; compare Fig. 2.1 on page 4) will not be taken into account. Cell properties, such as *REGR* and phytohormonal concentrations will be assumed to be homogeneous inside a cell. The position of the cells is described by one spatial variable  $x \in \mathbb{R}_0^+$ , which measures the arc length between the cells and the quiescent center.<sup>3</sup> The number  $N(t) \in \mathbb{N}$  of cells in the string changes in time  $t$  due to cell division. Cell death in this region is negligible resulting in a mortality rate of zero, while the division rate, i.e. the number of divisions a cell goes through within one hour, is positive or zero. The division process is assumed to be symmetric, i.e. the two cells produced by division are indistinguishable. This means that both daughter cells have the same length and undergo the same processes. Furthermore, we assume that the length of the tissue is not affected by cell division. Not only division affects cell length, but also growth, so that each cell has a time-dependent length denoted here by  $l_k(t)$ , where  $k = 1, \dots, N(t)$ .

In analogy to the known architecture of the root growth zone (Beemster et al. 2003), we assume that cell division occurs at the end of the string of cells representing the root tip (division zone), followed by a segment of cells undergoing elongation (elongation-only zone), resulting in a saturation zone and finally a zone of mature cells. We assume that the transition between these phases is determined by a ratio function  $\omega = \omega(c_1(x), c_2(x)) \in \mathcal{C}^0(\mathbb{R} \times \mathbb{R}, \mathbb{R})$ , which depends on the concentrations  $c_1(x)$  and  $c_2(x)$  of two hypothetical hormones. These hormones were chosen to have auxin- and cytokinin-like properties. These hypothetical hormones are assumed to be produced as cytokinin and auxin in the root tip and in the plant shoot, respectively (Taiz and Zeiger 1991). Moreover, these are assumed to be subjected to degradation, dilution and cell-to-cell transport, either of diffusive or active nature. Throughout this Chapter, Latin indices will assume values from 1 to  $N(t)$ , while Greek indices assume the values 1 and 2. Time  $t$  will be given in hours and minutes (*h* and *min*), position in *mm*, cell lengths in  $\mu\text{m}$  and concentrations in  $\text{mmol m}^{-3}$ . The terms *auxin* and *cytokinin* will be used freely to design the two hypothetical hormones. However, the reader should keep in mind that the effect of auxin and cytokinin is too complex to be described completely, so that the hypothetical hormones were chosen to resemble only some of the properties of these two phytohormones.

## 3.2 Biophysical equations

We saw in Chapter 2 that cell growth can be described by two equations, corresponding to mass and energy conservation. We saw also that the turgor functions as a separation variable between these two equations [Eqs. (2.4) and (2.5)], so that

---

<sup>3</sup>Quiescent center: region of mitotically inactive cells at the root tip (Fig. 3.2).

it assumes a certain value depending on the wall extensibility and on the concentration of solutes inside the cell [Eq. (2.8)]. This allows to obtain an elongation rate that is independent of the turgor [Eq. (2.9)].

The connection between growth rate, wall extensibility  $\phi$  and turgor  $p$  is essential to model correctly the *REGR* distribution. A cell length dependent *REGR* would change during cell division. For example, a linear dependence,  $REGR \propto l$ , would result in half *REGR* after a division. Such disturbances in the meristem's growth have not been reported (Ivanov and Maximov 1999), suggesting a cell length independent *REGR*. Measurements of the velocity distribution along the root show that the distribution in the elongation-only zone depends linearly on the coordinate (van der Weele et al. 2003), so that the slope, i.e. the *REGR*, does not depend on cell length. Additionally, the Lockhart-Equation has been validated by an approach describing cell wall creep (Veytsman and Cosgrove 1998). We therefore use here the simplified versions as the underlying cell growth equations [Eq. (2.37) and (2.38); page 22].

### 3.2.1 Approximations

Lockhart 1965 suggests that water conductivity  $L_p$  is not restricting for growth of single cells. Although root cells compose a tissue and cannot be treated as single cells, this view is supported by measurements of turgor  $p$  along the root axis. If water conductivity would be restricting, Eq. (2.8) implies that  $p$  would approach the yield threshold  $Y$  (i.e.  $\lim_{L_p \rightarrow 0} p = Y$ ). However,  $p$  in root tips has been found to be substantially higher than  $Y$ , showing that  $L_p$  is not a restricting factor in root tips (Pritchard et al. 1990; Spollen and Sharp 1991; Pritchard et al. 1993). In other tissues, e.g. leaves, water supply may be restricting (see e.g. Boyer 1968).

For non-restricting water conductivity, normal root cell geometry and normal cell wall extensibility  $\phi$ , we find a small ratio of volume increase to water uptake  $\gamma := V_{ol} \phi / A_s L_p$ .<sup>4</sup> Under this condition Eq. (2.9) simplifies, up to second order in  $\gamma$ , to

$$d_t l = -l \phi (\psi_s + Y) + \gamma l \phi (\psi_s + Y) + O(\gamma^2), \quad (3.1)$$

where  $\psi_s$  is the osmotic potential. Eq. (2.8) becomes

$$p = -\psi_s + \gamma (\psi_s + Y) + O(\gamma^2). \quad (3.2)$$

---

<sup>4</sup>The assumption of a small  $\gamma$  is legitimate for all cells found in root tips: a young meristematic cell has  $\gamma \approx 10^{-5}$ , while a cell located at the growth maximum has  $\gamma \approx 10^{-4}$  and a mature cell has  $\gamma \approx 0$ .

The zero order approximation shows that the *REGR* is independent of the surface to volume relation and independent of the water conductivity. Additionally, the turgor tends to reach the osmotic potential inside the cell in well-watered conditions. The turgor has been found by other authors to be constant along and across the expanding region (e.g. Pritchard et al. 1990; Spollen and Sharp 1991). However, the first order approximation of the turgor, shows that this is rather unlikely as the wall extensibility and the relation between surface and volume change along the root axis. Additionally, the zero order approximation shows that a pattern in the osmotic potential is propagated into the turgor distribution. The osmotic potential is known to change along and across the root tip, else water uptake and transport into the xylem would not be possible (Murphy 2000; Pritchard et al. 2000). A careful inspection of the Figures published by Pritchard et al. (1993) demonstrates that the turgor falls along the root axis.

### 3.2.2 Osmotic potential $\psi_s$

The osmotic potential  $\psi_s$  is crucial for the water uptake of a cell and thus also for its growth (Eq. (3.1); Pritchard et al. 2000; Boyer and Silk 2003). However, absorbed water tends to increased  $\psi_s$ , so that cells have to regulate their osmotic potential to counteract dilution and to maintain growth. Root cells can increase their volume several times (from ca. 10  $\mu m$  to more than 100  $\mu m$  length within 10 h; Beemster and Baskin 1998). Without regulation  $\psi_s$  would soon reach  $-Y$ , i.e.  $p \rightarrow Y$ , and growth would cease. For example, the simulation presented in Chapter 2 showed that a cell with loose wall and no osmotic regulation tends rather to diminish the osmotic potential than increasing its turgor (Fig. 2.7).

The gas equation can be used to model changes of the osmotic potential  $\psi_s = RT n_s/V_{ol}$  (Landau and Lifschitz 1987; Génard et al. 2001)

$$d_t \psi_s = (RT/V_{ol}) d_t n_s - \psi_s d_t \ln V_{ol} + \psi_s d_t \ln T, \quad (3.3)$$

where  $R$  is the universal gas constant,  $T$  is the temperature,  $n_s$  is the number of moles of solutes. Assuming that the temperature is constant, the last term is zero. Génard et al. 2001 proposes a simplified Michaelis-Menten equation to model the accumulation process:  $d_t n_s \approx Z X V_{ol}$ , where  $Z$  is a maximum accumulation rate and  $X$  is the proportion of solutes that are not consumed and remain soluble. A cell will not accumulate more solutes than needed to be turgid and to maintain mechanical stability. We propose a simple osmotic regulation based on the maximum accumulation rate  $Z = \zeta_{max} (\psi_s - \overline{\psi_s})$ , where  $\zeta_{max} = \text{const}$  and  $\overline{\psi_s} = \text{const}$ . Therein, the osmotic potential fulfills the following ordinary differential equation

$$d_t \psi_s = \zeta (\psi_s - \overline{\psi_s}) - REGR \psi_s, \quad (3.4)$$

where  $\zeta := RT X \zeta_{max}$  and  $REGR = d_t \ln V_{ol}$ . Eq. (3.4) can be interpreted as a simple linear approximation of osmoregulation, where  $\zeta$  determines the relaxation time.

Water and solutes reach the root tip cells on two different pathways: symplastic and apoplastic<sup>5</sup> (Pritchard et al. 2000; Boyer and Silk 2003). Dilution is intrinsic to apoplastic water uptake. However, solutes that reach the growing cells through the symplastic pathway, i.e. supplied by the phloem, are not subjected as strongly to dilution. As a consequence, only a fraction of the dilution term in (3.4) acts on the osmotic potential. If the fraction of undiluted contribution in each cell is known, the dilution term could be easily corrected. The undiluted fraction may, however, depend on cell position (Pritchard et al., 2000). It becomes obvious that Eq. (3.4) is a very simplistic and rough approximation of osmoregulation. More complete water and solute uptake models exist (Murphy 2000; Murphy 2003; Boyer and Silk 2003), which would not bring here more insight into the root growth model. We therefore restrict the model to the simplest possible osmoregulation (3.4).

### 3.2.3 Wall extensibility $\phi$

Until now a direct measurement of  $\phi$  in vivo has not been published. The mean extensibility of the active zone has been reported instead (Pritchard et al. 1990). The Lockhart-Equation (2.4) delivers the distribution of  $\phi$ , for known distributions of  $Y$ ,  $p$  and  $REGR$ . If we assume that neither  $Y$  nor  $p$  change much along the root, it becomes clear that the distribution of  $\phi$  is more or less proportional to the  $REGR$  profile (Fig. 3.1).

In the last decade new insight into wall extensibility has occurred (see e.g. Pritchard 1994; Cosgrove 2000). Several affecting factors have been found, e.g. the wall proteins *expansins*, but the complete mechanism and controls of wall extension are still unknown. We propose an empirical approach based on an hypothetical enzyme deposited on the cell wall. The concentration of the enzyme  $c_e$  influences essentially the wall extensibility

$$\phi = \phi_{max} \frac{c_e}{K_{M,e} + c_e}, \quad (3.5)$$

where  $\phi_{max}$  is a maximal extensibility and  $K_{M,e}$  is a constant. As already mentioned,  $\phi$  is determined by several factors, and will only be proportional to  $c_e$  for small concentrations. For high  $c_e$ s the enzyme is not restricting and other factors have a central role. The simplest model describing this behavior is the basic

---

<sup>5</sup>Apoplast are the rooms in cells and tissues that are outside the plasmalemma, while the symplast define the inside of the plasmalemma.

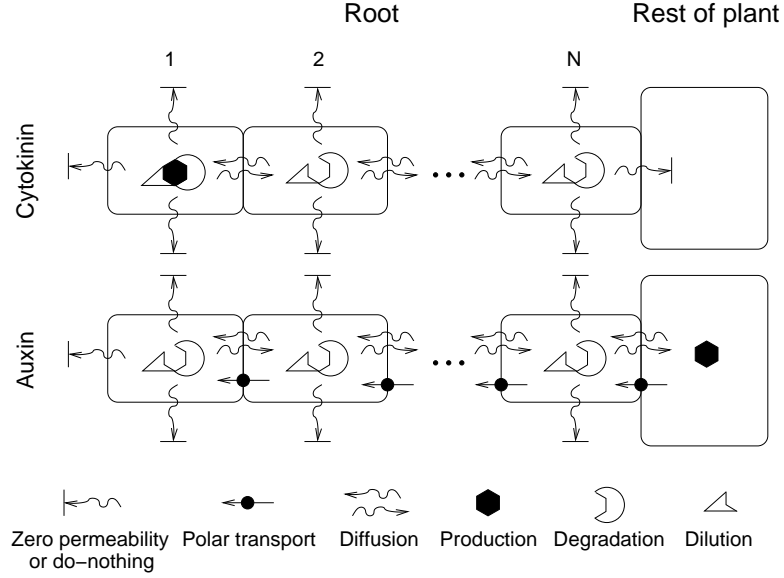


**Figure 3.3:** Schematic representation of the auxin and cytokinin transport equations. Auxin is transported polarly from the shoot towards the root apical cell, while cytokinin is solely transported by diffusion. The plant shoot is represented here by suitable boundary conditions. Both hormones are subjected to enzymatic degradation and growth dilution.

*Michealis-Menten* kinetics used in (3.5).

We assume that the enzyme concentration  $c_e$  on the wall satisfies

$$d_t c_e = \kappa_{prod}^e - (\kappa_{deg}^e + REGR) c_e, \quad (3.6)$$

where  $\kappa_{prod}^e$  and  $\kappa_{deg}^e$  are production and degradation rates. Dilution of the enzyme due to cell wall expansion, is described by the term containing  $REGR$ .<sup>6</sup>

### 3.2.4 Phytohormone transport

Reaction-diffusion equations are a suitable instrument to model biological development (Turing 1952; Prusinkiewicz and Rolland-Lagan 2006 and citations therein), including signal diffusion and positioning mechanisms. Two different approaches to model signal diffusion have been proposed: reaction-diffusion models and cell-to-cell transport models (Roussel and Roussel 2004). These differ essentially in the discretization involved in the resulting equations and are for

<sup>6</sup>Root cells grow almost unidirectional:  $d_t l \gg d_t l_w, d_t l_h$ . The dilution of the enzyme occurs on the expanding cell walls of area  $a_1 l$ , so that the dilution rate is  $d_t \ln(a_1 l) = d_t \ln V_{ol} = REGR$ .

small cell sizes equivalent (Hammer 1998; Roussel and Roussel 2004). While reaction-diffusion models are continuous and have to be discretized for numerical calculation, the cell-to-cell transport approach is intrinsically discrete. The conditions needed for an equivalence of both approaches are not satisfied in the model presented here, because cell size is not small compared to the distance scale over which concentration changes significantly. Thus, a cell-to-cell transport mechanism is used to model the positions of the different growth zones (division, elongation-only, saturation, and maturity).

The change in concentration of a phytohormone inside a cell can be represented by a sum of the following contributions

$$d_t c = (\partial_t c)_{diff} + (\partial_t c)_{trans} + (\partial_t c)_{dil} + (\partial_t c)_{prod} + (\partial_t c)_{deg} , \quad (3.7)$$

which are given by: *diffusion*, *transport*, *dilution*, *production* and *degradation*. Expressions for each of these contributions and suitable boundary conditions will be treated in the following. A schematic representation of the transport equations, and each of the contributions, are shown in Fig. 3.3.

### Diffusion

Assuming that the cell wall membrane complex of width  $h$  has a diffusion coefficient  $D_\alpha$  for the hormone  $\alpha$ , the amount exchanged by means of diffusion between cells  $k$  and  $k + 1$  is

$$a_0 D_\alpha^{app} \nabla_d^+ c_{\alpha,k} ,$$

where  $a_0$  is the base area of the cuboid approximating the cell,  $D_\alpha^{app} = D_\alpha l_k / h$  is an apparent diffusion coefficient and  $\nabla_d^\pm \circ := \pm (\circ_{k\pm 1} - \circ_k) / l_k$  is the forward or backward difference operator. Diffusion also occurs between cells  $k$  and  $k - 1$ , so that the net rate of change in amount  $s_{\alpha,k}$  in cell  $k$  is

$$(\partial_t s_{\alpha,k})_{diff} = a_0 D_\alpha^{app} (\nabla_d^+ c_{\alpha,k} - \nabla_d^- c_{\alpha,k}) = a_0 l_k D_\alpha^{app} \Delta_d c_{\alpha,k} ,$$

where  $\Delta_d \circ := \nabla_d^+ \nabla_d^- \circ = (\circ_{k+1} - 2 \circ_k + \circ_{k-1}) / l_k^2$  is the discrete Laplace operator. The concentration and the amount of a solute are connected through  $c = s / V_{ol}$ , which implies

$$(\partial_t c_{\alpha,k})_{diff} = D_\alpha^{app} \Delta_d c_k , \quad (3.8)$$

where  $V_{ol,k} = a_0 l_k$  was used and assumed to be constant in the differentiation, as dilution is accounted by the term  $(\partial_t c)_{dil}$ .

As expected, the diffusion contribution has the form of a discretized diffusion term. However, two different discretization could be used. We used here the cell length  $l_k$  as a discretization width, although we could have equivalently used

the thickness of the cell wall  $h$ . Both result in the same formal expression (3.8), but with different apparent diffusion coefficients.  $D_\alpha^{app}$  contains the relation of cell length to membrane thickness and depends hence on the coordinate, independently of the discretization used.

### Transport

Auxin is produced in the plant shoot and has to be transported actively into the root tip, in particular due to the continuous increase in distance between the tip and the shoot. This hormone is special in the sense that it undergoes basipetal polar transport in the shoot and acropetal polar transport in the root (Taiz and Zeiger 1991; Muday 2001). Active transport can, in contrast to diffusion, lead to accumulation in the root cap (Muday 2001; Perbal and Driss-Ecole 2003). The polarity of auxin transport makes it a very good candidate for positioning mechanisms (Blilou et al. 2005; Teale et al. 2005). It has been demonstrated to be transported through influx and efflux facilitator proteins (AUX and PIN<sup>7</sup>; Muday and DeLong 2001; Parry et al. 2001; Friml and Palme 2002). Further, its transportation velocity,  $4 \text{ mm h}^{-1}$  to  $10 \text{ mm h}^{-1}$ , is several times higher than that of diffusion (Sitte et al. 1998). The transport of auxin in the root tip is complex, as it is not only apical around the central cylinder, but also radial in the quiescent center and basipetal towards the elongation zone in the cortex cells (Fig. 5.1; Evans et al. 1986; Muday 2001; Perbal and Driss-Ecole 2003; Teale et al. 2005). However, the mean transport direction is apical towards the quiescent center.

The function of membrane transport systems is still not well understood. Elucidation of the function is hampered by the different transport proteins in membranes (Lüttge and Kluge 2002). However, a transport system can be approximated using the *Michaelis-Menten* formalism (Taiz and Zeiger 1991; Nobel 1999). Let the active transport system be acropetal, so that the amount of auxin,  $\alpha = 2$ , being transported from cell  $k + 1$  into cell  $k$  is

$$a_0 j_{max} \frac{c_{2,k+1}}{K_{M,2} + c_{2,k+1}},$$

where  $j_{max}$  is a maximal transport rate constant and  $K_{M,2}$  is the Michaelis-Menten constant of the system. Cell  $k$  transports, however, auxin into cell  $k - 1$

$$-a_0 j_{max} \frac{c_{2,k}}{K_{M,2} + c_{2,k}}.$$

---

<sup>7</sup>AUX and PIN proteins are located on the plasma membrane (pm), and facilitate the cellular influx and efflux of auxin, respectively. Their location on the pm is not fixed. For example, PIN proteins cycle continuously between the pm and endosomal compartments through vesicle trafficking (constitutive cycling; Royle and Murrell-Lagnado 2003; Swarup et al. 2005), and their distribution on the pm can react dynamic to upon application of chemicals (PIN1 and PIN2) or upon gravitropic stimulation of the organ (PIN3).

The net rate of change in concentration is then given by

$$(\partial_t c_{2,k})_{trans} = j_{max} \nabla_d^+ \left( \frac{c_{2,k}}{K_{M,2} + c_{2,k}} \right). \quad (3.9)$$

The transport direction is chosen by the discrete gradient operator. Here we chose  $\nabla_d^+$  reflecting an acropetal transport direction. If  $\nabla_d^-$  is used, the transport direction is basipetal. We should mention here that in a homogenization of (3.9), due to the continuity of the homogenized concentration, the term approximates a term with the logarithmic gradient  $j_{max} \nabla_d^+ \left( \frac{c_{2,k}}{K_{M,2} + c_{2,k}} \right) \rightarrow \mathbf{j}_{max} \cdot \nabla \ln(K_{M,2} + c_{2,k})$  for  $l_k \rightarrow 0$ . The transport direction in the homogenized version is taken then through the vector  $\mathbf{j}_{max}$  into account.

The transport term (3.9) represents the combination of efflux and influx facilitators. The nature of auxin transport is complicated. It has been shown that influx facilitators (AUX/LAX proteins) are as important in accumulation as efflux facilitator (PIN proteins; Kramer 2004; Swarup et al. 2005). Auxin seems also to promote its own transport out of cells (Paciorek et al. 2005), which complicates the modeling of the membrane transport system severely. Until now no quantitative mathematical model of this behavior is known to the author, although some similar approaches have been used in the modeling of shoot development (compare Prusinkiewicz and Rolland-Lagan 2006).

We assume that cytokinin is not actively transported at all, i.e. its transport is completely diffusive. This may be an erroneous assumption, as cytokinin is known to be transported by xylem and phloem. However, this assumption keeps the model as simple as possible and avoids excessively constraining the mechanism's possibilities.

### Dilution

Growth implies an uptake of water, resulting in a considerable dilution of solutes. A *Zea mays* (L.) root tip can locally grow with a rate of ca.  $50\% h^{-1}$ . Without compensation, a compound's concentration would fall to ca. 60% of its original value within one hour. Restitution can either be achieved by production or by active transport. We see here that dilution cannot be neglected, as other authors have (compare Prusinkiewicz and Rolland-Lagan 2006). The contribution of dilution is

$$(\partial_t c_{\alpha,k})_{dil} = -d_t \ln V_{ol,k} c_{\alpha,k} = -REGR_k c_{\alpha,k}. \quad (3.10)$$

### Production and degradation

We assume that cytokinin is produced at the root tip by the apical cell  $k = 1$

$$(\partial_t c_{1,k})_{prod} = \kappa_1^p \delta_{k1} , \quad (3.11)$$

where  $\kappa_1^p$  is a constant and  $\delta_{kj}$  is the *Kronecker*-symbol, which is defined as:  $\delta_{kj} = 1$  for  $k = j$  and 0 for  $k \neq j$ . Most auxin is produced in the plant shoot (Taiz and Zeiger 1991). We do not model the whole plant. It is therefore included into the transport equations through a boundary condition, so that the production rate vanishes:  $(\partial_t c_{2,k})_{prod} = 0$  for  $0 < k < N$ . We will treat the boundary conditions separately below.

The plant has to control the hormonal concentrations, for hormone regulation to be possible. This happens through regulation of the production and through suitable enzymatic degradation or conjugation. After a short time auxin transport leads to an accumulation in the apical cell. It is known that the root tip has the highest concentration of auxin in the root (Swarup et al. 2001). To avoid accumulation of huge amounts of auxin (high transport velocity:  $4 \text{ mm h}^{-1}$  to  $10 \text{ mm h}^{-1}$ ), the apical cell has to conjugate and/or degrade at a substantially higher rate than other cells do. To take this into account, degradation/conjugation of the hormones is described by

$$(\partial_t c_{\alpha,k})_{deg} = -(\kappa_{\alpha}^d + \kappa_{\alpha}^c \delta_{k1}) c_{\alpha,k} , \quad (3.12)$$

where  $\kappa_{\alpha}^d$  and  $\kappa_{\alpha}^c$  are constants. Conjugation is strictly not the same as degradation, as conjugated hormones may be de-conjugated for later use. The need of a higher conjugation/degradation rate in the apical cell, may be an artifact of the one dimensional model. Real roots seem to have an auxin recycling system (Teale et al. 2005; Swarup et al. 2005). Auxin transported acropetally into the apical meristem is redistributed radially towards the cortex cells and transported basipetally towards the shoot. However, it seems that the basipetal transport ends not far from the growth zone and PIN proteins may be involved in transport towards the central cylinder, i.e. auxin is cycled. The cycling could be part of a stabilization strategy.

### Boundary conditions

Boundaries could be classified into: *natural*, given by the geometry of the root, and *artificial*, created by treating only a subset of the whole system. The modeling of natural boundaries is normally more or less straightforward: the conservation equations are integrated into a thin layer around the boundary and letting the layer thickness go to zero (Giovangigli 1999). In contrast, artificial boundaries are extremely challenging because the missing information has to be meaningfully provided without excessively disturbing the solution. Choosing conditions on artificial boundaries is a fundamental question, in particular because not always the whole system can be modeled or simulated (see e.g. Quarteroni et al. 2000 for the

case of vascular fluid dynamics).

We introduced an artificial boundary to avoid a treatment of the shoot. We therefore have to give suitable boundary conditions. We propose the following

- No diffusion into the surroundings of the cell string (homogeneous *Neumann* condition). Reduces to a condition for  $k = 1$ :

$$(\partial_t c_{\alpha,1})_{diff} = D_{\alpha}^{app} \nabla_d^+ c_{\alpha,1}, \quad \text{for } k = 1.$$

- Cytokinin fulfills the *do-nothing* condition<sup>8</sup> on the artificial boundary ( $k = N$ ):

$$(\partial_t c_{1,N})_{diff} = -D_1^{app} \nabla_d^- c_{1,N}, \quad \text{for } k = N.$$

- The missing plant shoot is represented by an auxin source, which produces an influx through the artificial boundary. The concentration  $c_2^{in}$  in the source changes with rate:

$$d_t c_2^{in} = \kappa_2^{in} - \frac{j_{max}}{\bar{l}} \frac{c_2^{in}}{K_{M,2} + c_2^{in}},$$

where  $\kappa_2^{in}$  is a constant production rate and  $\bar{l}$  is a mean cell length. This boundary condition can be identified with a *Dirichlet* condition for  $c_2$ .

### Transport equations

Combining all the contributions and boundary conditions, we obtain the following transport equations

*Cytokinin* :

$$d_t c_{1,k} = \begin{cases} D_1^{app} \nabla_d^+ c_{1,1} + (\kappa_1^p - \kappa_1^d - \kappa_1^c - REGR_1) c_{1,1} & , \quad k = 1 \\ -D_1^{app} \nabla_d^- c_{1,N} - (\kappa_1^d + REGR_N) c_{1,N} & , \quad k = N \\ D_1^{app} \Delta_d c_{1,k} - (\kappa_1^d + REGR_k) c_{1,k} & , \quad \text{else} \end{cases} \quad (3.13)$$

<sup>8</sup>The *do-nothing* condition for a partial differential equation is found through the *weak* formulation of the equations. Here, the do-nothing condition becomes the same as a homogeneous Neumann condition, which means that the concentration becomes constant.

$$\begin{array}{l}
\text{Auxin :} \\
d_t c_{2,k} = \begin{cases} D_2^{app} \nabla_d^+ c_{2,1} - (\kappa_2^d + \kappa_2^c + REGR_1) c_{2,1} + \\ \quad + j_{max} \frac{c_{2,2}}{K_{M,2} + c_{2,2}} & , \quad k = 1 \\ -D_2^{app} \nabla_d^- c_{2,N} - (\kappa_2^d + REGR_N) c_{2,N} + \\ \quad + j_{max} \nabla_d^+ \left( \frac{c_{2,N}}{K_{M,2} + c_{2,N}} \right) & , \quad k = N \\ D_2^{app} \Delta_d c_{2,k} - (\kappa_2^d + REGR_k) c_{2,k} + \\ \quad + j_{max} \nabla_d^+ \left( \frac{c_{2,k}}{K_{M,2} + c_{2,k}} \right) & , \quad \text{else} \end{cases} \\
C_{2,N+1} = c_2^{in} \\
d_t c_2^{in} = \kappa_2^{in} - \frac{j_{max}}{l} \frac{c_2^{in}}{K_{M,2} + c_2^{in}}
\end{array} \tag{3.14}$$

Refer to Fig. 3.3 for a schematic representation of the equations with their boundary conditions.

### 3.2.5 Cell division

The different phases that a cell undergoes are closely related to its division rate. We will denote here the division rate by  $\theta$ . Beemster and Baskin (1998) analyzed the growth and division rates of *Arabidopsis thaliana* (L.) Heynh. roots. Their measurements show that the distribution of the division rate is almost constant up to a certain distance from the quiescent center. From this distance on, the division rate is reduced drastically until it reaches zero. This finding leads to a step function to model the field of division rate. The division rate of cell  $k$  is then

$$\theta(x_k(t)) := \begin{cases} \theta_0 & \text{for } 0 \leq x_k(t) < x_{el} \\ 0 & \text{elsewhere} \end{cases} , \tag{3.15}$$

where  $x_k(t)$  is the position of cell  $k$  at time  $t$ ,  $\theta_0$  is a positive constant and  $x_{el}$  describes the position where the cell stops dividing.  $x_{el}$  is however not necessarily constant in time and the same for each cell. In Section (3.2.6), we will present how  $x_{el}$  is determined in each cell.

We assume that the division process is symmetric, i.e. the daughter cells have half the mother's length, while all other properties are passed without modification. This implies that the concentration  $c_\alpha$  of phytohormones or the concentration of cell wall  $c_e$  are not affected by division. Additionally, the division process does not affect the overall tissue length, i.e. before and after a division the tissue has the same length.

We still have not cleared why  $\theta$  is so important to model the *REGR* distribution. The answer to this question is simple: cells which divide have to grow. This

occurs in contrast to expansion growth (water uptake) by cytoplasm production. Even so, a cell must double roughly its volume before it divides. High resolution measurements of cell length suggest the existence of a critical length indispensable for division to occur (Ivanov and Maximov 1999). This is supported by high spatial resolution growth measurements, which show a more or less constant *REGR* in the meristem and a sudden transition into the elongation zone (Fig. 3.1; van der Weele et al. 2003). The growth in the meristematic region is highly correlated to proliferation. The average of the relative growth rate over time in the meristem can be easily estimated. Let  $\tau := \theta_0^{-1}$  denote the cell cycle time lapse. The cell length averaged over time at a fixed position in the meristem should be time independent, otherwise after a certain time  $T \gg \tau$ , the size of meristematic cells would approach either zero or infinity. This is particularly true for the apical cells, which stay in the meristem at all times. Conservation of average length is guaranteed when cells double their size in one cell cycle, i.e.  $l(t + \tau) = 2l(t)$ . This implies that cell length in the meristem is  $\tau$  periodic. The average of a periodic function is given by the average over one period. Hence, in the meristem the average relative growth rate over time is given by

$$\overline{REGR}_{Mer} = \frac{1}{T} \int_0^T \frac{1}{l} d_t l dt = \frac{1}{\tau} \int_0^\tau d_t \ln l dt = \frac{1}{\tau} \ln \frac{l(\tau)}{l_0},$$

where  $l_0 = l(0)$  is the minimal and  $l(\tau)$  is the maximal cell length. Thus, the average *REGR* in the meristem is:

$$\overline{REGR}_{Mer} = \theta_0 \ln 2, \quad (3.16)$$

i.e. the average over time is essentially given by the division rate. This is in accord with the finding of Beemster et al. (2003) that in the apical meristem cells divide and grow at similar rates.

An expression for the average cell length over time in the meristem is also easily obtained. The length of meristematic cells, like the *REGR*, is a periodic function; we obtain thus the time-averaged cell length

$$\bar{l}_{Mer} = \frac{1}{\tau} \int_0^\tau l dt = \frac{\theta_0}{\overline{REGR}_{Mer}} \int_0^\tau d_t l dt,$$

and after integration and use of  $l(t + \tau) = 2l(t)$

$$\bar{l}_{Mer} = l_0 / \ln 2. \quad (3.17)$$

### 3.2.6 Assembling the model

Each cell in the string has its own growth rate, turgor, osmotic potential, wall extensibility, etc. These can be described by vector functions with an increasing

dimension. We assume that  $Y, L_p, a_0, a_1, \alpha, \overline{\psi}_s, \phi_{max}, K_{M,e}, P_\alpha, j_{max}, K_{M,2}$  and  $\kappa_\alpha^d$  are the same for all cells. The division process is modeled as described above in Section 3.2.5.

The transitions between division, elongation-only and maturity are controlled by the ratio function  $\omega(c_1, c_2)$ . This function may be thought of a sensing mechanism inside the cell. Transition into elongation-only or into saturation is accomplished when  $\omega$  reaches certain critical values  $\omega_{el}$  or  $\omega_{sat}$ . Because the concentrations of hormones depend on position and thus on cell index  $k$ , the ratio function  $\omega_k = \omega(c_{1,k}, c_{2,k})$  allows the cells to obtain information on their position. Coordination of the growth zone becomes therefore possible.<sup>9</sup> We selected here the empirical ratio function  $\omega = c_1/c_2$ , as it suffices to describe the action of auxin ( $c_2$ ) on the growth distribution.

Changes in wall extensibility  $\phi_k$  reflect the transition into a new phase.  $\omega_k$  does not act directly on the wall extensibility, as the transitions are mediated through the production and degradation of the cell wall enzyme. It acts thus on the rates of these processes

$$\begin{aligned}\kappa_{p,k}^e &= \kappa_{p,div}^e \theta(\omega_{el} - \omega_k) + \kappa_{p,el}^e \theta(\omega_k - \omega_{el}) \theta(\omega_{sat} - \omega_k), \\ \kappa_{d,k}^e &= \kappa_{d,sat}^e \theta(\omega_k - \omega_{sat}),\end{aligned}\quad (3.18)$$

where  $\kappa_{p,div}^e, \kappa_{p,el}^e$  and  $\kappa_{d,sat}^e$  are constants corresponding to production and degradation rates in the division, elongation and saturation phases,  $\theta(x)$  is the Heaviside function<sup>10</sup> and  $\omega_{el}$  and  $\omega_{sat}$  are constant thresholds.

Eq. (3.18) connects the phytohormone distributions to the growth equation (3.1). Through this equation the plant is able to influence root tip growth by increasing or decreasing the phytohormone concentrations:

$$\kappa_2^{in}, \kappa_1^p \rightarrow \omega_k \rightarrow \kappa_{p,k}^e, \kappa_{d,k}^e \rightarrow \phi_k \rightarrow REGR_k.$$

To obtain distributions of cell properties, as turgor,  $REGR$ , etc., the cell coordinates are needed. We define these to be at the cell center, so that the velocity  $v_k$  and coordinate  $x_k$  of cell  $k$  are

$$\begin{aligned}x_k &= x_{k-1} + (l_k + l_{k-1})/2 & x_1 &= l_1/2, \\ v_k &= v_{k-1} + (d_t l_k + d_t l_{k-1})/2 & v_1 &= d_t l_1/2.\end{aligned}$$

---

<sup>9</sup>The model assumes that all cells in the string, which represents the root tip, sense their distance to the quiescent center resulting in coordination of the growth zone. However, in a real root only selected cells may be sensing the distance and determine through cell wall stiffening the end of the growth zone (e.g. stiffening of the young vascular tissue). As long as the model is one dimensional, these two do not differ.

<sup>10</sup>The Heaviside function is defined as  $\theta(x) = 1$  for  $x \geq 0$  and  $\theta(x) = 0$  else, and should not be confused with the division rate of Section 3.2.5. This division rate can be defined as  $\theta'(x_k(t)) := \theta(x_k(t) - x_{el})$ .

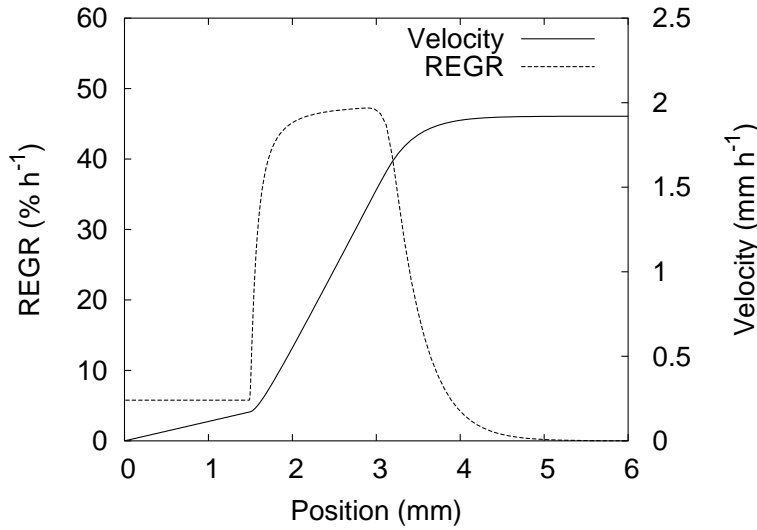


**Figure 3.4:** Mean velocity and *REGR* distributions (averaged over  $t = 120 h$  to  $300 h$ ). Transition into elongation-only occurs at ca.  $1.5 mm$  from the tip, while saturation begins at  $3 mm$ .

### 3.3 Simulation, results and discussion

In this section we would like to present simulations of a one dimensional root and to discuss the results in the light of experimental results. First we will show the distributions and cell characteristics predicted by the model. Then the behavior of the model to an increase in auxin production is presented. The simulation is based on Eqs. (3.1), (3.4), (3.6), (3.13) and (3.14). These ordinary differential equations are solved numerically by an *explicit Euler scheme* on an equally discretized time mesh of width  $10^{-3} min$ . At each time step  $\phi_k$ ,  $\kappa_{p,k}^e$  and  $\kappa_{d,k}^e$  were determined for all cells using the distributions of phytohormones together with the ratio function  $\omega$  and Eqs. (3.5) and (3.18).

Simulation starts with two initial cells. These have the initial properties found in Table 3.1, where also the simulation parameters can be found. The parameters were chosen so that a typical *Zea mays* (L.) root is resembled. The cell width and height were chosen as:  $l_w = 10 \mu m$  and  $l_h = 10 \mu m$ .

#### 3.3.1 Growth distribution and cell properties

The predicted distributions of velocity and *REGR* along the root are shown in Fig. 3.4. These were averaged over  $t = 120 h$  to  $300 h$ , because of oscillations in the distributions (compare Fig. 3.8). In contrast to the wide accepted notion of a gradual increase of *REGR* in the meristematic region (Erickson and Sax 1956),

**Table 3.1:** Parameters chosen to resemble a typical *Zea mays* (L.) root. I) Initial conditions. II) Cellular parameters: division rate  $\theta_0$  ( $h^{-1}$ ), yield threshold  $Y$  ( $MPa$ ), water conductivity  $L_p$  ( $\mu m \min^{-1} MPa^{-1}$ ), osmoregulation rate coefficient  $\zeta$  ( $\min^{-1}$ ) and set-point osmotic potential  $\overline{\psi}_s$  ( $MPa$ ), elongation and saturation thresholds of auxin/cytokinin ratio ( $\omega_{el}$  and  $\omega_{sat}$ ). III) Parameters used in phytohormone production, artificial boundary condition and wall enzyme production. Units:  $[l] = \mu m$ ,  $[\psi_s] = MPa$  and  $[c_e], [c_1], [c_2], [c_2^{in}] = mmol m^{-3} \min^{-1}$ ,  $[P_\alpha] = \mu m \min^{-1}$ ,  $[*] = mmol m^{-3} \min^{-1}$ ,  $[\dagger] = \min^{-1}$ ,  $[j_{max}] = mmol m^{-2} \min^{-1}$ ,  $[\ddagger] = mmol m^{-3}$ ,  $[\bar{l}] = \mu m$  and  $[\phi_{max}] = \min^{-1} MPa^{-1}$ .

<b>I Initial conditions</b>						
$l$	$\psi_s$	$c_e$	$c_1$	$c_2$	$c_2^{in}$	
10	-0.5	0.0408	0.1	0	$10^{-4}$	
<b>II Cellular parameters</b>						
$\theta_0$	$Y$	$L_p$	$\zeta$	$\overline{\psi}_s$	$\omega_{el}$	$\omega_{sat}$
1/12	0.2	60	-0.1	-0.5	0.2	6
<b>III Hormonal parameters</b>						
Hormone	$P_\alpha$	$\kappa_\alpha^{p*}$	$\kappa_\alpha^{d\dagger}$	$\kappa_\alpha^{c\dagger}$	$j_{max}$	$K_{M,2}^{\ddagger}$
Cytokinin, $\alpha = 1$	20	0.2	$45 \times 10^{-4}$	—	—	—
Auxin, $\alpha = 2$	20	—	$10^{-4}$	4	100	$2 \times 10^{-2}$
Boundary	$\kappa_2^{in*}$	$\bar{l}$				
	$10^{-2}$	100				
Wall enzyme	$\kappa_{p,div}^e$	$\kappa_{p,el}^e$	$\kappa_{d,sat}^e$	$\phi_{max}$	$K_{M,e}^{\ddagger}$	

the model shows an abrupt transition between the division and the elongation-only zones (Fig. 3.4). Recent measurements of van der Weele et al. 2003 and Ivanov and Maximov 1999 confirm for several species a more or less constant *REGR* in the meristem and an abrupt acceleration in the elongation zone (Fig. 3.1). The sharp increase in growth indicates a change in the mechanism of cell expansion (Ivanov and Maximov 1999). The differences between these notions of meristematic growth can be explained by the smoothing procedures needed in the determination of the *REGR* profiles. Sigmoidal fits of the velocity profiles have been used traditionally for the determination of the *REGR* distribution (Morris and Silk 1992). A gradual growth increase is intrinsic to a sigmoidal velocity profile, so that it does not surprise that the fit ignores the sudden change in *REGR*. Modern methods allow the determination of *REGR* profiles more accurately (Walter et al. 2002; van der Weele et al. 2003) and confirm this behavior.

Cytokinin, produced in the apical cell, falls quickly along the root axis, while auxin accumulates in the apical cell and is almost constant elsewhere (Fig. 3.5). The different degradation rates allow a monotonic ratio function  $\omega$  and thus an adequate positioning mechanism (Fig. 3.5). Auxin accumulation occurs due to the polar transport, and measurements of IAA<sup>11</sup> concentration along root apices of *A. thaliana* confirm its existence (Swarup et al. 2001). Accumulation in the columella is the basis of the *fountain model* of auxin transport and consequently of *gravitropism* models (see e.g. Chen et al. 1999; Blancaflor and Masson 2003; Perbal and Driss-Ecole 2003). Auxin gradients, produced by an interplay between polar transport and diffusion, are good candidates for positioning mechanisms (Blilou et al. 2005; Teale et al. 2005).

The model does not take the sub-cellular distribution of auxin into account, although the cell can be treated as being composed of three adjacent compartments: cell wall, cytoplasm and vacuole (Kramer 2004). Treating the cell as an homogeneous entity has mainly an effect on the calculation of the active hormone concentrations, as the amount of active hormone is not distributed in the whole cell volume. However, although the physiological effects of auxin are well documented (Taiz and Zeiger 1991), the complete mechanism behind auxin sensing is still unclear. It does not make much sense to take a sub-cellular distribution into account, while the relevant compartment is still unknown. Nonetheless, the simplified model is enough to describe the concentration gradients qualitatively (Swarup et al. 2001). A more extensive approximation of cellular and sub-cellular auxin transport can be found in Kramer 2004.

Cell length along the root axis is subjected to strong variations. A snapshot at  $t = 270 h$  and the averaged distribution (from  $t = 120 h$  to  $300 h$ ) are shown

---

<sup>11</sup>IAA: Indole-3-acetic-acid, the most relevant auxin.

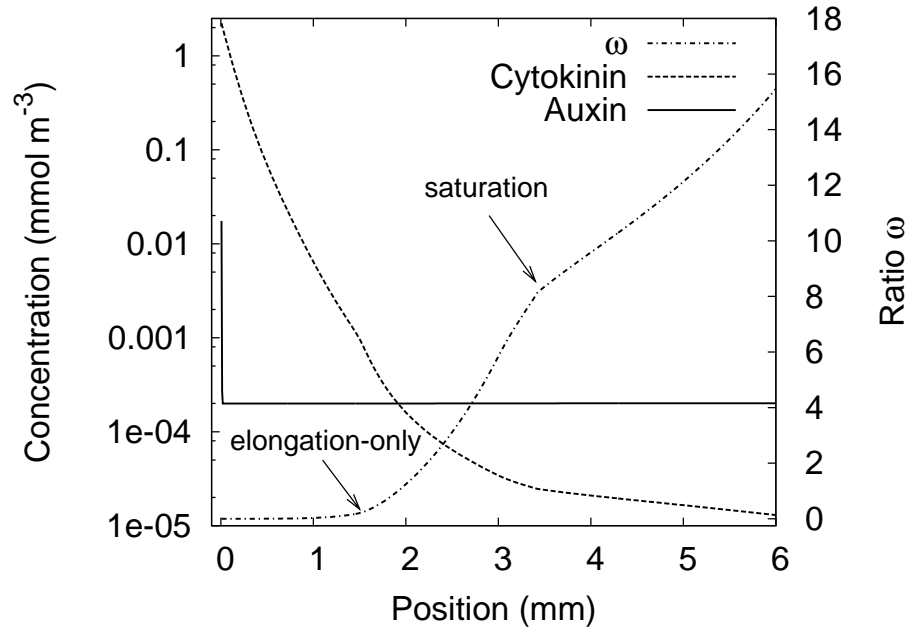


**Figure 3.5:** Distribution of auxin, cytokinin and their ratio function  $\omega$  ( $t = 270$  h).

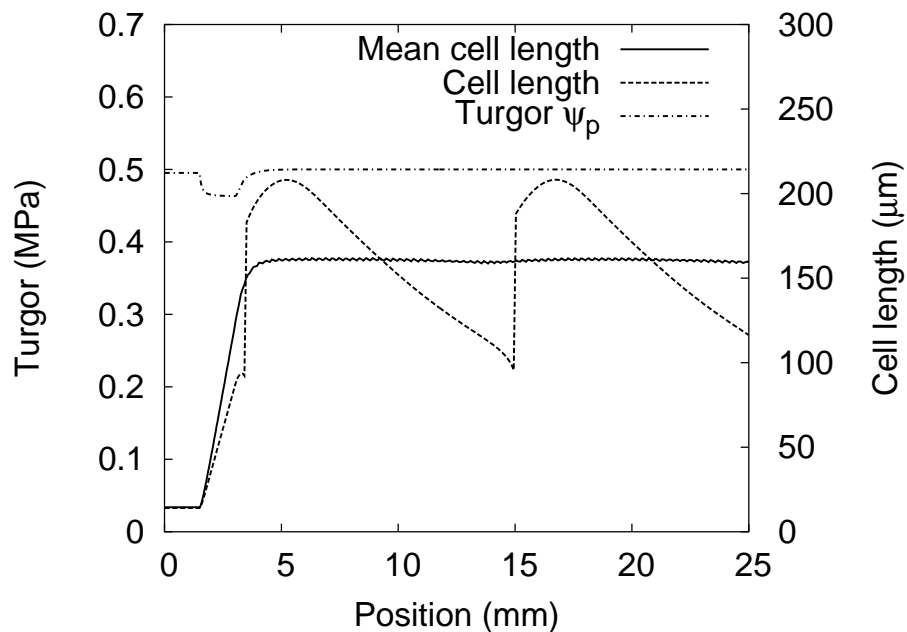


**Figure 3.6:** Distribution of turgor  $\psi_p$  and cell length along the root axis ( $t = 270$  h). The mean cell length distribution is also shown (averaged over  $t = 120$  h to 300 h).

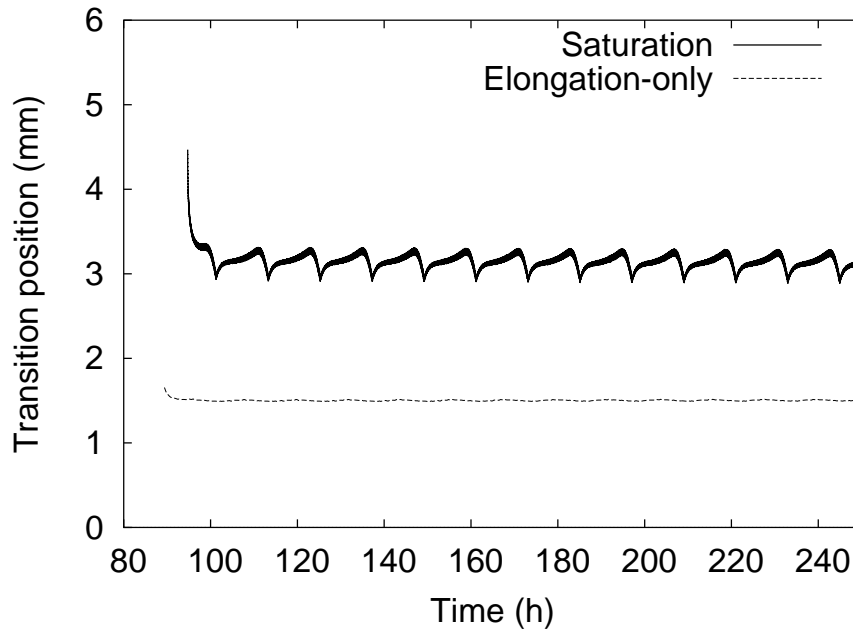


**Figure 3.7:** Positions of transition into elongation-only and saturation phases. Transition into saturation shows strong oscillations with a period of one cell cycle (12 h), and additionally superimposed quantization effects.

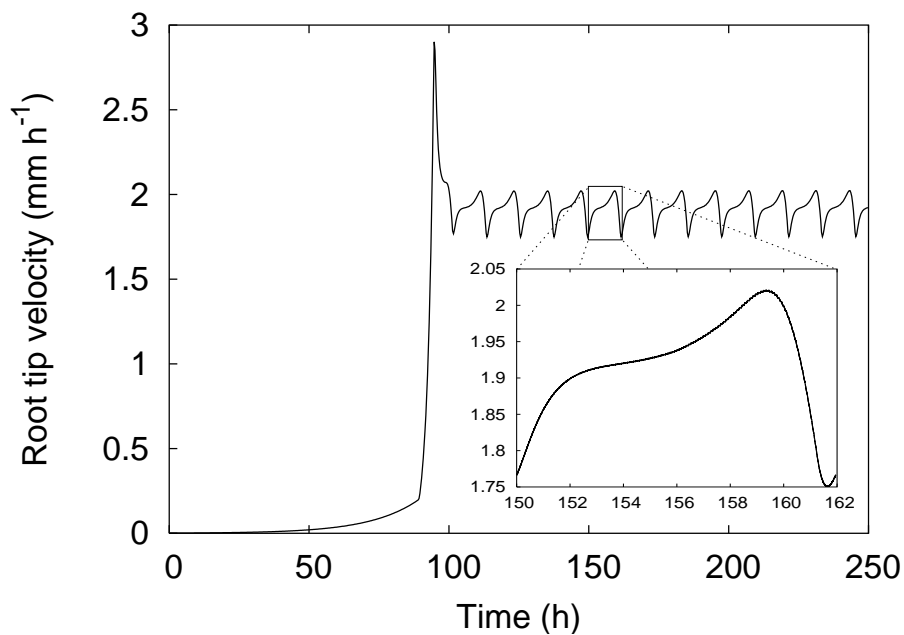


**Figure 3.8:** Velocity of root tip against time since “germination”. Oscillation of the saturation position produces a strong variation in the tips velocity.

in Fig. 3.6. Cell division is responsible for the oscillation in cell length distribution. The transition into elongation only and into saturation depend only on  $\omega$ , and hence only on the phytohormone concentrations. Thus, division and transition into elongation-only are not coordinated, resulting in varying terminal cell lengths. Because cell division is perfectly synchronized in the model, the variations in cell length distribution are regular. However, a real root does not have such a complete synchronization, explaining why irregular strong variations of cell length have been reported (see Fig. 8 in Pritchard et al. 1990).

The turgor  $\psi_p$  distribution is almost constant along the root (Fig. 3.6), with a slight deviation in the elongation-only zone due to the higher wall extensibility [Eq. (3.2)]. Pritchard et al. (1993) found the turgor to be constant, but a careful inspection of their Figures shows that the turgor falls slightly. The cause of this is not certain. Either the osmoregulation is not fast enough to counteract dilution, or the increasing wall extensibility causes the turgor to fall [compare Eq. (3.2)]. Water and solute supply is chimeric in the root tip: symplastic and apoplastic (Pritchard et al. 2000; Boyer and Silk 2003). A substantial amount of the solutes are not subjected to dilution, as they are supplied symplastically (phloem). A slow osmoregulation is thus improbable. The model shows that due to the higher wall extensibility in the elongation-only zone, the turgor falls not more than  $0.05 \text{ MPa}$  (Fig. 3.6). Pritchard et al. (1993) showed, however, that the turgor falls continuously at the basal end of the elongation-only zone for more than  $0.1 \text{ MPa}$ . The cell extensibility can thus not be the cause. A heterogeneous deposition rate of osmotically active compounds (Walter et al. 2003) may be responsible for an increasing osmotic potential and consequently for a decreasing turgor. It becomes clear that modeling the distribution of osmotically active compounds is essential for the description of the turgor distribution.

The elongation-only zone and consequently the growth of the whole root is characterized by the position of the transition into elongation-only and saturation (Fig. 3.7). Transition into elongation-only occurs after a short stabilization phase at an almost constant position. Because no basal meristem is modeled, this position equals the meristem size. The transition into saturation is superimposed by an oscillation with a period of the cell division time ( $12 \text{ h}$ ). Quantization effects overlay the oscillation making the transition position fuzzy.

The dimension of the elongation-only zone determines the velocity of the root tip (Fig. 3.8). The oscillation found in the saturation position is therefore transferred into the tip's velocity. Slight quantization effects are visible in the magnified section. Oscillations of the root tip are well documented and have been shown to depend on several environmental factors as nutrient availability (Walter et al. 2003; Walter and Schurr 2005). It is however still unknown how they occur, although a model based on two circular growth waves linked to ion-fluxes has been

proposed (Shabala and Newman 1997).

Figs. 3.9 and 3.10 show the time evolution of the wall extensibility, velocity, osmotic potential and cell length of a chosen cell. A cell is  $\sim 7 h$  in the elongation-only zone, which is considerable less than the cell cycle time ( $12 h$ ), as becomes clear from the evolution of wall extensibility. The time evolution of the cell's velocity shows that the cell accelerates exponentially until a maximum velocity is reached (same as the root tip velocity). The proposed osmoregulation maintains the osmotic potential as near as possible to the set-point value  $\bar{\psi}_s = -0.5 MPa$ . Even so, dilution can be clearly seen. As with the velocity, the cell length grows exponentially until the mature cell size is reached.

### 3.3.2 Auxin change

We examine in this Section the behavior of the model to changes in auxin production rate. Such auxin concentration changes correspond to the shoot sending information to the root to control/influence growth. Two situations are examined. First, a sudden increase in auxin production is simulated and the reaction of the root tip's velocity is determined (Fig. 3.11). Second, to understand the effects on the velocity, the dependence of the meristem and elongation-only zone dimension on the production rate was determined (Fig. 3.12).

Growth, in particular the size of the meristem and elongation-only zone, depends on the auxin production rate. This was simulated by a sudden change in auxin production rate  $\kappa_2^{in}$  after the root stabilized from the germination process. Fig. 3.11 shows the root tip velocity versus time. At  $t = 150 h$  the production rate  $\kappa_2^{in}$  was increased tenfold from  $10^{-2}$  to  $10^{-1} mmol m^{-3} min^{-1}$ . After the change, the tip slows abruptly down to  $0.9 mm h^{-1}$  for one hour, and rises then to oscillate around  $1.4 mm h^{-1}$ , which is considerably lower than before the change ( $1.8 mm h^{-1}$ ). Beemster and Baskin (2000) found that a synthetic auxin (2,4-dichlorophenoxyacetic acid) applied exogenously to *Arabidopsis thaliana* (L.) Heynh. roots reduced the tip velocity substantially. This is consistent with our model results. It is noteworthy that not only the mean velocity changed, but also the amplitude of the oscillation increased by a factor of 1.5.

The size of the division zone (meristem) and elongation-only zone were determined for a variable production rate  $\kappa_2^{in}$  (Fig. 3.12). This was achieved by changing  $\kappa_2^{in}$  suddenly at  $t = 150 h$  from  $10^{-2} mmol m^{-3} min^{-1}$  to a new value between  $2 \times 10^{-5}$  and  $2 \times 10^{-1} mmol m^{-3} min^{-1}$ . For each new value a new simulation was started. Meristem and elongation-zone size fall with increasing auxin production (Fig. 3.12). Beemster and Baskin (2000) determined the *REG*R distribution after application of auxin and found that the elongation-only

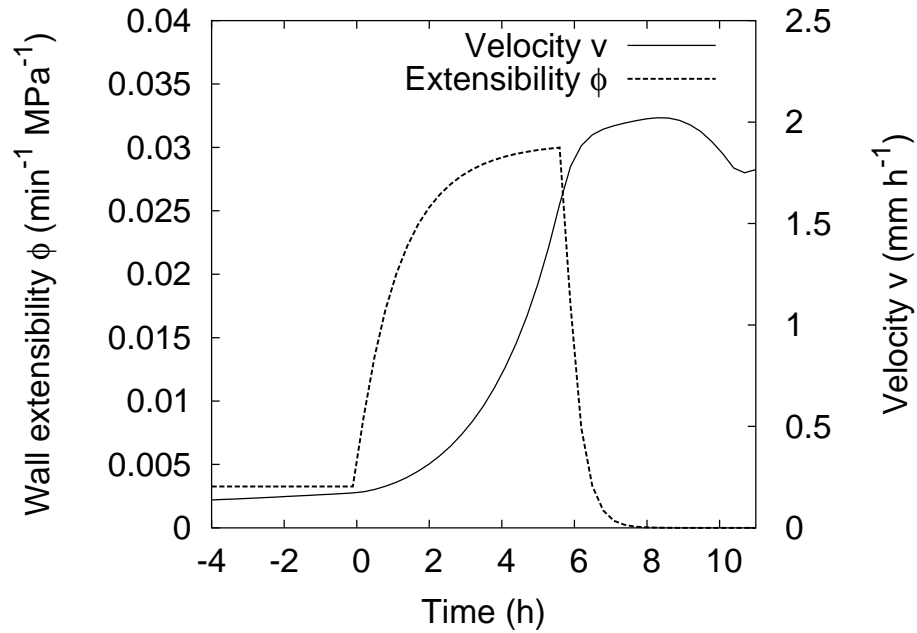


**Figure 3.9:** Evolution of wall extensibility and velocity of a chosen cell. Time axis chosen so that transition into elongation occurs at  $t = 0$  h. Cell velocity increases exponentially until it reaches after ca. 7 h the velocity of the root tip, which oscillates (compare Fig. 3.8).

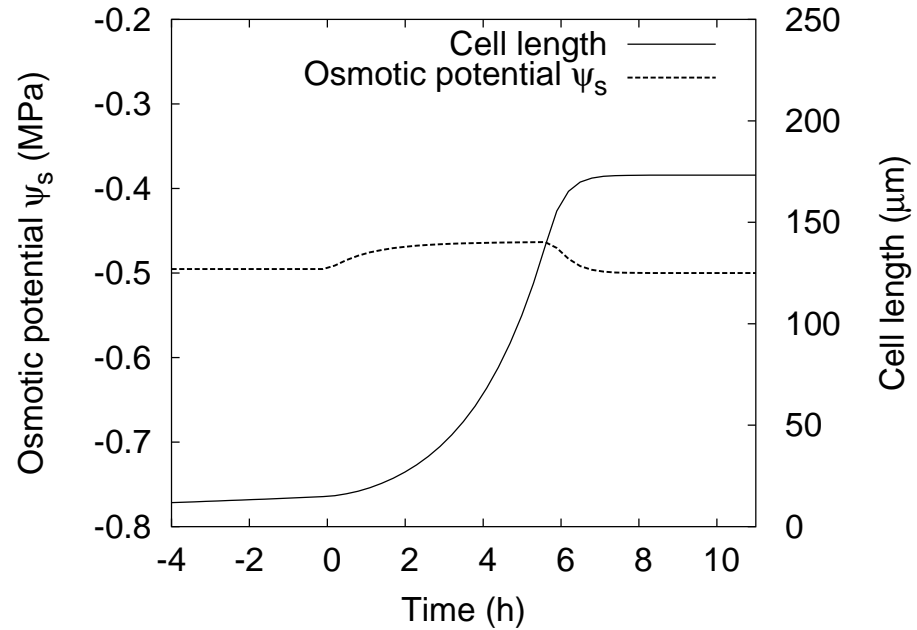


**Figure 3.10:** Evolution of cell length and osmotic potential of a chosen cell. Cell length increases exponentially until saturation. Dilution effects are clear in the evolution of osmotic potential. Time axis chosen as in Fig. 3.9.

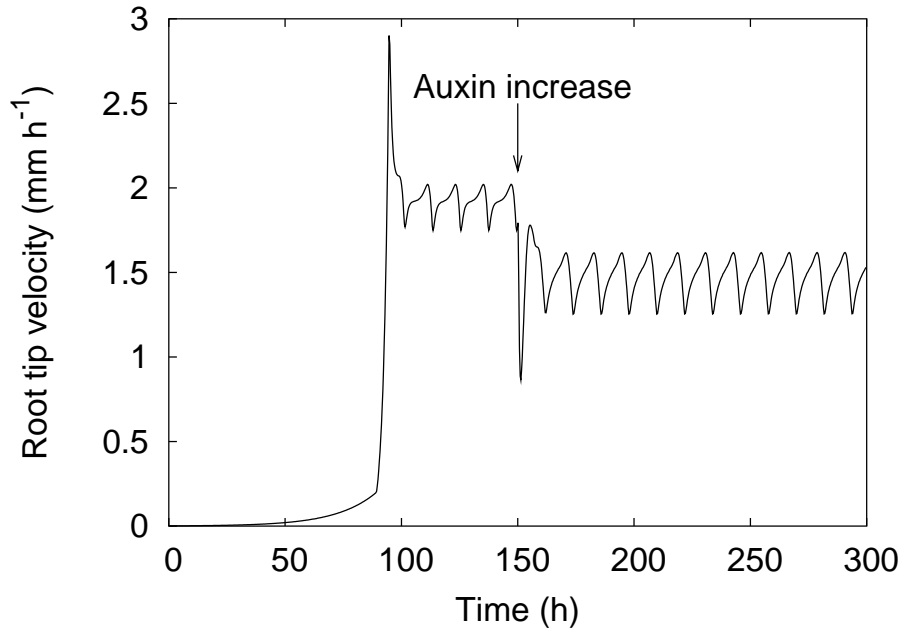


**Figure 3.11:** Reaction of the root tip to a tenfold increase of auxin production (i.e.  $\kappa_2^{in} : 10^{-2} \mapsto 10^{-1} \text{ mmol m}^{-3} \text{ min}^{-1}$ ).

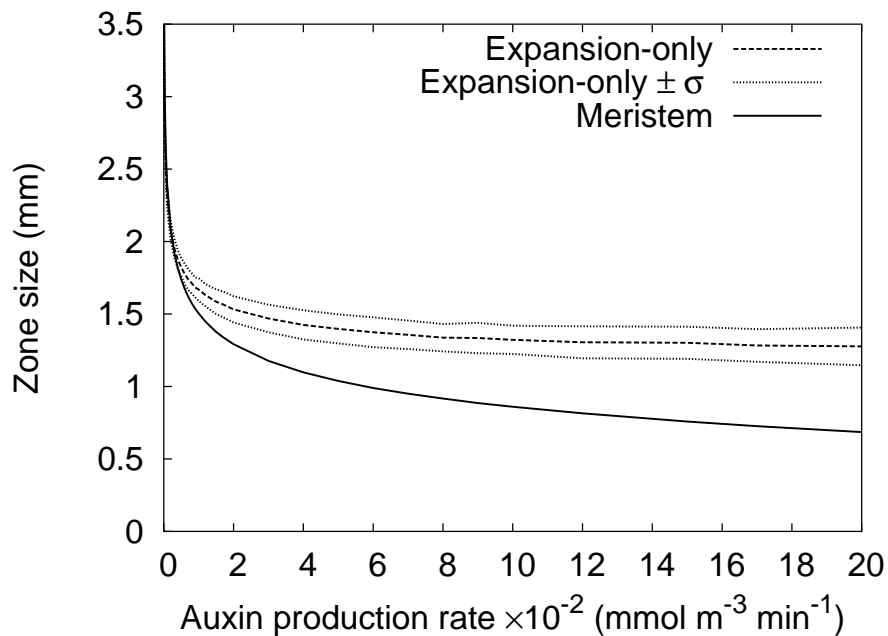


**Figure 3.12:** Dependence of the division zone (meristem) and elongation-only zone dimensions on auxin production rate  $\kappa_2^{in}$  (original rate:  $10^{-2} \text{ mmol m}^{-3} \text{ min}^{-1}$ ).

zone narrows and shifts towards the quiescent center without a change in maximal *REGR*. Hence, auxin affects the distribution of wall extensibility rather than the wall extensibility itself. The model presented here behaves similarly. On increasing auxin production the meristem size, which corresponds to the transition position into elongation-only, shifts towards the apical cell and the elongation-only zone shrinks. Beemster and Baskin (2000) found in contrast to the models prediction the meristem, defined as the division active zone and independent of elongation, to shift basally on application of auxin. This discrepancy between measurements and model can be explained either by the measurement method used (Beemster and Baskin 2000), or by the strict separation between elongation and division assumed in this model (Section 3.2.5). On the one hand, the method used by Beemster and Baskin 2000 to measure the *REGR* distributions relies on a small number of markers and has thus no high spatial resolution. On the other hand, a strict separation between cell division and elongation is improbable.

### 3.3.3 Conclusion

The auxin- and cytokinin-like properties given to the two hypothetical phytohormones are essential to the control of the model's root elongation zone. The cytokinin-like hormone produces mainly a gradient, which is modulated by the concentration of the auxin-like hormone. A similar strategy may be used in real primary roots to control the root elongation zone. These two hormones may be part of a positional system, which allows the root cells to obtain information on their position along the root axis. The effects of auxin on the elongation zone (Beemster and Baskin 2000) and the sudden change between meristematic and elongative growth support this view (Ivanov and Maximov 1999; van der Weele et al. 2003). Plants may influence this positional system by changing the production and/or distribution of auxin and cytokinin. This seems to be the main strategy involved in the gravitropic reaction, where the axial auxin redistribution is shifted towards one side to produce curvature. The model shows that a plant shoot is able to influence root growth by changing the production of auxin, and provides a sound basis for extension into gravitropism models. The refinement of the growth equation allows a connection to models of biomechanics and water uptake, so that the influences of soil properties on root growth may be modeled. Solute uptake, transport and deposition is essential for root growth. The model is too simplistic in this point and should be extended to include the transport and deposition of solutes, in particular because of the importance of carbohydrates in the growth process and osmotic active solutes in water uptake. It became also clear that a strict separation between division and elongation restricts the model too much. However, allowing both to overlay complicates the numerical treatment of the problem substantially (particularly in multidimensional models). The mechanism involved in auxin signaling and action are still too unknown and oblige the use of an empirical ratio function.

# Chapter 4

## Curvature Phenomena

### 4.1 Introduction

Differential growth in cylindrical organs, such as roots and hypocotyls, is a complex process that involves changes in transcription and dynamic alteration of protein expression patterns (Muday 2001; Friml and Palme 2002; Friml et al. 2002; Blilou et al. 2005; Teale et al. 2005). Quantitative analysis of growth and differential growth is a prerequisite to understand the molecular organization of this process.

Several concepts have been used to characterize curvature of cylindrical organs. The three most noticeable being probably: differential relative elemental growth rate (*REGR*) distributions (Silk and Erickson 1978; Silk 1989; Ishikawa and Evans 1993; Zieschang et al. 1997; Mullen et al. 1998a), the curvature  $\kappa$  (e.g. Silk and Erickson 1978; Silk 1989; Selker and Sievers 1987; Zieschang and Sievers 1991) and distributions of curvature angle (Mullen et al. 1998b; Mullen et al. 2000; Wolverton et al. 2002a; Wolverton et al. 2002b).

Differential *REGR* distributions and the rate of change of curvature ( $d_t\kappa$ ) have been shown to be equivalent (Silk and Erickson 1978; Silk 1989; Zieschang et al. 1997). However, differential *REGR* profiles are prone to errors, because the traditional method to measure *REGR* distribu-

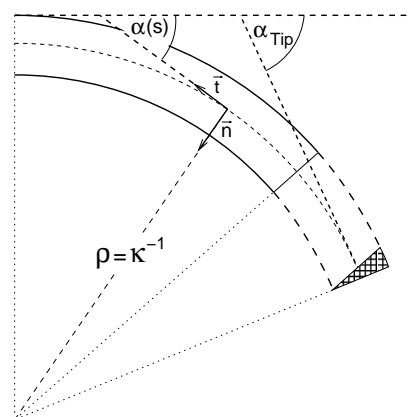


**Figure 4.1:** Cylindrical organ which grows and curves.  $\rho$  and  $\kappa$  denote the curvature radius and curvature at distance  $s$  from the organ apex, respectively.  $\alpha(s)$  is the curvature angle at position  $s$ , while  $\alpha_{Tip}$  denotes the tip's curvature angle. The tangent  $\vec{t}$  and normal  $\vec{n}$  are shown. The dashed circle segments on the upper and lower sides have the same arc length, and the hatched area depicts the gradient in volume increase produced by differential growth.

tions relies on a relatively small amount of markers and interpolation schemes need to be applied (Peters and Bernstein, 1997). Moreover, the determination of curvature production through differential *REGR* profiles is critical, because the coordinates of the profiles have to be matched correctly (non-trivial for e.g. curved root geometry and easily resulting in artifacts).

As will be shown below,  $\kappa$  and  $d_t\kappa$  are not suited to describe the change of orientation of an organ and do not quantify sufficiently the production of curvature. This becomes clear in Fig. 4.1, where  $\kappa$  is constant and  $d_t\kappa$  is zero, although the orientation of the organ changes. Quantitative relations of curvature production at specific regions need to be established to elucidate differential growth and organ curvature in gravitropism, phototropism and hydrotropism (see e.g. Blancaflor and Masson 2003; Eapen et al. 2005; Esmon et al. 2005). Therefore, the concept of the curvature angle distribution (Mullen et al. 1998b; Mullen et al. 2000; Wolverton et al. 2002a; Wolverton et al. 2002b) was extended here, to find a suitable measure of curvature production (*differential growth curvature rate, DGCR*).

Theoretical calculations presented below, show for curvature occurring in a plane the relation of the *DGCR* to  $d_t\kappa$  and to differential *REGR* profiles. Moreover, this concept is extended to describe curvature and torsion processes in three dimensions. In addition to this, the *DGCR* is applied in a simple model of root gravitropism, and used to simulate two different cases of curvature production in root gravitropism (one and two sites of production). The recent proposal of the existence of two motors in root gravitropism is tested therewith (compare Wolverton et al. 2002a). The simulations presented here show that a suitable measure of curvature production is essential to be able to separate two motors that are located so closely as proposed (in the distal elongation zone, DEZ, and in the central elongation zone, CEZ; Ishikawa and Evans 1993; Wolverton et al. 2002a), and confirm the need of a suitable measure of curvature production (*DGCR*).

## 4.2 Curvature production in $\mathbb{R}^2$

In some situations, the center curve of curving organs can be approximated by a plane curve  $\varphi \mapsto \mathbb{R}^2$  (compare for example roots during the gravitropic reaction). In this section we assume curvature in a plane, while in the following section the case in  $\mathbb{R}^3$  will be treated. The natural coordinate system of a curve  $\varphi(s(t), t) \in \mathcal{C}^2(\mathbb{R} \times \mathbb{R}, \mathbb{R}^3)$  either in  $\mathbb{R}^2$  or  $\mathbb{R}^3$ , where  $s$  is the arc length, is given by (e.g. Smirnow 1990)

$$\begin{aligned} \mathbf{t} &= \partial_s \varphi \\ \mathbf{n} &= \frac{\partial_s \mathbf{t}}{\kappa} = \frac{\partial_{ss}^2 \varphi}{\kappa} \\ \mathbf{b} &= \mathbf{t} \times \mathbf{n}, \end{aligned}$$

where  $\mathbf{t}$  is the tangent<sup>1</sup>,  $\mathbf{n}$  is the normal and  $\mathbf{b}$  is the binormal of  $\varphi$ , and  $\kappa = \|\partial_s \mathbf{t}\|$  is the curvature and  $\times$  denotes the vector product. Compare also Fig. 4.1. The curvature vector  $\mathbf{N}$  is defined as

$$\mathbf{N} = \partial_s \mathbf{t} = \kappa \mathbf{n} ,$$

and gives a measure of the intensity and direction of curvature. Here, the midline  $\varphi$  of the organ depends on time  $t$  because it deforms due to the curvature process as a consequence of asymmetrical growth. The rate of change of the curvature vector can be used to determine the rate of change of  $\kappa$ . The rate of change of  $\mathbf{N}$  is given by

$$d_t \mathbf{N} = d_t \partial_s \mathbf{t} = \partial_s \partial_t \mathbf{t} + \partial_s^2 \mathbf{t} d_t s = \partial_s (\partial_t \mathbf{t} + \partial_s \mathbf{t} v) - \partial_s \mathbf{t} REGR ,$$

where velocity,  $v = d_t s$ , and relative elemental growth rate  $REGR = \partial_s v$ , and the chain-law of differentiation were used. However, because  $\mathbf{t} = \mathbf{t}(s(t), t)$

$$d_t \mathbf{t} = \partial_t \mathbf{t} + \partial_s \mathbf{t} v ,$$

so that

$$d_t \mathbf{N} = \partial_s d_t \mathbf{t} - \partial_s \mathbf{t} REGR .$$

Now taking into account that the tangential and normal vectors are rotated by an angular velocity  $\boldsymbol{\Omega} = \omega \mathbf{b}$ , we find

$$\begin{aligned} d_t \mathbf{t} &= \boldsymbol{\Omega} \times \mathbf{t} = \omega \mathbf{b} \times \mathbf{t} = \omega \mathbf{n} , \\ d_t \mathbf{n} &= \boldsymbol{\Omega} \times \mathbf{n} = \omega \mathbf{b} \times \mathbf{n} = -\omega \mathbf{t} \end{aligned} \quad (4.1)$$

and

$$\begin{aligned} d_t d_t \mathbf{N} &= \partial_s (\omega \mathbf{n}) - \partial_s \mathbf{t} REGR \\ &= (\partial_s \omega) \mathbf{n} + \omega \partial_s \mathbf{n} - \kappa REGR \mathbf{n} \\ &= (DGCR - \kappa REGR) \mathbf{n} - \kappa \omega \mathbf{t} , \end{aligned}$$

were  $DGCR = \partial_s \omega$  is denoted *differential growth curvature rate*,  $\partial_s \mathbf{t} = \kappa \mathbf{n}$ ,  $\partial_s \mathbf{n} = -\kappa \mathbf{t}$  (Smirnow, 1990) and the chain-law of differentiation were used. Now using  $d_t \mathbf{N} = d_t \kappa \mathbf{n} + \kappa d_t \mathbf{n}$  we finally obtain

$$d_t \kappa = DGCR - \kappa REGR . \quad (4.2)$$

This shows that the rate of change of curvature  $d_t \kappa$  is composed of a “production” term  $DGCR$  and the term  $-\kappa REGR$ . The latter can be denoted as dilution term,

<sup>1</sup>No confusion should arise between the tangent  $\mathbf{t}$  and time  $t$ , as one is boldface and the other italic.

because it is negative for growing organs (as  $\kappa > 0$  and  $REGR > 0$ ).

The meaning of the  $DGCR$  becomes clear through a curvature conservation equation, which is obtained using

$$d_t \kappa = \partial_t \kappa + \partial_s \kappa v = \partial_t \kappa + \partial_s (\kappa v) - \kappa REGR ,$$

so that comparison delivers

$$\partial_t \kappa + \partial_s (\kappa v) = DGCR . \quad (4.3)$$

Coupling this equation to a conservation equation (compare e.g. the mass conservation equation  $\partial_t \rho + \text{div}(\rho \mathbf{v}) = 0$ ) shows that in the context of a curvature conservation equation  $DGCR$  is the *source of curvature*. This shows that  $DGCR$  is exactly the concept sought for to characterize production of curvature. Moreover its calculation is simple through the angular velocity  $\omega$  (tropic speed)

$$DGCR := \partial_s \omega . \quad (4.4)$$

It is defined according to the  $REGR$ , as a divergence of a “velocity”. However, instead of representing the relative increase in length, it describes the amount of curvature angle produced per unit time and unit length. Therefore, the curvature angle can be obtained by an integration

$$\alpha(s(t), t) = \int_0^T \int_0^{s(t)} DGCR \, ds(t) \, dt . \quad (4.5)$$

Note that because the arc length  $s(t)$  changes in time, the integration over distance and over time do not commute.

### 4.3 Differential growth in $\mathbb{R}^2$

The term differential growth has to be defined carefully, because it can be interpreted widely and lead to misunderstandings. A measure of growth could be the rate of change of length, of area or of volume or the relative growth rate ( $REGR$ ,  $RGR$ ).  $REGR$  gradients may be interpreted as differential growth (Zieschang et al. 1997; Mullen et al. 1998a). However, although a  $REGR$  gradient may not exist, the organ can be changing its orientation due to a gradient in rate of change of length.<sup>2</sup> This makes clear, that orientation is determined by gradients

<sup>2</sup> $REGR$  measures the relative increase in length. For same  $REGR$ , a long length element increases absolutely more than a short element, leading to a change of orientation.

in rate of change of length and not by gradients in *REGR*. Differential growth will thus be defined here, in the context of tropisms, as the process behind changes in orientation.

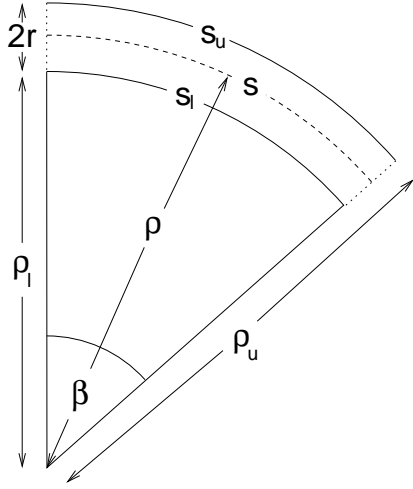


**Figure 4.2:** Simplified geometry of a curved cylindrical organ.  $\rho$  is the curvature radius of the midline, while  $\rho_u$  and  $\rho_l$  are the curvature radius' of the upper and lower sides.  $\beta$  is the opening angle of the arc segments  $s$ ,  $s_u$  and  $s_l$  (midline, upper and lower side respectively), and  $r$  is the radius of the organ.

The connection of the *DGCR* to *REGR* gradients is found by assumption of a cylindrical organ of radius  $r$  (Fig. 4.2; compare Silk and Erickson 1978; Silk 1989; Zieschang et al. 1997). At a certain arc length, the midline and the upper and lower sides can be approximated by segments of a circle. The curvature radius  $\rho$  of the midline curve can be determined through

$$s = \beta \rho \quad \Rightarrow \quad \rho = \partial_\beta s ,$$

where  $s$  is the arc length and  $\beta$  is the opening angle of the segment. The difference in curvature radius between the upper and lower sides is

$$\rho_u - \rho_l = \partial_\beta s_u - \partial_\beta s_l = 2r . \quad (4.6)$$

The organ is assumed to have a constant radius  $r$ , so that the time derivative of Eq. (4.6) is

$$d_t(\partial_\beta s_u - \partial_\beta s_l) = 0 .$$

The partial derivative  $\partial_\beta$  and total derivative  $d_t$  do not commute because  $\beta = \beta(t)$ , so that using the chain-law of differentiation and  $s_{u,l} = s_{u,l}(\beta(t), t)$  the above Equation is transformed into

$$\partial_\beta (\partial_t s_u + \partial_\beta s_u d_t \beta - \partial_t s_l - \partial_\beta s_l d_t \beta) - (\partial_\beta s_u - \partial_\beta s_l) \partial_\beta d_t \beta = 0 .$$

However,  $d_t \beta = \omega$  is the angular velocity by which the tangent  $\mathbf{t}$  is rotated, so that

$$\partial_\beta d_t \beta = \partial_s d_t \beta \partial_\beta s = \rho \partial_s \omega = \rho DGCR ,$$

where  $DGCR = \partial_s \omega$  and  $\rho = \partial_\beta s$  were used. Taking now into account Eq. (4.6) and that  $d_t s_{u,l} = \partial_t s_{u,l} + \partial_\beta s_{u,l} d_t \beta$  we find

$$DGCR = \frac{\partial_s(v_u - v_l)}{2r}, \quad (4.7)$$

where  $v_u = d_t s_u$  and  $v_l = d_t s_l$  are the rate of change of arc length of the upper and lower sides, respectively. Eq. (4.7) can be transformed into an expression of a *REGR* gradient

$$DGCR = \frac{REGR_u - REGR_l}{2r} + \kappa \frac{REGR_u + REGR_l}{2}. \quad (4.8)$$

where  $REGR_u = \partial_{s_u} v_u$  and  $REGR_l = \partial_{s_l} v_l$  are the *REGR* of the upper and lower sides respectively. The second term on the right of Eq. (4.8) arises from the change of variables  $s \mapsto s_{u,l}$ . Note that in general

$$REGR \neq (REGR_u + REGR_l)/2.$$

Silk and Erickson 1978 derived a similar expression to Eq. (4.8)

$$d_t \ln(1 + 2r\kappa') = REGR_u - REGR_l, \quad (4.9)$$

where  $\kappa'$  is the curvature of the lower side. A simple but somewhat cumbersome calculation shows that Eq. (4.9) is consistent to Eqs. (4.2) and (4.8) up to second order terms of  $\kappa r$ .<sup>3</sup>

The determination of curvature production *DGCR* through (4.4) is superior to using (4.8), as it uses the midline of the organ and is of particular advantage in root tips, where cell lineages have a complicated geometry near the quiescent center and organ radius  $r$  cannot be assumed to be uniform along the axis (Hejnowicz and Hejnowicz, 1991).

## 4.4 Curvature in $\mathbb{R}^3$

In the past sections we treated curvature production of organs in a plane. Nonetheless, curvature processes occur in the three dimensional space. This opens new motion possibilities, in particular *torsion* of the organ. Circumnutations of roots and hypocotyls is known to include torsion of the organ (e.g. Silk 1989; Barlow 1992). A description in plane is thus only a rough approximation. However, the

<sup>3</sup>Silk and Erickson 1978 used another nomenclature:  $M(o) = REGR_u$ ,  $M(i) = REGR_l$  and in particular  $R = \rho - r$ . This results in a slightly different curvature than the used here:  $\kappa' = R^{-1} \neq \rho^{-1} = \kappa$ .

plane case can be subsequently extended to describe curvature in  $\mathbb{R}^3$ .

The calculations presented in Section 4.2 are based on Eq. (4.1). In  $\mathbb{R}^3$  the rotation axis of  $\mathbf{t}$  and  $\mathbf{n}$  is not anymore  $\mathbf{b}$ . Instead the angular velocity  $\mathbf{\Omega}$  is a linear combination of the three vectors

$$\mathbf{\Omega} = \omega_t \mathbf{t} + \omega_n \mathbf{n} + \omega_b \mathbf{b} , \quad (4.10)$$

where  $\omega_t = \mathbf{\Omega} \cdot \mathbf{t}$ ,  $\omega_n = \mathbf{\Omega} \cdot \mathbf{n}$  and  $\omega_b = \mathbf{\Omega} \cdot \mathbf{b}$ . Eq. (4.10) shows that  $\mathbf{\Omega}$  acts also on the binormal  $\mathbf{b}$  (torsion). The time dependence of the natural coordinate system is determined by the ODE

$$\begin{aligned} d_t \mathbf{t} &= \mathbf{\Omega} \times \mathbf{t} = \omega_b \mathbf{n} - \omega_n \mathbf{b} \\ d_t \mathbf{n} &= \mathbf{\Omega} \times \mathbf{n} = \omega_t \mathbf{b} - \omega_b \mathbf{t} \quad \text{for } 0 < t \\ d_t \mathbf{b} &= \mathbf{\Omega} \times \mathbf{b} = \omega_n \mathbf{t} - \omega_t \mathbf{n} \\ \mathbf{t}(0) &= \mathbf{t}_0 , \mathbf{n}(0) = \mathbf{n}_0 , \mathbf{b}(0) = \mathbf{b}_0 \quad \text{for } t = 0 \end{aligned} \quad (4.11)$$

Through a calculation analogous to Section 4.2, but taking Eq. (4.11) and  $\partial_s \mathbf{n} = -\kappa \mathbf{t} - \tau \mathbf{b}$  (Smirnow 1990) into account, we find

$$\begin{aligned} d_t \kappa &= -\omega_n \tau + \partial_s \omega_b - \kappa \text{REGR} , \\ d_t \tau &= \omega_n \kappa - \partial_s \omega_t - \tau \text{REGR} , \end{aligned} \quad (4.12)$$

where  $\omega_n = \omega a_n$  and  $\omega_t = \omega a_t$ . Eq. (4.12) is a coupled ODE system, which solution gives  $\kappa$  and  $\tau$  at any time. Eq. (4.12) can be transformed into conservative form, yielding

$$\begin{aligned} \partial_t \kappa + \partial_s (\kappa v) &= -\omega_n \tau + \partial_s \omega_b , \\ \partial_t \tau + \partial_s (\tau v) &= \omega_n \kappa - \partial_s \omega_t . \end{aligned} \quad (4.13)$$

This shows that the sources of curvature and torsion are given by

$$\begin{aligned} DGCR &:= -\omega_n \tau + \partial_s \omega_b , \\ DGTR &:= \omega_n \kappa - \partial_s \omega_t , \end{aligned} \quad (4.14)$$

where *DGTR* is the *differential growth torsion rate*. Note that the *DGCR* in Eq. (4.14) is consistent with Eq. (4.4), because  $\tau = 0$  for organs that curve in a plane.

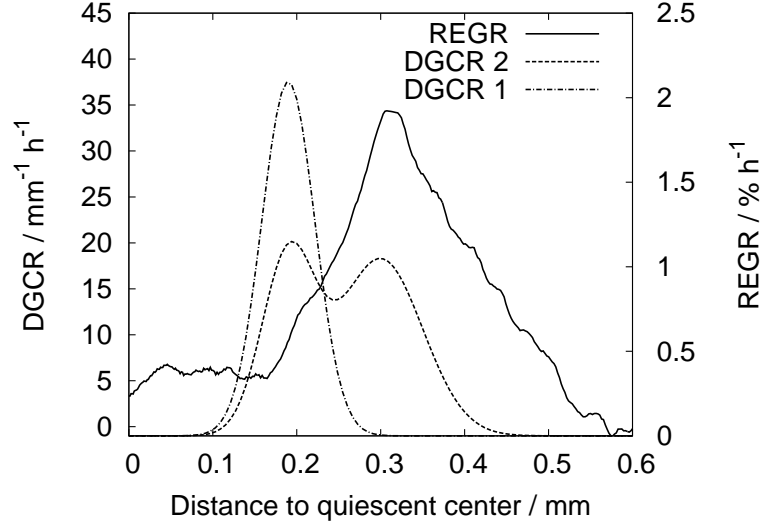


**Figure 4.3:** Root growth and model of gravitropism motors. Solid line denotes a *measured* relative elemental growth rate (*REGR*) distribution of an *A. thaliana* root (average over first 3 h of gravitropic reaction; provided by K. A. Nagel, Forschungszentrum Jülich). Dashed and dashed dotted lines denote the differential growth curvature rate (*DGCR*) assumed for two and one gravitropism motor(s), respectively.

### Root gravitropism model

The proposed measure *DGCR* is applied here in a simple model of the gravitropic reaction of roots. Eq. (4.3) can be used to simulate two cases of curvature production: one and two sites of production. These cases are conceivable in root gravitropism, as the existence of two motors have been proposed recently (Wolverton et al. 2002a). These motors have been assumed to be located at the distal and central elongation zones (DEZ and CEZ; Ishikawa and Evans 1993), which are centered around the elongation maximum (CEZ) and apically of the elongation maximum where growth attains 30% of the maximal *REGR* (DEZ; compare Fig. 4.3).

Let a gravitropism motor be given by a bell-shaped curve

$$M(s, \beta) = A \sin(\beta) \exp\left(-\frac{s - s_0}{\sigma^2}\right), \quad (4.15)$$

where  $s$  is the arc-length,  $\beta$  is the stimulation angle,  $A$  is an amplitude,  $s_0$  is the center position of the motor and  $\sigma^2$  describes the extension of the motor. The factor  $\sin(\beta)$  models the dependence on the stimulation angle  $\beta$  and was chosen in terms of the Sine-Law (Sachs 1882).

**Table 4.1:** Simulation parameters of root gravitropism model.

Motor	$A$ ( $mm^{-1} h^{-1}$ )	$s_0$ ( $mm$ )	$\sigma^2$ ( $mm^2$ )
One motor			
One	2.1	0.19	$2 \times 10^{-3}$
Two motors			
One	1.05	0.19	$2 \times 10^{-3}$
Two	1.05	0.3	$5 \times 10^{-3}$

Because the  $DGCR$  is the source of curvature [compare Eq. (4.3)], and sources are additive, it can be described as a sum over the motors

$$DGCR(s, \beta) = \sum_{i=0}^N M_i(s, \beta) = \sum_{i=0}^N A_i \sin(\beta) \exp\left(-\frac{s - s_{0,i}}{\sigma_i^2}\right), \quad (4.16)$$

where  $N$  is the number of motors present. An extension of this expression to describe more than one sensor, i.e. more than one stimulation angle  $\beta$ , should be straightforward. When the root is initially stimulated by  $90^\circ$ , the stimulation angle and curvature angle of the whole organ are related by  $\beta = 90^\circ - \alpha_{Tip}$ .

Note that the model of the dependence of the motors on the stimulation angle is very simplistic. Signal transduction is not instantaneous in organs, so that information on the stimulation angle needs time to reach the sensitive tissue (refer to Swarup et al. 2005 for the case of auxin). Moreover, it is still unclear if the Sine-Law is correct (e.g. Audus 1964; Barlow et al. 1993; Mullen et al. 2000). However, as will become clear below, the fact that the reaction decreases in time is here more important than the actual law behind it.

Using Eqs. (4.3) and (4.16) two root gravitropism cases were simulated. The first assumes that one motor is responsible for curvature production, the second case assumes two spatially separated motors (Wolverton et al. 2002a). The parameters used in the simulation are presented in Table 4.1. These were chosen to resemble an *Arabidopsis thaliana* (L.) Heynh. root, and were based on the definition of the DEZ and CEZ and on unpublished measurements of the gravitropism kinetics of *A. thaliana* roots (measurements conducted in the author's lab). The velocity distribution  $v$  was obtained by integration of a measured  $REGR$  distribution (average over first 3 h of gravitropic reaction of an *A. thaliana* root; dataset provided by K. A. Nagel, Forschungszentrum Jülich). The  $REGR$  distribution and the gravitropism motors are shown in Fig. 4.3. As Eq. (4.3) is a conserva-

tion equation, it was solved using the *Conservative Lax Method*, which has been shown to be stable for suitable discretization widths (e.g. Potter 1973). These widths were chosen here to meet this stability condition (time:  $10^{-3} h$ , space:  $3 \mu m$ , fastest propagation velocity:  $< 80 \mu m h^{-1}$ ).

Fig. 4.4 A,B presents the simulation results under the assumption of one motor, while Fig. 4.4 C,D shows the results for two motors. Both cases showed a similar distribution of  $\kappa$ , composed initially of one peak located at the site of production, which reduced intensity in time and gave rise to a second broader peak (Fig. 4.4 A,C). The second peak can be contributed to advection/convection of curvature (Silk and Erickson 1978; Silk 1989), as becomes clear from the movement of its maximum. The first peak is due to production and its distance to the quiescent center is thus constant. A change in the intensity of the first motor is essential for the existence of the second peak. If no change in intensity would occur, growth dilution [compare Eq. (4.2)] would ensure that beyond the curvature motors the distribution of  $\kappa$  would fall monotonically without having a second maximum. Measurements of *Lepidium* and *Phleum* roots confirm the existence of a moving and a fixed peak (Selker and Sievers 1987; Zieschang and Sievers 1991). Wolverton et al. 2002a interpreted those two peaks as the two motors of gravitropism. However, the simulations presented here show that both cases, of one and two motors, exhibit this behavior. Thus,  $\kappa$  is insufficient to show the existence of two motors that are located so closely.

The rate of change of curvature  $d_t\kappa$ , which could erroneously be interpreted as a measure of curvature production [compare Eqs. (4.2) and (4.3)], fails also to show a clear separation of both motors (Fig. 4.4 C,D). If the distribution of  $\kappa$  is determined with a low resolution, which has been the case due to technical reasons (e.g. Selker and Sievers 1987; Zieschang and Sievers 1991), the existence of one or two motors cannot be definitively determined using  $d_t\kappa$  (Figs. 4.4 B,D). Both cases show due to growth dilution a similar  $d_t\kappa$  pattern. For the case of two motors, the second motor appears strongly reduced, so that the pattern may be interpreted as a slightly wider motor (Figs. 4.4 D). Curvature production may in general be underestimated around the elongation maximum, if  $d_t\kappa$  is assumed to be a measure of production.

In contrast to  $\kappa$  and  $d_t\kappa$ , the *DGCR* shows clearly either one or two motors (Figs. 4.4 B,D). The theoretical results found above are confirmed here; the *DGCR* measures the production of curvature and emphasizes the two motors independently of growth dilution. A hint for the specific function of the two motors is also found here. The model shows that the first motor, located where growth dilution is small, has a key role in curvature initiation, while the second, located where growth dilution is maximal, is crucial in maintaining curvature (Fig. 4.4 D). Note that the model presented here is not able to differ between one motor

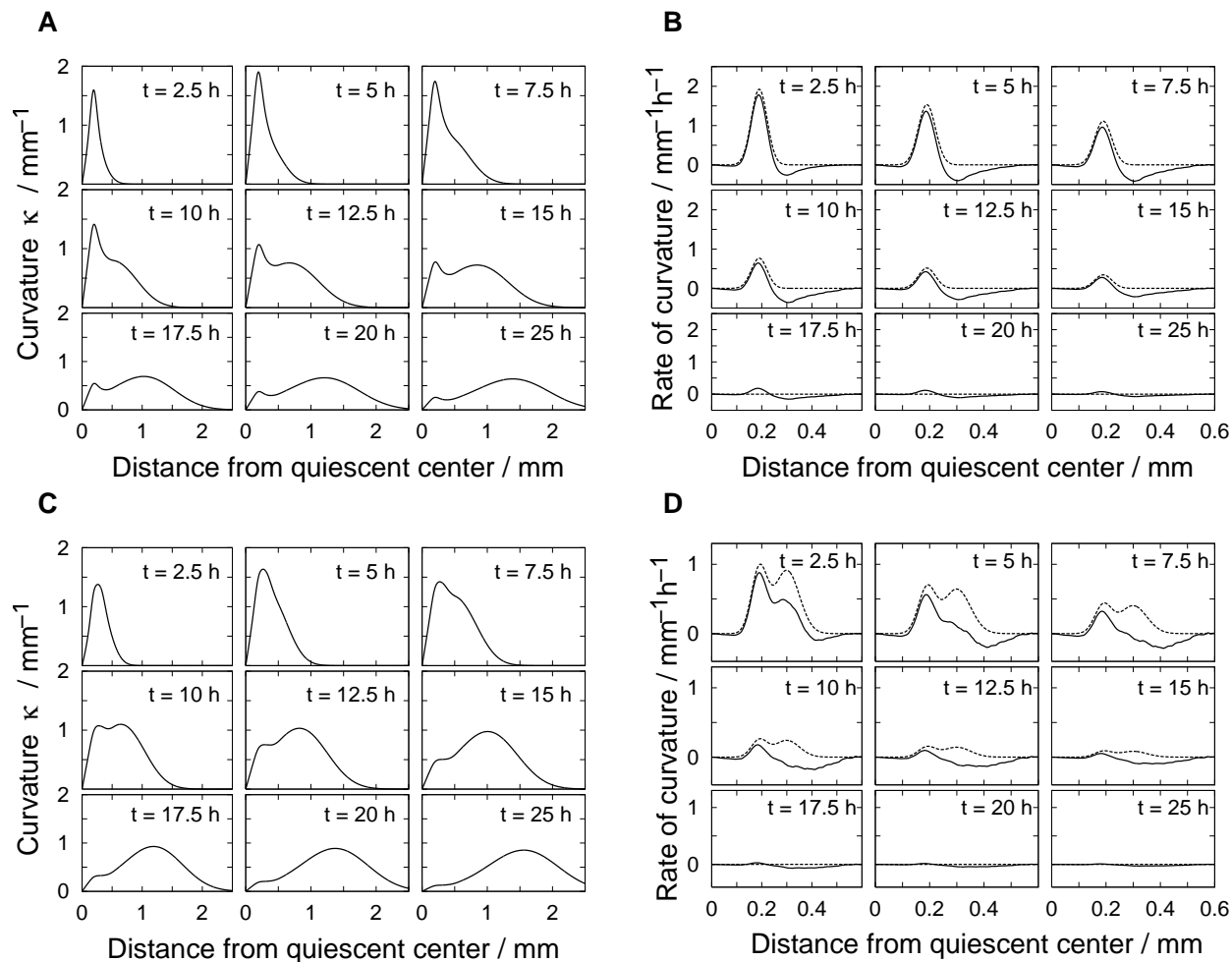


**Figure 4.4:** Simulated curvature and rate of curvature along a root axis. A, distribution of curvature  $\kappa$  along a root axis, under the assumption of one gravitropism motor located at the *distal elongation zone* (DEZ). B, distribution of rate of change of curvature  $d_t\kappa$  (solid line) and *differential growth curvature rate*  $DGCR$  (dashed line). One motor located at the DEZ is assumed to be responsible for curvature. C, distribution of  $\kappa$ , under the assumption of two gravitropism motors located at the DEZ and at the *central elongation zone* (CEZ). D, distribution of  $d_t\kappa$  and  $DGCR$ . Two motors located at the DEZ and CEZ are assumed to produce curvature.

with a large spatial extension and two spatially separated motors. This question can only be answered experimentally, through investigation if these cell groups are either controlled by two different sensors (Wolverton et al. 2002a; Wolverton et al. 2002b), or regulated through different phytohormones (Aloni et al. 2004). Nonetheless, the model shows that a better measure of curvature production (*DGCR*) is essential to elucidate this.

The *DGCR* was defined as the slope of the tropic speed distribution  $\omega(s) = d_t \alpha(s)$  [Eq. (4.4)], and is thus analogous to the *REGR*, defined as the slope of the velocity distribution  $v(s)$ . Such an analogy between translational and rotational movement is well known in physics (e.g. Halliday and Resnick 1988). The *DGCR* can be interpreted as follows. A rigid body can only move by means of a translation and/or a rotation. Because it is rigid, any volume element of it rotates with the same angular velocity. In non-rigid bodies, such as graviresponding roots and hypocotyls, the angular velocity changes in space, reflecting deformation. In cylindrical organs, the tropic speed  $\omega$  is an angular velocity and variations of it in space reflect curvature, which production is quantified by the *DGCR*. The *DGCR* represents the amount of curvature angle produced per unit length and unit time.<sup>4</sup> Curvature angle kinetics of root segments have been used intuitively before to characterize the gravitropic reaction of roots (Mullen et al. 1998b; Mullen et al. 2000; Wolverton et al. 2002a; Wolverton et al. 2002b). However, these do not allow a quantitative determination of curvature production, although this is essential to understand the control and signal pathways behind differential growth. This gap is filled by the *differential growth curvature rate DGCR*, and should thus serve as a helpful tool for future measurements.

---

<sup>4</sup>The *DGCR* can be expressed either in radians or in degrees per unit length and unit time. Radians should be used, when a comparison to  $d_t \kappa$  is sought for.

# Chapter 5

## Root Gravitropism

In Chapter 3 we presented a one-dimensional model of root growth. Abundant biological data was available to synthesize this model (Erickson and Sax 1956; Silk et al. 1989; Walter et al. 2002). Roots however vary substantially from a one-dimensional structure, they tend to curve, to circumnutate, to follow gradients of nutrients and humidity and, not to forget, to grow towards the direction of the gravity vector (e.g. Blancaflor and Masson 2003; Eapen et al. 2005; Walter and Schurr 2005). This encourages to expand the model presented in Chapter 3 into two or three dimensions. However, in contrary to the one-dimensional case, no extensive biological information is available, although this data is a prerequisite to model root growth. We therefore chose to investigate how root growth reacts to gravitropic stimulation. Aim was here to obtain data as accurate as possible and suitable for future modeling. This needed, however, a considerable extension of the growth analysis methods available (Walter et al. 2002).

This chapter is divided into three sections. The first is a biological introduction into root gravitropism (Section 5.1). The second describes the analysis of curvature (Section 5.2, based on Chapter 4). And finally, Section 5.3 is dedicated to the overall characterization of the gravitropic reaction, based on measurements of wild-type and PIN3 deficient mutants.<sup>1</sup>

### 5.1 Introduction

Root gravitropism has been a topic of research for a long time. Although the *sine rule*<sup>2</sup> was formulated more than 120 years ago (Sachs, 1882), the complete mechanism of root gravitropism is still unclear. In the last years the polar transport of the plant hormone auxin in roots has been extensively investigated (Muday 2001; Friml and Palme 2002; Friml et al. 2002; Blancaflor and Masson 2003;

---

<sup>1</sup>The PIN3 efflux facilitator protein is involved in relocation of auxin from the central root stele to the epidermal and cortical cell files, and is essential in the gravitropic signal transduction.

<sup>2</sup>Classical sine-law: the gravitropic stimulus is proportional to the sine of the inclination angle.

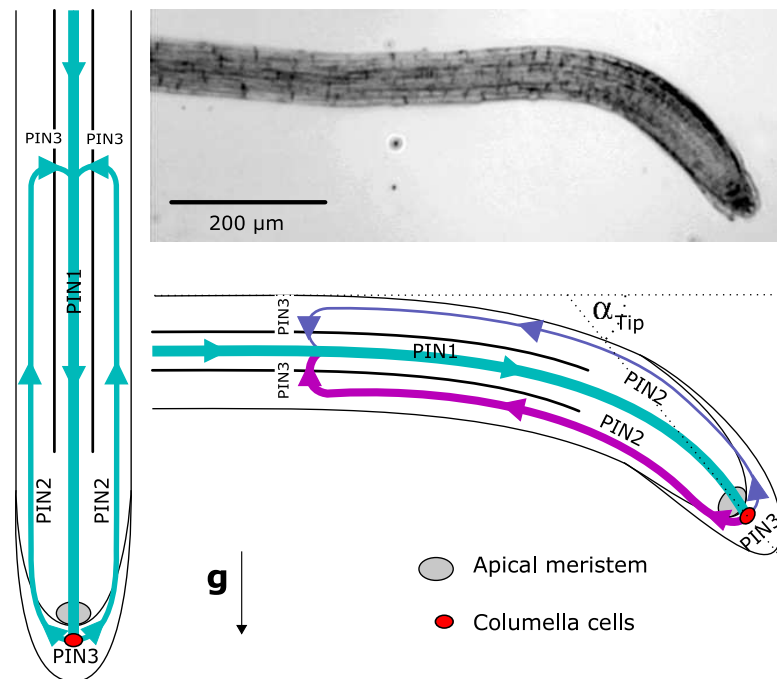


**Figure 5.1:** Simplified auxin transport model. During the gravitropic reaction, auxin is preferentially transported into the lower side of the root inhibiting growth and resulting in curvature. The curvature angle  $\alpha_{Tip}$  between the root tip and the horizontal is shown.

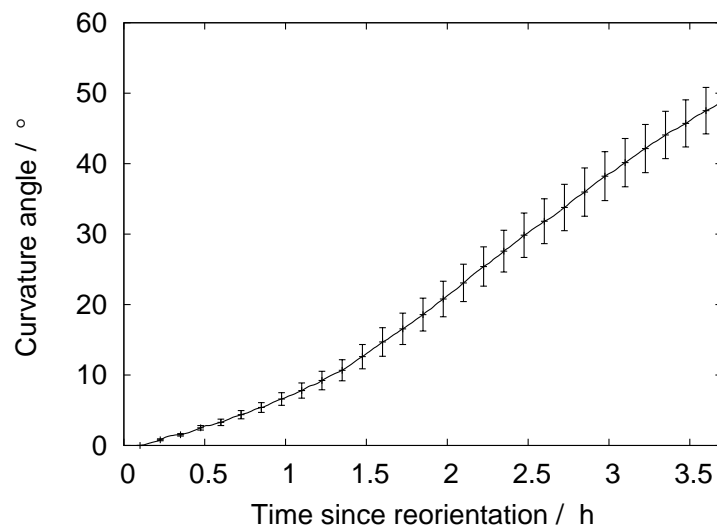


**Figure 5.2:** Curvature kinetics of *Arabidopsis thaliana* (L.) Heynh. roots. The curvature angle  $\alpha_{Tip}$  between the root tip and the horizontal is shown.

Blilou et al. 2005; Teale et al. 2005). The current transport model, denominated *fountain-model*, is based on influx (AUX/LAX) and efflux (PIN) facilitator proteins located on the plasma membrane (Muday 2001; Friml and Palme 2002); Perbal and Driss-Ecole 2003). It assumes that auxin is transported apically around the central cylinder by PIN1, apically near the columella by PIN4 leading to accumulation, radially from quiescent center towards the cortex by PIN3 and basipetally in the cortex towards the expansion zone by PIN2 (Fig. 5.1; Blancaflor and Masson 2003; Blilou et al. 2005; Teale et al. 2005).

One of the central statements of the fountain-model is that upon gravitropic stimulation PIN3 is asymmetrically reallocated in the columella cells. Auxin transport towards the cortex cells occurs then preferentially to the lower side of the root upon gravitropic stimulation (Fig. 5.1; Blancaflor and Masson 2003). Therefore, in the lower side more auxin is transported towards the expansion zone, leading to growth inhibition and to the actual bending (Blancaflor and Masson, 2003). Perception of gravity is believed to be accomplished in the columella cells by sedimentation of statoliths (Blancaflor and Masson 2003; Chen et al. 1999; Perbal and Driss-Ecole 2003).<sup>3</sup> However, hints of gravisensitivity outside the columella exist (Wolverton et al. 2002a; Wolverton et al. 2002b). The chain of events between perception and reallocation are still not known.

Friml et al. (2002) found that roots of *pin3* mutants, which lack the PIN3 protein,<sup>4</sup> react considerably slower to gravitropic stimuli than wild-type roots do. However, the question of why these mutants still react to reorientation has not been answered. Based on the fountain-model, no asymmetrical auxin redistribution is expected in *pin3* roots. Thus, either other auxin transport proteins are involved or roots use auxin independent pathways (Aloni et al., 2004). The existence of dual motors and sensors of gravitropism have been proposed recently (Wolverton et al., 2002a), and might explain why *pin3* mutants still react.

Measurements of gravitropic reaction have been conducted traditionally by determining the kinetics of the curvature angle (Fig. 5.2; Larsen 1957; Johnson 1965; Perbal et al. 2002; Wolverton et al. 2002a). Larsen (1957) proposed the empirical *logarithmic model* to describe the curvature kinetics. It states that the increment in response is proportional to the relative increment of the dose. The existence of a *presentation time*, minimal duration of stimulus to induce a response, is a consequence of this model. The presentation time has been used to characterize the sensitivity to gravitropic stimuli. Perbal et al. (2002) proposed

---

<sup>3</sup>Statoliths are specialized amyloplasts composed of dense materials (starch in roots, barium sulfate crystals in Chara rhizoids), and have a central role, as sedimentation bodies, in gravity perception.

<sup>4</sup>The convention used in molecular biology to designate mutants is to name them after the missing product. These are then written lowercase and italics, while the product itself is written roman and uppercase. For example, *pin3* is the mutant that lacks the protein PIN3.

the *hyperbolic model*, in which the response is limited by a ligand-receptor system, which fits the data more accurately. In contrast to the logarithmic model, the hyperbolic model does not involve a presentation time. Therefore, the slope of the curve at the origin was proposed as an index of gravitropic sensitivity. It is easily shown that neither the logarithmic nor the hyperbolic model are accurate as neither of take growth, the mediator of curvature, into account.<sup>5</sup>

Although the kinetics of curvature are an important tool for investigation of gravitropism, they are in their traditional form not suited to obtain information about the distribution of curvature production. However, determining the cell groups involved in gravitropic bending is essential to understand the gravitropic response. Attempts have been made to deduce curvature from the asymmetrical distribution of growth among opposite cell lineages along the root growth zone (Ishikawa et al. 1991; Mullen et al. 1998a; Zieschang et al. 1997). This method gave insight into the location of curvature production. The distal elongation zone (DEZ), a group of cells between the meristem and the zone of maximum elongation, is believed to be responsible for curvature initiation (Ishikawa et al. 1991; Ishikawa and Evans 1993; Ishikawa and Evans 1997; Mullen et al. 1998a). Along with the DEZ, the central elongation zone (CEZ), a zone located around the elongation maximum, has been reported to be involved in curvature production (Wolverton et al., 2002a). However, this method is intrinsically susceptible to errors, because it makes assumptions on the root geometry. Roots differ considerably from a cylindrical body, so that the question arises how positions on different cell lineages are matched.

## 5.2 Advances in curvature analysis

Although the measurements of gravitropic reaction evolved substantially in time, from hand measurement of curvature angle to automated digitizer systems (Sachs 1882; Mullen et al. 1998b), all suffered from a low spatio-temporal resolution of growth and curvature analysis. This problem can be dealt with by applying and adapting novel high resolution growth measurement methods (Schmundt et al. 1998; Walter et al. 2002; van der Weele et al. 2003). These methods have been successfully used to characterize differential reactions of *REG*R distributions towards changes of external parameters (Walter et al. 2002; Walter et al. 2003), and suit, together with the results of Chapter 4, the problem of characterization of the gravitropic reaction.

---

<sup>5</sup>A consequence of Eqs. (4.5) and (4.8) in Chapter 4, is that an inflection point in the curvature kinetics has to be present (clearly present in Fig. 5.2). However, neither the logarithmic nor the hyperbolic model contain this behavior.

Using differential growth to determine the gravitropic reaction is not a new concept (Selker and Sievers 1987; Zieschang et al. 1997; Mullen et al. 1998a). However, the traditional method to measure *REGR* distributions contains some pitfalls, because it relies on a relatively small amount of markers. The *REGR* distribution is acquired by applying interpolating schemes, which give rise to a large variation margin in the resulting distribution (Peters and Bernstein, 1997). The method used here for calculation of the *REGR* achieves a much higher spatial and temporal resolution (see e.g. Figs. 5.9 and 5.10 on pages 75 and 76). Moreover, the determination of curvature production through differential *REGR* profiles is prone to errors, because the coordinates of the upper and lower *REGR* profiles have to be matched correctly (non-trivial for curved root geometry, compare Fig. 5.4 on page 70). The method used here uses the coordinate system of the root mid-line and avoids this problem a priori.

A new concept of curvature production, the *differential curvature production rate* (*DGCR*; Chapter 4), has to be introduced to give consideration to the accuracy needed in determination of differential growth upon gravitropic stimulation. Until now the kinetics of curvature angle, e.g. Fig. 5.4 on page 70, have been the sole concept used to characterize the intensity of the reaction. These have been extended to obtain spatial information by tracking of the angle of segments (Mullen et al., 1998b). However, curvature angle is not sufficient to obtain reliable information on the location of curvature production. We therefore propose here the concept of the *DGCR* according to the relative elemental growth rate (*REGR*), which has been used successfully in root growth for decades (Erickson, 1976). This new concept of curvature production and the high spatio-temporal resolution of the applied method extend the set of essential tools needed in elucidation of the molecular mechanisms behind curvature initiation.

### 5.2.1 Calculation of spatio-temporal distributions

The spatio-temporal distributions of relative elemental growth rate (*REGR*) and the differential curvature production (*DGCR*), are determined using several steps: a) determination of velocity field, b) regularization of velocity field, c) tracking of a curve  $\varphi$ , d) calculation of *REGR* and *DGCR* profiles on the curve.

#### Velocity field

The velocity of each pixel  $(i, k)$  at frame  $m$ , is determined using the *structure tensor method* (Bigün and Granlund 1987; Haußecker and Spies 1998; Schmundt et al. 1998; Walter et al. 2002). The discretization of the structure tensor method is done via differentiation filters optimized for directional accuracy of the gradient

(Scharr, 2005). These filters are essential for the high precision of the estimated optical flow fields required for subsequent processing steps.

### Regularization

Under normal circumstances, this method does not deliver dense velocity fields, e.g. when an image region lacks sufficient grey value structure. Thus, to obtain a dense velocity field, a regularization, meaningful filling of missing information, has to be performed. The regularization was implemented as a *normalized convolution* (Jähne, 1997).

### Curve tracking

After obtaining the velocity of each pixel, the velocity field is interpolated to be able to track points between pixels. A linear interpolation was chosen, as the obtained velocity field is smooth and a higher interpolation order does not render additional accuracy. The position of any chosen point can be tracked in time by using an *Euler-Scheme* (Stoer and Burlisch, 2000a). This can be used to track any curve  $\varphi$ , e.g. the root mid-line, by discretization of  $\varphi$  into a set of  $N$  points  $\varphi_j$ . Each point  $\varphi_j$  is tracked in time, so that an approximation of the curve  $\varphi$  at each frame is obtained. The points  $\varphi_j$  and their positions in each frame are subsequently processed to obtain the spatio-temporal distributions of *REGR* and *DGCR*. For all measurements, the initial point  $\varphi_0$  of  $\varphi$  is chosen at the transition between quiescent center and apical meristem, i.e. the quiescent center and the calyptra are not tracked.

## 5.2.2 Relative elemental growth rate

To obtain the *REGR* spatio-temporal distribution, the distance  $l_j$  between points  $\varphi_j$  and  $\varphi_{j+1}$  is calculated for each frame (refer also to Chapters 2 and 3). The *REGR* of the length element  $l_j$  is

$$REGR_j = \frac{1}{l_j} d_t l_j = d_t \ln l_j, \quad (5.1)$$

and is used to obtain the spatio-temporal distribution of *REGR* (compare Fig. 5.9 on page 75). The *REGR* can also be defined as the derivative of the projection of the velocity field on  $\varphi$ :  $REGR = \partial_x v$ . Eq. (5.1) allows a simple but effective time averaging (Peters and Bernstein, 1997)

$$\overline{REGR}_j = \frac{1}{T} \int_0^T REGR_j(\tau) d\tau = \frac{1}{T} \int_0^T d_\tau \ln l_j d\tau = \frac{1}{T} \ln \left( \frac{l_j(T)}{l_j(0)} \right), \quad (5.2)$$

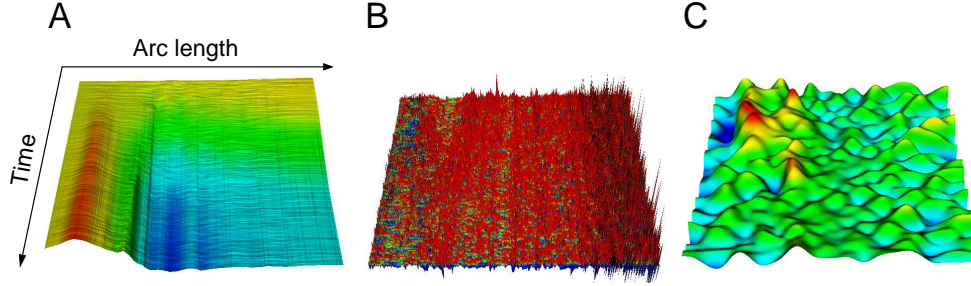


**Figure 5.3:** Denoise of spatio-temporal data. The x-axis represents arc length (distance to quiescent center) and the y-axis time since reorientation, color and height display intensity of scalar data. A and B, raw curvature angle and raw *DGCR* distributions. C, denoised *DGCR* distribution.

where  $T$  is the time over which averaging is done. Eq. (5.2) uses only the initial and final length. If a coordinate  $(x_j, y_j)$  is assigned to each length element  $l_j$ , Eqs. (5.1) and (5.2) provide raw and time averaged *REGR* profiles on  $\varphi$ . See Fig. 5.10 on page 76 for an example result of the averaging method (visualized using *VTK*, Visualization ToolKit, Kitware, Inc., New York, U.S.A.).

### 5.2.3 Differential growth curvature rate

An approximation of the curvature angle distribution along the root is easily obtained through the curve points  $\varphi_j$ . The derivative in time of the curvature angle gives the angular velocity, which is a measure of the rate of change of an angle. The angular velocity can be calculated for each segment  $\varphi_{j+1} - \varphi_j$

$$\omega_j = d_t \alpha_j, \quad (5.3)$$

where  $\alpha_j$  is the curvature angle of the segment and  $\omega_j$  the corresponding angular velocity. A rotating rigid body has an uniform angular velocity, while the angular velocity along a curving body varies in space. In analogy to the *REGR*, the differential curvature production *DGCR* is defined as the divergence of the angular velocity

$$DGCR_j = \partial_x \omega_j \approx \frac{\omega_{j+1} - \omega_{j-1}}{l_j + l_{j-1}}. \quad (5.4)$$

This gives the amount of curvature degrees produced per unit length and unit time.

### 5.2.4 Denoising of spatio-temporal distributions

*REGR* and *DGCR* are obtained through derivatives [Eqs. (5.1) and (5.4)]. Therefore a small disturbance in the velocity field expands to a large error in *REGR*

and *DGCR* (Fig. 5.3). Several methods to reduce noise are available (Black and Rangarajan, 1996). We chose to use a diffusive approach, based on the minimization of a functional composed of a data and a smoothness term [compare Black and Rangarajan 1996, Eq. (1)]

$$J(u) = \int (u - u_{orig})^2 dx + \lambda \int \|\nabla u\|^2 dx \rightarrow \min, \quad (5.5)$$

where  $u$  is the smooth solution and  $u_{orig}$  is the original data. Depending on  $\lambda$ , the solution is either smoother, or it is nearer to the original noisy data. The minimization process is achieved using an iterative scheme. Fig. 5.3 shows the effect of Eq. 5.5 on the *DGCR* of a selected root during the gravitropic reaction (reorientation by 90 °).

### 5.2.5 Normalization and averaging of distributions

Due to natural variations of root growth within one plant line, the distribution of *REGR* and *DGCR* have to be normalized to be able to produce meaningful average spatio-temporal distributions. Normalization is achieved by the transformation

$$\begin{aligned} REGR' &= \frac{REGR}{REGR_{max}}, \\ DGCR' &= \frac{DGCR}{DGCR_{max}}, \\ x' &= \frac{x-x_0}{\sigma}, \end{aligned} \quad (5.6)$$

where  $REGR'$  and  $x'$  are the transformed relative elemental growth rate and position,  $REGR_{max}$  is the maximal growth rate,  $DGCR_{max}$  is the maximal curvature production rate,  $x_0$  is the position of the growth maximum and  $\sigma$  is half the full width at half maximum. Eq. (5.6) transforms the *REGR* distribution such that the maximum, located at position zero, has a value of one and the distribution has a full width of one at half maximum. The normalized distributions of different roots can then be averaged without artificial flattening or loss of form. The average distribution can subsequently be de-normalized using the mean normalization coefficients. Eq. (5.6) is a spatial normalization, but we are also interested in the temporal evolution. If the normalization process would be applied at each frame, the temporal evolution of the spatial distribution would get lost. We chose thus to use a reference spatial distribution to normalize the spatial distributions in each frame. For each measurement, the reference frame is obtained by averaging of the *REGR* distribution during the response. After determination of the reference frame, the measurement is normalized and the average over all measurements is determined. The average spatio-temporal distributions (compare Fig. 5.9 on page 75) can be used to obtain either the kinetics through spatial integration (Figs. 5.5 and 5.6 on page 71) or the average spatial distributions through integration in time

(Figs. 5.7 and 5.8 on page 72).

## 5.3 Characterization of root gravitropism

In this section the results of Chapter 4 and the Methodological Advances described in Section 5.2 are applied to characterize the gravitropic reaction of wild-type and mutant roots. Based on the determination of optical flow of gray-value structures through image sequences, we mapped the gravitropic root curvature of individual roots by introduction of a novel curvature production quantification method. Averaging of the individual data sets allowed to determine the specific contribution of PIN3 to growth along the growth axis. We demonstrate that two spatially separated cell groups are responsible for curvature production upon stimulation, and identify these cell groups with the two motors of gravitropism proposed recently (Wolverton et al., 2002a). Additionally, we demonstrate that only one of the motors depends on PIN3, suggesting that the other motor is based on a different pathway (compare Aloni et al. 2004).

### 5.3.1 Kinetics of growth and curvature

Analysis of kinetic changes of curvature angle and inspection of the images of both wild-type and mutant roots showed that *pin3* roots curved substantially slower than wild-type (*wt*) roots (Fig. 5.4). While wild-type roots curved by  $50^\circ$  within the first 3.5 *h* of reaction, *pin3* mutants reached only  $27^\circ$ . The gravitropic reaction was accompanied by variation in root growth velocity, i.e. the velocity by which the root tip moves away from the non-growing basal region.

Reorientation of wild-type and *pin3* roots reduced growth velocity in both organs (Fig. 5.5). Growth velocity of wild-type roots declined significantly during the first hour reaching a minimum, but recovered during the following 3 *h* to almost the original velocity. *pin3* roots however recovered substantially slower over 4 *h* before the original growth was resumed (Fig. 5.5). This suggests that the growth rate of *pin3* was essentially modified.

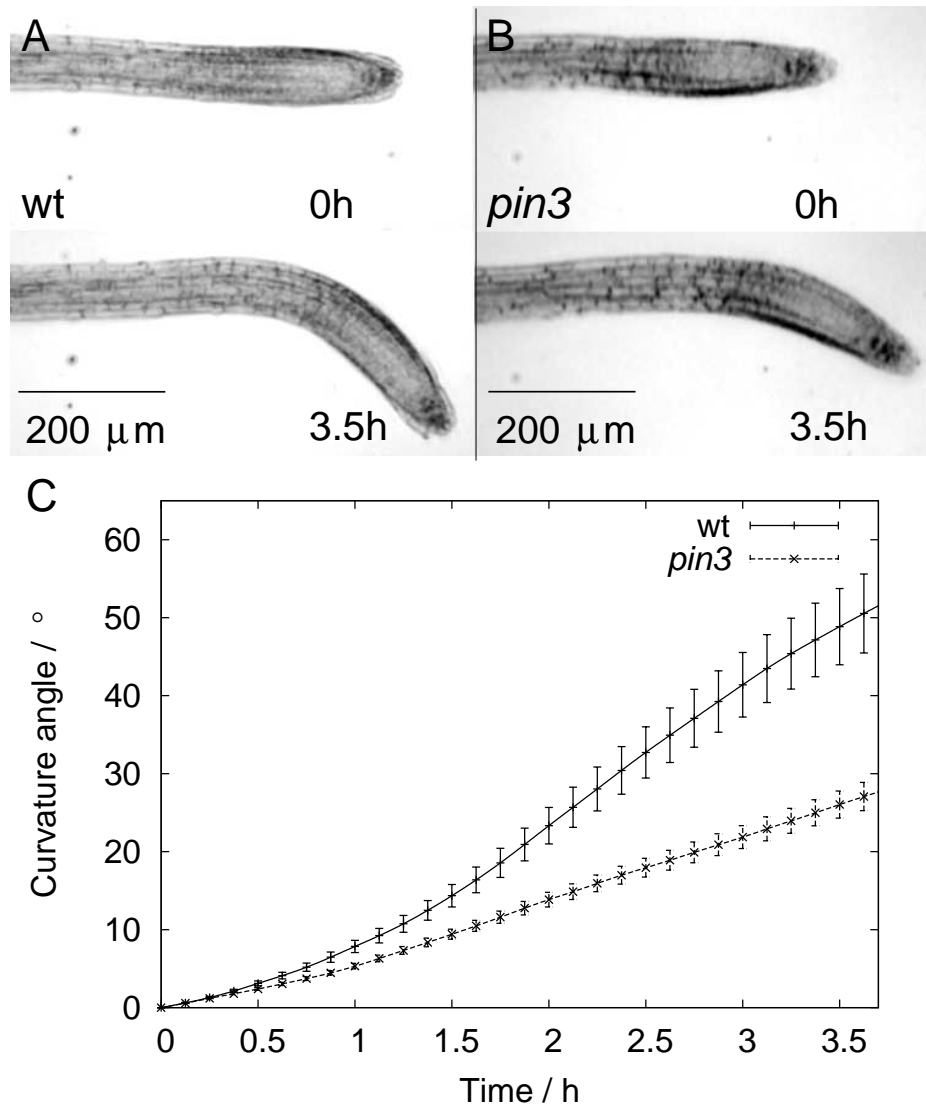


**Figure 5.4:** A and B, Selected wild-type and *pin3* roots before and 3.5 h after reorientation by 90°. C, Curvature angle kinetics of wild-type and *pin3* roots after reorientation by 90°. The standard errors for every 15-th data point are shown (wild-type:  $n = 6$ , *pin3*:  $n = 5$ ).

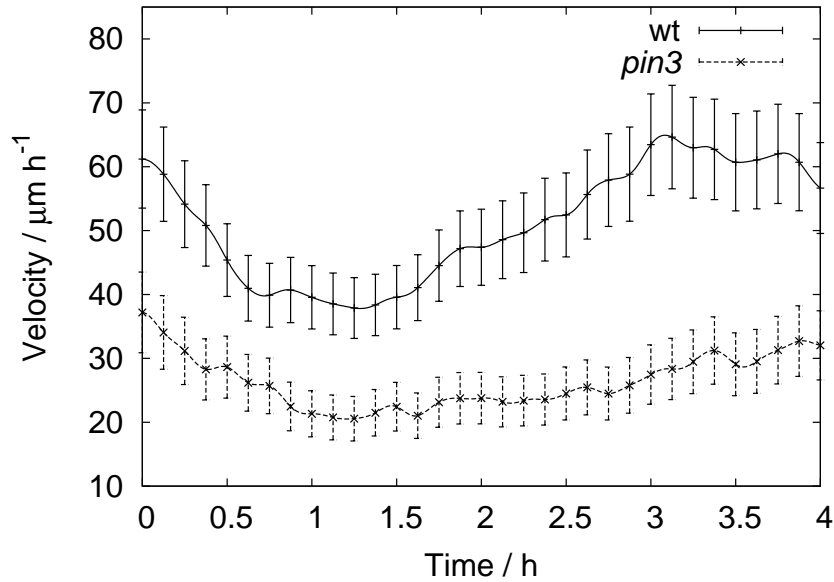


**Figure 5.5:** Root tip velocity kinetics of wild-type and *pin3* roots after reorientation by  $90^\circ$ . The standard errors for every 15-th data point are shown (wild-type:  $n = 6$ , *pin3*:  $n = 5$ ).

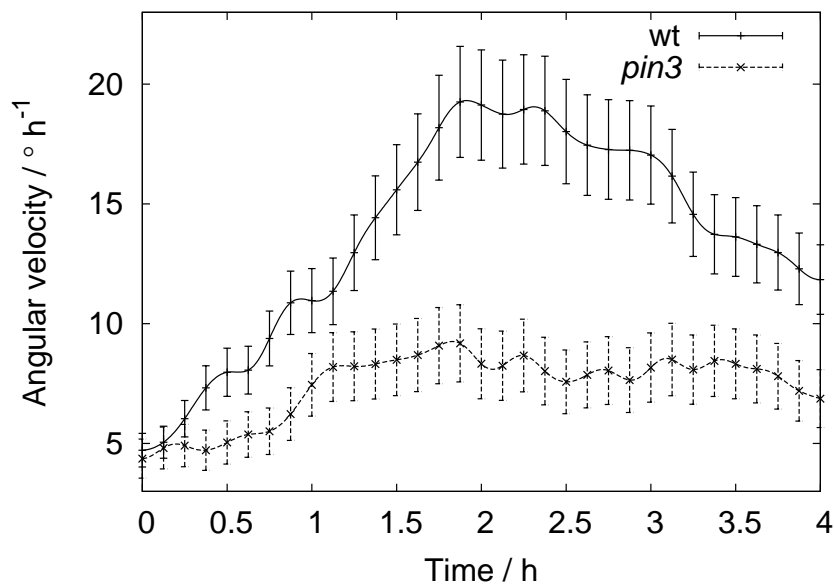


**Figure 5.6:** Evolution in time of the angular velocity of the root tip of wild-type and *pin3* roots during gravitropic response (rotated by  $90^\circ$ ). The standard errors for every 15-th data point are shown (wild-type:  $n = 6$ , *pin3*:  $n = 5$ ).

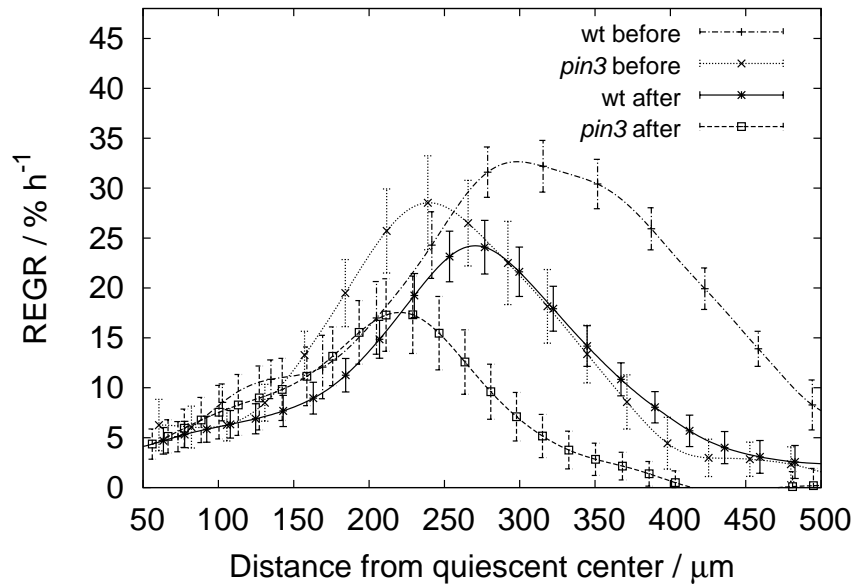


**Figure 5.7:** Average relative elemental growth rate (*REGR*) spatial distribution of wild-type and *pin3* roots during the first 4 h of gravitropic stimulation (rotated by 90°). The standard errors for every 15-th data point are shown (wild-type:  $n = 6$ , *pin3*:  $n = 5$ ).

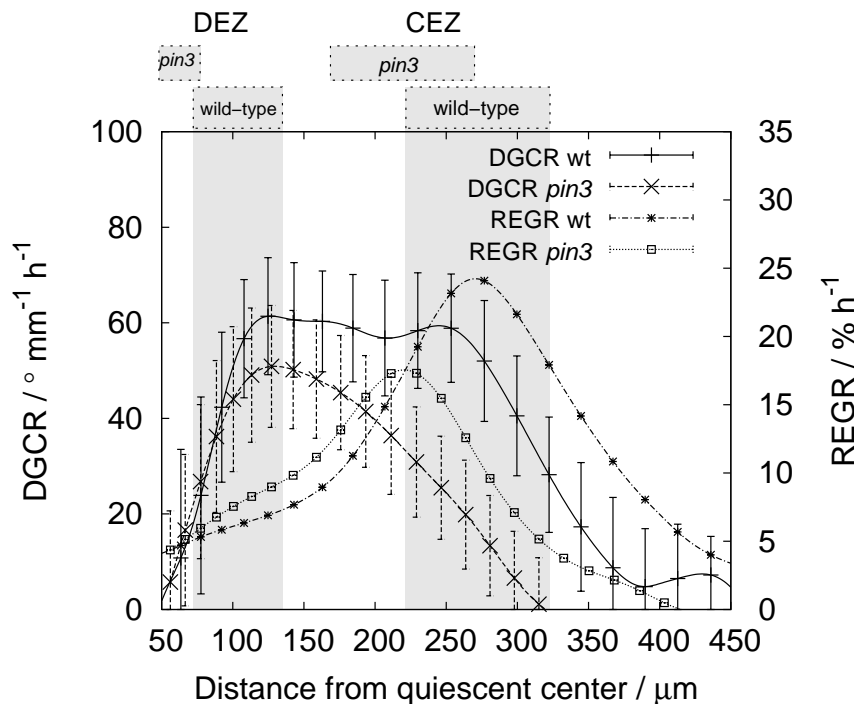


**Figure 5.8:** Differential growth curvature rate (*DGCR*) spatial distribution of wild-type and *pin3* roots rotated by 90° (average over the first 4 h of gravitropic stimulation). The central and distal elongation zones (CEZ and DEZ, respectively) are depicted for comparison. The standard errors for every 15-th data point are shown (wild-type:  $n = 6$ , *pin3*:  $n = 5$ ).

The angular velocity (i.e. the slope of the curvature angle kinetics, see Fig. 5.4) of the root tip gives information on the rate of curvature of the root. As shown in Fig. 5.6, analysis of the angular velocity reveals that the reaction of wild-type roots was composed of three phases, during which angular velocity increased distinctly in the first and second hour followed by a phase of decreasing angular velocity from 2 *h* onwards. A maximal angular velocity was reached approximately 2 *h* after reorientation (Fig. 5.6). The transition from the first into the second phase coincides with the minimum of root tip velocity (1 *h* after rotation; Fig. 5.5), suggesting a coordination between curvature and growth slowdown. *pin3* lacks the second increasing phase; a sustained phase of constant angular velocity was found instead (Fig. 5.6). Reduction of angular velocity occurred 3.5 *h* after rotation in *pin3* roots, whereas wild-type roots reduced their angular velocity already 2 *h* after rotation. As the initial curvature phases of wild-type and *pin3* roots are comparable, we conclude that the gravitropic curvature is mediated by two distinct responses, one being PIN3 dependent and another one PIN3 independent. This coincides with earlier hypotheses in which the existence of two motors of gravitropism had been proposed (Wolverton et al., 2002a).

The average spatial distributions of relative elemental growth rate [*REGR*, Eq. (5.1) in Section 5.2] in wild-type and *pin3* roots before and after reorientation of the roots by 90° are shown in Fig. 5.7 (average over 4 *h* of 11 gravitropic reactions). Bell-shaped *REGR* distributions with distinct *growth maxima* were found in both wild-type and *pin3* roots before and during gravitropic stimulation. Before reorientation, the growth distribution of the *pin3* roots was apically shifted to a narrow region close to the quiescent center with a reduced maximal growth intensity (*REGR<sub>max</sub>* *wt*: 33 % *h*<sup>-1</sup>; *pin3*: 28 % *h*<sup>-1</sup>), and a reduced growth zone length (75% of the wild-type). The growth maximum of *pin3* was also shifted towards the quiescent center (*wt* at 298  $\mu\text{m}$  and *pin3* at 239  $\mu\text{m}$ ). Similar differences between wild-type and *pin3* roots were found after reorientation (*wt*: 25 % *h*<sup>-1</sup> at 271  $\mu\text{m}$ ; *pin3*: 17 % *h*<sup>-1</sup> at 224  $\mu\text{m}$ ). Reorientation had similar effects on the *REGR* distribution of wild-type and *pin3*, composed of a significant reduction in *REGR<sub>max</sub>* and an apical shifting of the growth maximum (*wt* reduction: 75% of orig. growth and 91% of orig. position; *pin3*: 61% of growth and 94% of position).

The average spatial distribution of differential growth curvature rate (*DGCR*, Eq. (5.4) in Section 5.2) during the gravitropic response of wild-type and *pin3* roots is shown in Fig. 5.8 (average of 11 roots and over the first 4 *h* of response). Both roots increased their *DGCR* within the first 100  $\mu\text{m}$  behind the quiescent center. While wild-type roots maintained a more or less constant intensity of 60 ° *mm*<sup>-1</sup> *h*<sup>-1</sup> between 100  $\mu\text{m}$  and 250  $\mu\text{m}$  behind the quiescent center, *pin3* roots reached a maximum of 50 ° *mm*<sup>-1</sup> *h*<sup>-1</sup> at 120  $\mu\text{m}$  and decreased intensity towards the base of the growth zone. This suggests that the reaction phases are spatially separated (compare also Fig. 5.6). Comparison of curvature production

**Table 5.1:** Mean normalization coefficients of relative elemental growth rate ( $REGR$ ) and differential growth curvature rate ( $DGCR$ ) distributions of wild-type and  $pin3$  roots. Normalization:  $REGR' = REGR/REGR_{max}$ ,  $DGCR' = DGCR/DGCR_{max}$  and  $x' = (x - x_0)/\sigma$ , where  $REGR_{max}$  and  $DGCR_{max}$  are the maximal values of  $REGR$  and  $DGCR$ ,  $x_0$  is the position of the growth maximum and  $\sigma$  is the full width at half maximum of the expansion zone. The standard errors are shown (wild-type:  $n = 6$ ,  $pin3$ :  $n = 5$ ).

Plant	$x_0$ ( $\mu m$ )	$\sigma$ ( $\mu m$ )	$REGR_{max}$ (% $h^{-1}$ )	$DGCR_{max}$ ( $^{\circ} mm^{-1} h^{-1}$ )
wild-type	$271 \pm 8$	$169 \pm 17$	$25 \pm 2$	$63 \pm 4$
$pin3$	$224 \pm 17$	$129 \pm 9$	$17 \pm 3$	$51 \pm 8$

with the growth distributions shows that curvature occurred apically of the growth maximum in both roots. The location of curvature initiation did not depend on the position of the growth maxima. However, wild-type roots produced a substantial amount of curvature almost at the growth maximum, in contrast to  $pin3$  roots.

Fig. 5.9 presents a comparison of the spatio-temporal distribution of  $REGR$  and  $DGCR$  of wild-type and  $pin3$  roots during the gravitropic response (reorientation by  $90^{\circ}$ ). The x-axis corresponds to the spatial coordinate (distance from quiescent center), while the temporal evolution is displayed along the y-axis.  $pin3$  roots had a smaller expansion zone and recovered substantially slower than wild-type roots. The spatio-temporal distribution of  $DGCR$  shows that the length of the curvature zone and the position of maximal  $DGCR$  varied in time (Fig. 5.9). During the first phase (from 0 h to 1 h) the curvature production zone of wild-type roots shifted and extended basally. Around the transition time between the first and second phase (1 h), the curvature zone extended basally within a short time into a region that was more than twice as large as before. From 1 h to 3 h the curvature zones overlapped, until around 3 h the intensity of the first zone (denoted by *apical* curvature zone; from 100  $\mu m$  to 200  $\mu m$ ) was drastically decreased. The second curvature zone (denoted as *basal* curvature zone, located 200  $\mu m$  to 300  $\mu m$  behind the quiescent center) curved with similar intensity and shifted slightly towards the base of the root.  $pin3$  roots, however, showed a completely different spatio-temporal distribution of curvature production (Fig. 5.9). The basal curvature zone was absent in  $pin3$  roots, while the apical curvature zone was still present. This suggests that the apical curvature zone, corresponding to the first phase, is not regulated by PIN3, while the basal curvature zone, corresponding to the second phase, depends on PIN3. A color coded representation of the average  $REGR$  distribution along the growth zone and across the width of wild-type and



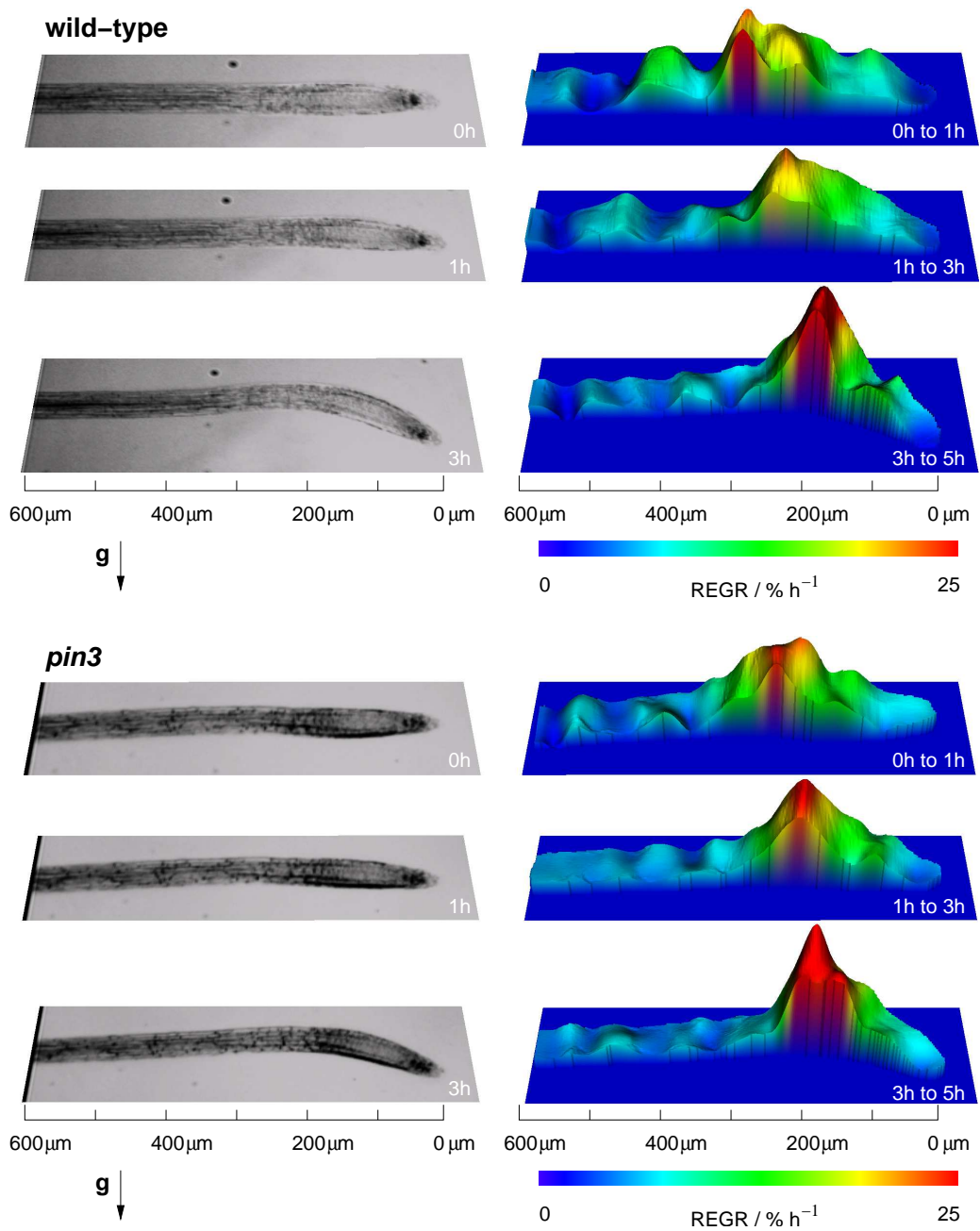


**Figure 5.10:** Color coded average relative elemental growth rate (*REGR*) distributions of selected wild-type and *pin3* roots during gravitropic reaction (reorientation by 90°). Growth is depicted through coloration and height of the surfaces shown on the right. The averages are over the first hour, from the first to the third hour and from the third to the fifth hour after reorientation. These are projected on original images, which are shown on the left side (at 0 h, 1 h and 3 h). Differential growth between the sides of the root produces curvature. The higher the asymmetry is, the more curvature is produced.

*pin3* roots, shown in Fig. 5.10, illustrates this observation. Both roots were rotated by 90° and their growth distribution averaged using Eq. (5.2) over the first hour, from the first to the third hour and from the third to the fifth hour. In this depiction, it can be shown that curvature was produced by differential growth between the sides of the root. During the first hour, the asymmetry in growth between the upper and bottom side of the roots was similar in the wild-type and *pin3* roots. Both roots showed a strong asymmetry in growth intensity apical of the growth maximum (apical curvature zone). From one hour to three hours, the plants differed substantially in overall growth intensity and growth asymmetry (Fig. 5.10). The wild-type root substantially reduced growth and created a strong asymmetry between the sides, reflecting a higher curvature production, particularly in a more basal part of the growth maximum (basal curvature zone). Differential growth also curved the *pin3* root, but slowdown and growth asymmetry were substantially less than in the wild-type root. From the third to the fifth hour growth increased again accompanied by a reduction in growth asymmetry in both plants.

As mentioned in Section 5.2.5, the growth distributions (Fig. 5.9) are normalized to obtain an average distribution with conserved form. Table 5.1 shows the average normalization coefficients used in the normalization Eqs. (5.6). Upon usage of these average parameters, the average normalized distribution was denormalized through the inverse of Eqs. (5.6).

### 5.3.2 Discussion

Differential growth in *pin3* roots is disturbed due to the missing PIN3 protein, which explains their defective gravitropic response (Friml et al., 2002). Our measurements confirmed this behavior, and showed that kinetics of curvature angle differ substantially between wild-type and *pin3* roots (Fig. 5.4). However, the kinetics of curvature angle do not suffice to understand the effects of PIN3 on differential growth. We therefore had to define a new analysis, based on spatio-temporal data (Figs. 5.6 and 5.8 to 5.10). Wild-type roots showed two phases of increasing *DGCR*: from 0 h to 1 h and from 1 h to 2 h followed by a phase of decreasing *DGCR* (Figs. 5.6 and 5.10). An apical curvature zone, which extends from 100  $\mu\text{m}$  to 200  $\mu\text{m}$  behind the quiescent center, is associated to the first phase, while the second phase is associated to a basal curvature zone located from 200  $\mu\text{m}$  to 300  $\mu\text{m}$  (Figs. 5.8 and 5.9). Concomitant activation of both curvature zones is reflected by a high *DGCR* between 1 h and 3 h, while inactivation of the apical curvature zone results in a reduction of curvature rate (from 2 h on; Figs. 5.6 and 5.9). The apical and basal curvature zones may constitute the two motors of gravitropism hypothesized recently (Wolverton et al., 2002a). Until now, the distal elongation zone (DEZ), a zone empirically defined to be between the meristem and the growth maximum (Ishikawa and Evans, 1993), was thought to be the location of the first motor (Ishikawa and Evans 1997; Mullen et al. 1998a;

Wolverton et al. 2002a). Growth distribution on the upper side of *A. thaliana* roots was found to be inhibited near the growth maximum and to shift apically, leading to the conclusion that the DEZ was responsible for curvature production (Mullen et al., 1998a). Although we found the apical curvature zone to have a maximum at 120  $\mu\text{m}$  (Fig. 5.8), it is still unclear if the apical curvature zone and the DEZ coincide. A determination of the DEZ through the growth distribution is difficult in *A. thaliana* roots, due to a uniform elongation in the meristem and an abrupt acceleration in the elongation zone (Fig. 3.1 on page 24; van der Weele et al. 2003). The apical curvature zone seems rather to be located at the basal meristem, where cell expansion and division overlap (Beemster et al., 2003). The second motor was hypothesized to be at the central elongation zone (CEZ), a zone located around the growth maximum, as it also had been reported to be responsible for curvature production (Selker and Sievers 1987; Wolverton et al. 2002a). However, neither had the location of the motors been clearly determined yet, nor had their actual existence definitively been proven. It was possible here for the first time to characterize the intensity of curvature production in time and along the roots, demonstrating the existence of the motors and allowing a determination of their location and time of activity (Fig. 5.9). The use of knockout mutants allowed additionally to show that the basal curvature zone (second motor) depends strongly on PIN3, while the apical curvature zone (first motor) is not affected by the absence of this protein (Figs. 5.6, 5.9 and 5.10). We conclude therefore that auxin mediates the basal curvature zone. However, the signal pathway involved in the first motor is still unclear, although hints for a possible cytokinin dependency exist (Aloni et al., 2004). As auxin, cytokinin is asymmetrically redistributed upon gravitropic stimulation. Because cytokinin reduces meristematic activity in the root (Werner et al., 2003), an asymmetric distribution of mitosis upon stimulation is expected and has been confirmed by measurements (Wagner, 1937). Our results show a growth asymmetry in the root meristem during the first 3 h of reaction (Fig. 5.10), confirming an adaptation of cell division, as cell cycle duration and meristematic growth are tightly bound in roots (Beemster et al. 2003; Chavarría-Krauser and Schurr 2004). The root apical meristem has to deliver enough cells to keep the expansion zone stable (Beemster et al., 2003), so that the first motor could be an adaptation of the meristematic activity to the following cell consuming second motor. We found not only a disturbed differential growth in *pin3* roots, but also a reduction of overall growth caused by a smaller expansion zone (Fig. 5.7). As PIN3 is involved in the axial redistribution of auxin in the columella cells, the absence of this protein could imply that auxin accumulation is higher in *pin3* roots. A smaller expansion zone is consistent with this, as has been shown by application of auxin and confirmed by a theoretical approach (Beemster and Baskin 2000; Chavarría-Krauser et al. 2005). We did not find a correlation between the positions of the first gravitropism motor and the growth maximum (Fig. 5.8), suggesting again an auxin-independent motor.

# Chapter 6

## Lateral CO<sub>2</sub> Diffusion Inside Leaves

### 6.1 Introduction

Leaves have a complex inner structure composed of several layers (Fig. 6.1). These inner structures of leaves are not densely packed to provide the photosynthetically active tissue with sufficient CO<sub>2</sub>. Stomata control the gas exchange between the leaf and outer air. These are regulated by environmental constraints mainly CO<sub>2</sub> and water availability (Farquhar and Sharkey 1982). The mesophyll, as the photosynthetically active tissue, consists of palisade tissue with longitudinal cells more densely packed than the loose spongy tissue. Vascular bundles, responsible for water and nutrient transport, are located within the mesophyll tissue. The vascular bundles are often surrounded by bundle sheaths (see e.g. Esau 1977), which in some species range from the upper to the lower epidermis separating air spaces inside the leaf. Leaves with such extensive bundle sheaths are designated as *heterobaric*, while leaves without are *homobaric* (Neger 1912; Neger 1918; Fig. 6.1). In homobaric leaves the air spaces may be connected to compose large and extensive air compartments, in which gas diffusion may occur over larger distances than in heterobaric leaves. Homobaricity can therefore enhance the lateral supply of CO<sub>2</sub>, which in turn may affect photosynthesis and net CO<sub>2</sub> exchange of leaves (Pieruschka et al. 2005a; Pieruschka 2005). The effect on photosynthesis has been currently discussed in literature (compare Morison et al. 2005; Pieruschka et al. 2005a; Pieruschka et al. 2005b).

One crucial step towards determining the relevance of lateral diffusion, is the accurate determination of the diffusivity inside the leaf. The structure of the air spaces in the parenchyma is complex and irregular (Fig. 6.1). However, the air spaces are small compared to the characteristic lengths found in CO<sub>2</sub> assimilation patterns, allowing to use a *homogenized diffusion coefficient*  $D$  to model lateral CO<sub>2</sub> diffusion. There are no direct experimental methods to measure the lateral diffusion coefficients. Mainly two approaches have been used, either through measurement of lateral CO<sub>2</sub> fluxes using double-gasket leaf chambers (Pieruschka

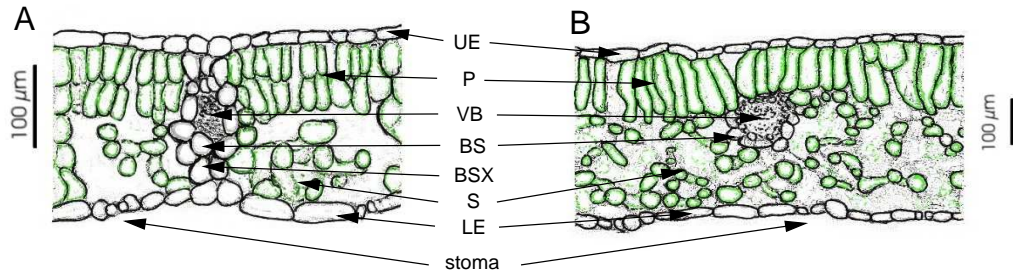


**Figure 6.1:** Cross sections of: A, heterobaric (*Glycine max*) and B, homobaric (*Vicia faba*) leaves. UE: upper epidermis, P: palisade tissue, VB: vascular bundle, BS: bundle sheath, BSX: bundle sheath extension, S: spongy tissue, LE: lower epidermis. Photosynthetically active tissues are marked green. Images adapted from Pieruschka 2005.

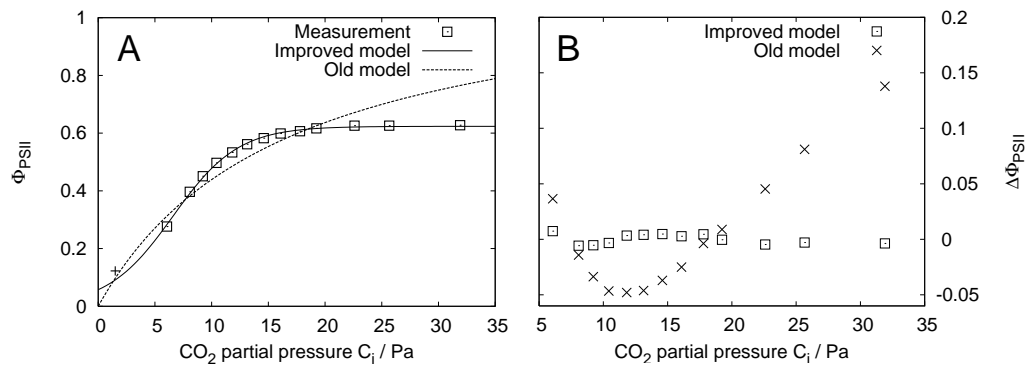


**Figure 6.2:** Quantum yield  $\Phi_{PSII}$  calibration models. A,  $\Phi_{PSII}$  measurement compared to model proposed by Morison et al. 2005 and improved model. The cross represents the measured compensation point. B, model residuals.

et al. 2005a), or through *chlorophyll fluorescence imaging* coupled to a mathematical model of lateral CO<sub>2</sub> diffusion (Galloët and Herbin 2005; Morison et al. 2005). The first relies on concentration gradients between the two gaskets and uses differences in net CO<sub>2</sub> exchange rates to determine  $D$  (Pieruschka et al. 2005a). These experiments have to be performed in darkness to avoid interferences of photosynthetic CO<sub>2</sub> uptake and photorespiratory CO<sub>2</sub> evolution in light. The second is based on the measurement and calculation of CO<sub>2</sub> concentration profiles, which are then used to determine  $D$  through minimization of a suitable error functional (Galloët and Herbin 2005; Morison et al. 2005). Here, the later was chosen in order to measure  $D$  and estimate the impact of lateral CO<sub>2</sub> fluxes on photosynthesis.

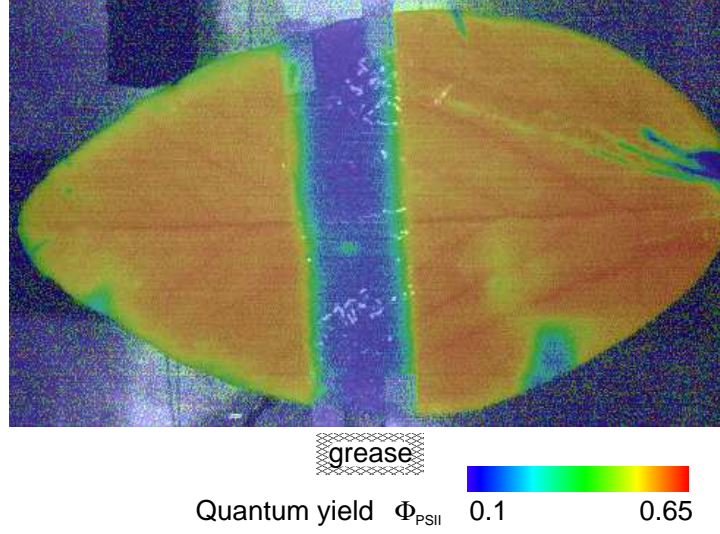


**Figure 6.3:** Chlorophyll fluorescence image of a *Vicia faba* leaf with a greased area, where gas exchange is prevented. The quantum yield  $\Phi_{PSII}$  is shown overlaid on the visual image.

## 6.2 Calibration model

Gas exchange measurements deliver only average leaf internal  $\text{CO}_2$  concentrations. To obtain spatial concentration patterns one has to rely on chlorophyll fluorescence imaging (Morison et al. 2005). The chlorophyll fluorescence parameter  $\Phi_{PSII} = F'_q/F'_m$ , also known as *quantum yield*, is a measure of the proportion of light energy (absorbed by photosystem II) used in photosynthetic electron transport. Fig. 6.3 shows the  $\Phi_{PSII}$  distribution of a leaf with a grease covered area. The grease prevents gas exchange, resulting in a substantially lower  $\Phi_{PSII}$  as a consequence of low  $\text{CO}_2$  partial pressure. The  $\text{CO}_2$  partial pressure  $C_i$  inside the leaf and  $\Phi_{PSII}$  are functionally related (Fig. 6.2). Morison et al. 2005 proposed a simple hyperbolic model

$$\Phi_{PSII} = \frac{\Phi_{max} C_i}{K_m + C_i}, \quad (6.1)$$

where  $\Phi_{max}$  and  $K_m$  are parameters. Common linear regression can be used on suitably transformed variates ( $C_i \mapsto C_i^{-1}$  and  $\Phi_{PSII} \mapsto \Phi_{PSII}^{-1}$ ) to fit this model to measurements of average  $\Phi_{PSII}$  for given  $C_i$ s. However, the residuals are unacceptable, because of the remaining functional dependence (Fig. 6.2, B). We therefore propose an improved model based on a sigmoid function

$$\Phi_{PSII} = \frac{\Phi_{max}}{1 + \exp\left(-\frac{C_i - C_{i,0}}{\sigma}\right)}, \quad (6.2)$$

**Table 6.1:** Quantum yield  $\Phi_{PSII}$  against CO<sub>2</sub> partial pressure  $C_i$  calibration parameters of proposed model and model of Morison et al. 2005. Proposed model is significantly better than the old model (F-Test:  $P < 0.0001$ ).

Model	$\Phi_{max}$	$K_m$ (Pa)	$C_{i,0}$ (Pa)	$\sigma$ (Pa)	$r^2$
Morison et al. 2005	1.16	16.4	—	—	0.88
Proposed	0.624	—	6.59	2.88	0.998

where  $\Phi_{max}$ ,  $C_{i,0}$  and  $\sigma$  are parameters. Eq. (6.2) describes a sample calibration curve significantly more accurate than the model proposed by Morison et al. 2005 (F-Test:  $P < 0.0001$ ; Table. 6.1; Fig. 6.2, A and B). Moreover, the proposed model is also able to extrapolate for small  $C_i$  accurately, as becomes clear by comparing the model to the compensation point determined through gas exchange measurements (cross in Fig. 6.2, A). After a calibration curve has been obtained for the given environmental conditions, and after the model (6.2) has been fitted (parameters shown in Table 6.1), it is simple to apply the inverse of (6.2) to obtain  $C_i$  distributions from  $\Phi_{PSII}$  fluorescence images (Fig. 6.3).

### 6.3 Lateral diffusion model

The transport equation of CO<sub>2</sub> in leaves is given by three overlapping processes: respiration, assimilation and diffusion (Galloët and Herbin 2005). Leaf cells bind CO<sub>2</sub> through photosynthesis, and as all cells, respire and produce CO<sub>2</sub>. An additional process designated *photorespiration* is closely linked to photosynthesis due to competitive binding of CO<sub>2</sub> and O<sub>2</sub> by the RubisCO enzyme, which catalyzes CO<sub>2</sub> fixation. However, the experiments presented here were performed under non-photorespiratory conditions (1% O<sub>2</sub>); photorespiration can thus be neglected. The transport of CO<sub>2</sub> can be approximately described by Fick's empirical law (Giovangigli 1999). The respiration rate  $\kappa_{resp}$  can be assumed to be constant and given, while assimilation is described by standard photosynthesis models (von Caemmerer 2000)

$$\kappa_{PS}(C_i) = \frac{(C_i - \Gamma_*) A_{max}}{C_i + K_c (1 + O/K_o)}, \quad (6.3)$$

where  $A_{max}$ ,  $K_c$  and  $K_o$  are the maximal rate and Michaelis-Menten constant of carboxylation and oxygenation respectively,  $C_i$  and  $O$  are the chloroplastic partial pressures of CO<sub>2</sub> and oxygen respectively.  $\Gamma_*$  is given by

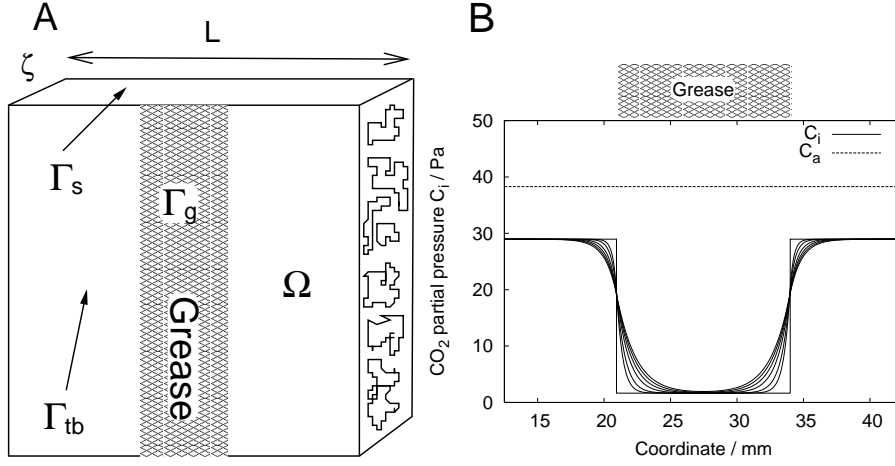


**Figure 6.4:** Lateral  $\text{CO}_2$  diffusion model. A, model domain  $\Omega$  of part of a leaf of width  $\zeta$  and length  $L$ . An area  $\Gamma_g$  is covered by grease.  $\Gamma_s$  is the boundary around the domain, while  $\Gamma_{tb}$  is the boundary at the top and the bottom of  $\Omega$ . B, steady-state solution of  $\text{CO}_2$  diffusion model. Each curve corresponds to a relative diffusion coefficient  $D' = D/D_{fa}$  of: 0, 0.05, 0.1, 0.2, 0.3, 0.4 and 0.5.  $D_{fa}$  is the  $\text{CO}_2$  free air diffusion coefficient.

$$\Gamma_* = \frac{0.5 O}{S_{c/o}}, \quad (6.4)$$

where  $S_{c/o}$  is the relative specificity of RubisCO to  $\text{CO}_2$  and oxygen (von Caemmerer 2000).

Let  $\Omega$  be a model domain describing part of the leaf with an area covered with grease (Fig. 6.4, A). Let  $\Gamma_s$  be the boundary surrounding the domain, while  $\Gamma_{tb}$  denotes the top and bottom boundary of  $\Omega$ . The boundary describing the greased area is denoted by  $\Gamma_g \subset \Gamma_{tp}$ . The steady state concentration distribution is then given by the transport problem

$$\begin{aligned} -D \Delta C_i + \kappa_{PS} - \kappa_{resp} &= 0 && \text{in } \Omega \\ \nabla C_i \cdot \mathbf{n} &= 0 && \text{on } \Gamma_s, \\ D \nabla C_i \cdot \mathbf{n} &= j_{in} && \text{on } \Gamma_{tb} \end{aligned} \quad (6.5)$$

where  $D$  is the  $\text{CO}_2$  homogenized diffusion coefficient in the leaf, and  $j_{in}$  can be approximated by (von Caemmerer and Farquhar 1981)

$$j_{in}(C_i, x) = \chi_{\Gamma_{tb} \setminus \Gamma_g}(x) \left( g_s (C_a - C_i) - \frac{E}{2} (C_a + C_i) \right), \quad x \in \Omega, \quad (6.6)$$

where  $\chi_{\Gamma_{tb} \setminus \Gamma_g}$  is the indicator function<sup>1</sup> of  $\Gamma_{tb} \setminus \Gamma_g$ ,  $C_a$  is the  $\text{CO}_2$  partial pressure

<sup>1</sup>The indicator function  $\chi_A$  of a set  $A$  is given by  $\chi_A(x) = 1$  for  $x \in A$ , zero elsewhere.

outside the leaf and  $E$  is the water transpiration rate. Integrating over the leaf thickness and using the boundary conditions imposed [Eq. (6.5)], a one dimensional problem is obtained

$$\boxed{\begin{aligned} -D \frac{d^2 C_i}{dx^2} + \frac{(C_i - \Gamma^*) A_{max}}{C_i + K_c (1 + O/K_o)} &= \kappa_{resp} + \frac{j_{in}}{\zeta} & , 0 < x < L \in \mathbb{R} \\ d_x C_i &= 0 & , x \in \{0, L\} \subset \mathbb{R} \end{aligned}} \quad (6.7)$$

where  $\zeta$  and  $L$  are thickness and length of  $\Omega$  respectively (compare Fig. 6.4, A). This is the sought for problem to model the CO<sub>2</sub> concentration distribution. The diffusion coefficient  $D$  in leaves depends on the porosity of the inner structure (Fig. 6.1). Some plant species, such as *V. faba* have a high porosity, other such as CAM plants, have low porosity.  $D$  is thus expected to be between 0 and  $D_{fa}$ , where  $D_{fa}$  is the CO<sub>2</sub> diffusion coefficient in free air ( $D_{fa} = 1.51 \cdot 10^{-5} \text{ m}^2 \text{ s}^{-1}$ , at 20° C under standard atmospheric pressure, Nobel 1999). In the sequel, the relative diffusion coefficient  $D' = D/D_{fa}$  will be stated instead.

Parameter	Value
$\zeta$	479 $\mu\text{m}$
$A_{max}$	195.7 $\text{Pa s}^{-1}$ ( $\hat{=}$ 38.6 $\mu\text{mol m}^{-2} \text{ s}^{-1}$ )
$K_c$	40.4 $\text{Pa}$
$K_o$	$24.8 \cdot 10^3 \text{ Pa}$
$O$	$10^3 \text{ Pa}$ ( $\hat{=}$ 1% O <sub>2</sub> )
$S_{c/o}$	2837.8
$\kappa_{resp}$	6.6 $\text{Pa s}^{-1}$ ( $\hat{=}$ 1.3 $\mu\text{mol m}^{-2} \text{ s}^{-1}$ )
$g_s$	$3.96 \cdot 10^{-3} \text{ m s}^{-1}$ ( $\hat{=}$ 163 $\text{mmol m}^{-2} \text{ s}^{-1}$ )
$E$	$6.17 \cdot 10^{-5} \text{ m s}^{-1}$ ( $\hat{=}$ 2.54 $\text{mmol m}^{-2} \text{ s}^{-1}$ )
$C_a$	38.28 $\text{Pa}$

**Table 6.2:** Lateral CO<sub>2</sub> diffusion simulation parameters.

Eq. (6.7) can be solved using a standard *discrete difference* approximation (Stoer and Burlisch 2000b). The resulting system of equations is not linear due to the assimilation rate (6.3), and was thus solved using *Newton's method* (Stoer and Burlisch 2000a). Fig. 6.4, B shows the solutions of Eq. (6.7) for the model parameters shown in Table 6.2 and for varying  $D'$ : 0, 0.05, 0.1, 0.2, 0.3, 0.4 and 0.5. An ideal heterobaric leaf has  $D' = 0$ , while a homobaric leaf, such as *V. faba*, has  $D' = 0.3 - 0.5$ .

Leaf internal CO<sub>2</sub> partial pressures are measured through gas fluxes by application of Eq. (6.6) on the net CO<sub>2</sub> and water fluxes (von Caemmerer 2000). This can be used to determine one photosynthesis parameter, by application of mass conservation (6.3) at the boundary. Most of the parameters in (6.3) are RubisCO specific and hence very well determined. Therefore, the maximal assimilation rate  $A_{max}$ , which substantially varies between species and environmental conditions, is the best candidate. This is how  $A_{max}$  shown in Table 6.2 was determined.

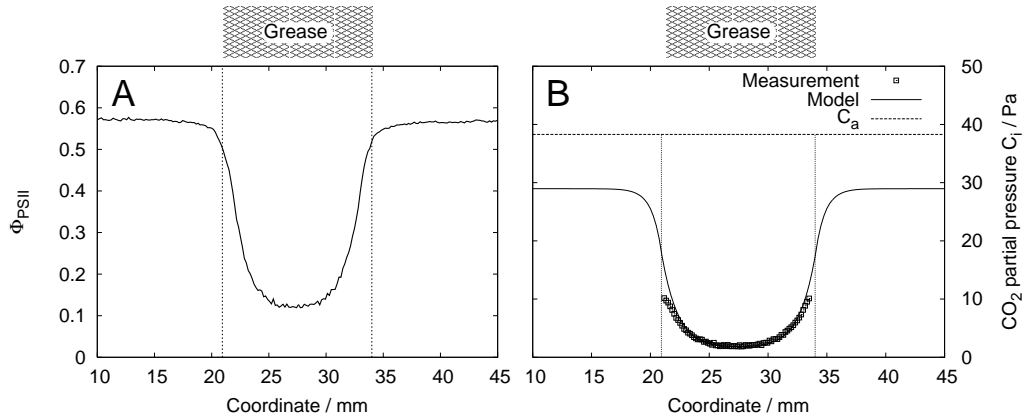


**Figure 6.5:** Fit of relative diffusion coefficient  $D' = D/D_{fa}$  to a measurement of a homobaric (*Vicia faba*) leaf. A, quantum yield  $\Phi_{PSII}$  average profile. B, model result against measurement values ( $D' = 0.44$ ).

Two photosynthesis parameters could be determined, when a long range  $\text{CO}_2$  gradient would be present (e.g. using double-gasket chambers). Additionally to  $A_{max}$ , the respiration rate  $\kappa_{resp}$ , which is measured in dark-adapted leaves (no photosynthesis), could be obtained. Until now it is not clear if  $\kappa_{resp}$  changes between dark-adapted and light-exposed leaves (Atkin et al. 1998; Loreto et al. 2001).

## 6.4 Diffusion coefficients from concentration profiles

After having established the diffusion model and its parameters, the homogenized diffusion coefficient  $D$  can be obtained from measurements. These measurements are calibrated as described in Section 6.2 using the model (6.2) with the parameters listed in Table 6.1. However, before  $D'$  can be fitted to the data, average  $C_i$  profiles need to be obtained. This is accomplished by averaging the quantum yield data (Fig. 6.3) perpendicular to the grease boundary, resulting in far less noisy data than in single profiles (compare Morison et al. 2005). Subsequently,  $D'$  is fitted to the measurement through minimization of an error functional. Due to its good stability we chose to use the relative error as the kernel of the error functional (Galloët and Herbin 2005)

$$J_{err} := \sum_{\alpha=1}^N \frac{|C_i(x_\alpha) - c_i^\alpha|}{c_i^\alpha}, \quad (6.8)$$

where  $N$  is the amount of measurements,  $(x_\alpha, c_i^\alpha)$  is the  $\alpha$ -th measurement and  $C_i(x_\alpha)$  is the model value at position  $x_\alpha$ . Because only one parameter is estimated, Brent's minimization algorithm was used (implemented in *GNU Scientific Library*

**Table 6.3:** Lateral CO<sub>2</sub> diffusion flux effect for different relative diffusion coefficients  $D' = D/D_{fa}$ . Refer to Fig. 6.6 for a description of the areas  $I$  and  $II$  and the diffusion distances  $\Delta x_I$  and  $\Delta x_{II}$ .  $K$ : net CO<sub>2</sub> assimilation flux.  $\Delta I$  and  $\Delta K$  represent the difference to the ideal heterobaric leaf ( $D' = 0$ ), while  $\Delta x_I$  and  $\Delta x_{II}$  measure the diffusion distance into area  $I$  and  $II$  respectively. Fluxes are given in  $\mu\text{mol m}^{-2} \text{s}^{-1}$  and distances in  $\text{mm}$ .

$D'$	$K$ ( $I + II$ )	$\Delta K$	$I$	$II$ ( $\Delta II$ )	$\Delta I$	$\Delta x_I$	$\Delta x_{II}$
0	299.4	0	299.4	0	0	0	0
0.05	307.5	8.1	297.0	10.5	-2.4	0.5	2.17
0.1	311.4	12.0	296.2	15.2	-3.2	0.75	3.17
0.2	317.0	17.6	295.0	22.0	-4.4	1.08	4.5
0.3	321.2	21.8	294.1	27.1	-5.3	1.33	5.5
0.4	324.8	25.4	293.4	31.4	-6.0	1.5	6.42
0.5	328.0	28.6	292.7	35.3	-6.7	1.67	7.17

(*GSL*); Stoer and Burlisch 2000a). Fig. 6.5 shows the results for the dataset presented in Fig. 6.3. Due to the saturation of  $\Phi_{PSII}$  for high CO<sub>2</sub> levels (Fig. 6.2), high CO<sub>2</sub> partial pressures are systematically underestimated. The measurements were thus restrained to CO<sub>2</sub> partial pressures lower or equal to 10 Pa. The concentration in the greased regions tends to reach the compensation point<sup>2</sup>, because the size of the grease strip  $\Gamma_g$  is large enough. The compensation point and the CO<sub>2</sub> distribution are described accurately by the model. The diffusion coefficient was determined to be  $D' = 0.44$  (corresponding to  $D = 6.7 \cdot 10^{-6} \text{ m}^2 \text{ s}^{-1}$ ), and is substantially larger than the results of other measurement techniques (Pieruschka et al. 2005a). This is probably a consequence of how Pieruschka et al. 2005a conducted the experiments. They determined  $D$  from lateral diffusion fluxes over distances of 6 mm to 8 mm, increasing the occurrence of densely packed tissue and thus underestimating the local occurring  $D$ .

## 6.5 Lateral diffusion effect

The relevance of lateral diffusion in photosynthesis can be estimated by solving Problem (6.7) for a set of different diffusion coefficients and comparing the average net assimilation to those of an ideal heterobaric leaf ( $D' = 0$ ). The CO<sub>2</sub> distribution around a grease boundary in a homobaric leaf, can be classified into

<sup>2</sup>Compensation point  $\Gamma$ : CO<sub>2</sub> concentration at which no net assimilation occurs, i.e.  $\kappa_{resp} = \kappa_{PS}$ .

two areas designed *I* and *II* (ungreased and greased; Fig. 6.6). These areas characterize the differences in CO<sub>2</sub> partial pressure between homobaric and ideal heterobaric leaves. Using (6.7), the net CO<sub>2</sub> exchange rate (*NCER*) can be determined

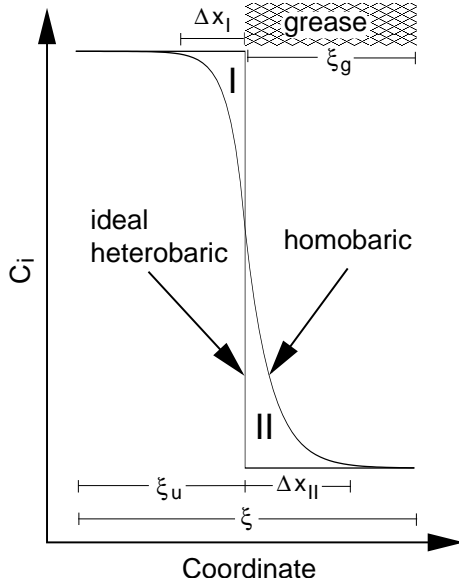


**Figure 6.6:** Lateral CO<sub>2</sub> diffusion effect. Area *I* and *II* determine the effect on the ungreased and greased sides respectively.  $\Delta x_I$  and  $\Delta x_{II}$  give the diffusion distances into areas *I* and *II* respectively (distance between grease boundary and where the difference in  $C_i$  is 5% of the heterobaric value).  $\xi_u$  and  $\xi_g$  are the lengths of the ungreased and greased regions respectively, while  $\xi = \xi_u + \xi_g$ .

$$NCER = \frac{1}{\xi_u} \int_0^{\xi_u} j_{in} dx, \quad (6.9)$$

where  $\xi_u$  is the length of the ungreased region (Fig. 6.6). The *NCER* is delivered by gas exchange equipment and is thus widely used by experimenters. A short calculation based on Eq. (6.9) and Problem (6.7) shows

$$NCER = \frac{\zeta}{\xi_u} K, \quad (6.10)$$

where  $\zeta$  is the leaf thickness and  $K$  is the net CO<sub>2</sub> assimilation flux

$$K = \int_0^{\xi} (\kappa_{PS} - \kappa_{resp}) dx, \quad (6.11)$$

where  $\xi = \xi_u + \xi_g$  is the length of the ungreased and greased regions. The difference in  $K$  between an ideal heterobaric and a homobaric leaf renders the effect of lateral diffusion on photosynthesis

$$\Delta K = \int_0^{\xi} (\kappa_{PS}(C_i) - \kappa_{PS}(C_i^{ht})) dx,$$

where  $C_i$  and  $C_i^{ht}$  are the CO<sub>2</sub> partial pressure distributions of homobaric and ideal heterobaric leaves, respectively. The use of  $\Delta K$  instead of  $\Delta NCER$  allows to estimate the strength of the effect for other leaf dimensions ( $\zeta$  and  $\xi_u$ ).

In addition to  $K$ , the diffusion effect can be estimated through the diffusion distances  $\Delta x_I$  and  $\Delta x_{II}$ , which characterize the range of the effect into the ungreased and greased regions respectively (Fig. 6.6). This distance is defined as

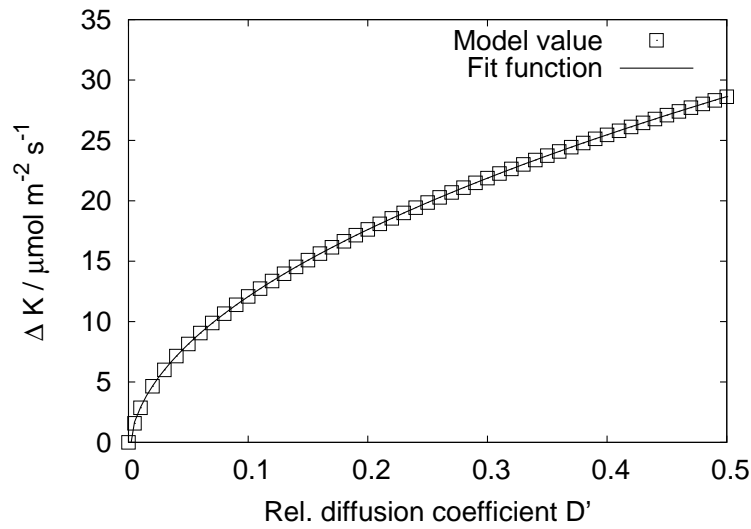
the one between the grease boundary and where the difference in CO<sub>2</sub> partial pressure is 5% of the heterobaric value. The solution of the ideal heterobaric leaf is constituted by two values:  $C_i^{ht} = \text{const}$  in ungreased region and compensation point  $\Gamma = \text{const}$  in greased region. The transition between these values is sharp (compare Fig. 6.4, B). However, in a homobaric leaf, the transition is continuous. Depending on distance to the leaf boundary and size of the grease strip, the compensation point and the ideal value at the boundary may even not be reached. By choosing the simulation domain carefully (essentially large enough), these cases are discarded to allow a calculation of the diffusion distances.

Table 6.3 lists the model results for  $K$ ,  $\Delta K$ ,  $\Delta x_I$  and  $\Delta x_{II}$ . As expected the diffusion distances increase with  $D'$ .  $K$  and hence  $\Delta K$  also increase and reflect an overall larger  $NCEP$  in homobaric leaves (Fig. 6.7), although photosynthesis parameters were kept constant (Table 6.2). The effect strength  $\Delta K$  can be fitted by a simple function

$$\Delta K = \alpha \sqrt{D'} + \beta, \quad (6.12)$$

where  $\alpha$  and  $\beta$  are coefficients. For the set of simulation parameters in Table 6.2, we found an excellent accordance of (6.12) with the model results ( $\alpha = 42.4 \mu\text{mol m}^{-2} \text{s}^{-1}$  and  $\beta = 1.34 \mu\text{mol m}^{-2} \text{s}^{-1}$ ;  $r^2 = 0.999996$ ). Eq. (6.12) together with the given parameters, allow to determine the effect strength for a given  $D'$  through a simple calculation. Note however that  $\alpha$  and  $\beta$  depend on the simulation parameters, Table 6.2, and should not be used for measurements conducted in other environmental conditions.

These results can be interpreted as follows. Homobaric leaves may exploit the CO<sub>2</sub> resources more efficiently than heterobaric, because of more effective utilization of CO<sub>2</sub>. In particular, water use efficiency. These leaves may have an advantage when exposed to sun flecks, because the light exposed tissue obtains additional respiratory CO<sub>2</sub> from the shaded tissue (Pieruschka et al. 2005b). Such sunflecks have been reported to substantially contribute to overall plant carbon gain in shaded environment (Percy et al. 1996; Pfitsch and Percy 1989). The model presented here is easily adapted to this situation. Instead of having a coordinate dependent  $j_{in} = j_{in}(C_i, x)$ , a coordinate dependent  $A_{max} = A_{max}(x)$  must be introduced. The effects should, however, be similar to the here presented.



**Figure 6.7:** Net assimilation flux  $\Delta K$  against relative diffusion coefficient  $D' = D/D_{fa}$ . A simple fit function is also shown:  $\Delta K = 42.39\sqrt{D'} - 1.34$ ,  $r^2 = 0.999996$ .



# Chapter 7

## Concluding remarks and perspectives

*Change return success  
Going and coming without error  
Action brings good fortune  
Sunset Sunrise*

Syd Barrett, 1967

Throughout this work, some applications of transport equations in plant biology were presented. The application focused mainly on the scarcely treated field of cell and tissue growth. On the cell scale, an initial approach to modeling subcellular growth patterns was proposed and demonstrated using a simple example. On the tissue level, the interplay between cell and tissue scale was demonstrated through introduction of a control mechanism based on phytohormones. This shows, that organ growth models should not solely be determined by cellular properties, such as turgor, wall extensibility, etc., but also by control mechanisms that operate on an organismic/tissue level (e.g. auxin transport).

However, the mechanical effect of surrounding cells on cell growth stays untreated. This may become one of the major future challenges of tissue modeling. Until now, several approaches exist to model tissue mechanics (see e.g. Niklas 1992). However, these do not focus on the mechanical properties of growing tissue or how growing cells interact mechanically. These models are restricted to short time scales, in which tissues behave as elastic bodies. On larger time scales, tissues deform/flow due to growth. Moreover, cells are able to communicate exchanging compounds, introducing coordination and affecting the mechanical properties of their walls. An example of such a complex interaction is the gravitropic reaction of roots, and was thus treated in the here presented work.

Gradients in auxin are used by the organ to control extension of the flanks and result in curvature of the organ. This shows how closely related are compound transport, mechanical properties and growth.

In addition to growth, an application of transport equations on leaf CO<sub>2</sub> exchange modeling was presented. The simple model presented here, describes quantitatively the lateral diffusion of CO<sub>2</sub> in leaves. Nonetheless, many questions remain unanswered. For example, the transport of CO<sub>2</sub> into the leaf through stomata is still unclear. The current model assumes that it occurs solely on a diffusional basis, and does not take into account that leaves are not packed densely and gas exchange between stomata is possible. To treat this issue properly, a multi-component flow of CO<sub>2</sub>, O<sub>2</sub>, H<sub>2</sub>O, etc., should be coupled to leaf geometry and to photosynthetic models. An accurate CO<sub>2</sub> transport model is not only essential for plant physiology, but also for climatic research. It is thus of relevance to improve the current model.

The work presented here shows how challenging the quantitative description of biological systems is. Descriptive biology has reached its bounds already since a long time. Modern biologists need quantitative approaches to refine and improve their models. A synthesis of mathematical, physical and biological models has thus become essential and is becoming an established approach in biology. Biological systems, from a molecular to an ecological level, pose everyday new unanswered questions. An interdisciplinary approach may be the only way to find answers.

# Bibliography

- Aloni R, Langhals M, Aloni E, Ullrich CI (2004) Role of cytokinin in the regulation of root gravitropism. *Planta* **220**, 177–182.
- Atkin OK, Evans JR, Siebke K (1998) Relationship between the inhibition of the leaf respiration by light and enhancement of leaf dark respiration following light treatment. *Australian journal of Plant Physiology* **25**, 437 – 443.
- Audus LJ (1964) Geotropism and the modified sine rule: an interpretation based on the amyloplast statolith theory. *Physiologia Plantarum* **17**, 737 – 745.
- Barlow PW (1992) A flow-chart of the processes responsible for gravitropism, nutation and other growth movements of roots. *Naturwissenschaften* **79**, 34–39.
- Barlow PW, Parker JS, Butler R, P. B (1993) Gravitropism of primary roots of *Zea mays* L. at different displacement angles. *Annals of Botany* **71**, 383–388.
- Beemster GTS, Baskin TI (1998) Analysis of cell division and elongation underlying the developmental acceleration of root growth in *Arabidopsis thaliana*. *Plant Physiology* **116**, 1515–1526.
- Beemster GTS, Baskin TI (2000) STUNTED PLANT 1 mediates effects of cytokinin, but not of auxin, on cell division and expansion in the root of *Arabidopsis*. *Plant Physiology* **124**, 1718–1727.
- Beemster GTS, Fiorani F, Inzé D (2003) Cell cycle: the key to plant growth control? *TRENDS in Plant Science* **8** (4), 154–158.
- Berntson GM (1997) Topological scaling and plant root system architecture: Developmental and functional hierarchies. *New Phytologist* **35**, 621–634.
- Bigün J, Granlund G (1987) Optimal orientation detection of linear symmetry. In: Proc. First Int. Conf. on Computer Vision (ICCV '87, London, June 8–11, 1987) IEEE Computer Society Press, Washington, pp. 433–438.
- Black MJ, Rangarajan A (1996) On the unification of line process, outlier rejection, and robust statistics with application in early vision. *International Journal of Computer Vision* **19** (1), 57–91.

- Blancaflor EB, Masson PH (2003) Plant gravitropism. Unraveling the ups and downs of a complex process. *Plant Physiology* **133**, 1677–1690.
- Blilou I, Xu J, Wildwater M, Willemsen V, Paponov I, Friml J, Heidstra R, Aida M, Palme K, Scheres B (2005) The PIN auxin efflux facilitator network controls growth and patterning in *Arabidopsis* roots. *Nature* **433**, 39–44.
- Boyer JS (1968) Relationship of water potential to growth of leaves. *Plant Physiology* **43**, 1056–1062.
- Boyer JS, Silk WK (2003) Hydraulics of plant growth. *Functional Plant Biology* **31**, 761–773.
- Brumfield RT (1942) Cell growth and division in living root meristems. *American Journal of Botany* **29**, 533–543.
- Buckner AJF, Hooker JE, Black KE (1996) Mathematical and simulation modeling of root systems architecture. *Mathematical Biosciences* **127**, 136.
- Chavarría-Krauser A, Jäger (2005) Barodiffusion effects in bifurcating capillaries. *Computing and Visualization in Science* , In press.
- Chavarría-Krauser A, Jäger W, Schurr U (2005) Primary root growth: a biophysical model of auxin-related control. *Functional Plant Biology* **32** (9), 849–862.
- Chavarría-Krauser A, Schurr U (2004) A cellular growth model for root tips. *Journal of Theoretical Biology* **230** (1), 21–32.
- Chen R, Rosen E, Masson PH (1999) Gravitropism in higher plants. *Plant Physiol* **120**, 343–350.
- Cosgrove DJ (1986) Biophysical control of plant cell growth. *Annual Review of Plant Physiology* **37**, 377–405.
- Cosgrove DJ (1992) Wall extensibility: its nature, measurement and relationship to plant cell growth. *New Phytologist* **124**, 1–23.
- Cosgrove DJ (1993) Water uptake by growing cells: An assessment of the controlling roles of wall relaxation, solute uptake, and hydraulic conductance. *International Journal of Plant Sciences* **154**(1), 10–21.
- Cosgrove DJ (2000) Loosening of plant cell walls by expansins. *Nature* **407**, 321–326.
- del Pozo JC, Lopez-Matas MA, Ramirez-Parra E, Gutierrez C (2005) Hormonal control of the plant cell cycle. *Physiologia Plantarum* **123**, 173–183.
- Eapen D, Barroso ML, Ponce G, Campos ME, Cassab GI (2005) Hydrotropism: root growth responses to water. *TRENDS in Plant Science* **10**, 44–50.

- Erickson RO (1976) Modeling of plant growth. *Annual Review of Plant Physiology* **80**, 309–315.
- Erickson RO, Sax KW (1956) Experimental growth rate of primary root of *Zea mays*. *Proceedings of the American Philosophical Society* **100**, 487–498.
- Esau K (1977) Anatomy of seed plants. John Wiley & Sons.
- Esmon CA, Pedmale UV, Liscum E (2005) Plant tropisms: providing the power of movement to a sessile organism. *Int J Dev Biol* **49**, 665–674.
- Evans LS, Lagrazon K, Pancrudo J (2001) Diversity of cell length in terminal portion of roots: location of the proliferative cell population. *Environmental and Experimental Botany* **45**, 85–94.
- Evans LS, Moore M, Hasenstein KH (1986) How roots respond to gravity. *Scientific American* **254**, 112–119.
- Farquhar GD, Sharkey TD (1982) Stomatal conductance and photosynthesis. *Annual Review of Plant Physiology* **33**, 317 – 345.
- Fitter AH, Stickland TR, Harvey ML, Wilson GW (1991) Architectural analysis of plant root systems first architectural correlates of exploitation efficiency. *New Phytologist* **118**, 375–382.
- Friml J, Palme K (2002) Polar auxin transport – old questions and new concepts? *Plant Molecular Biology* **49**, 273–284.
- Friml J, Wiśniewska J, Benková E, Mendgen K, Palme K (2002) Lateral relocation of auxin efflux regulator PIN3 mediates tropism in *Arabidopsis*. *Nature* **415**, 806–809.
- Galloët E, Herbin R (2005) Axisymmetric finite volumes for the numerical simulation of bulk CO<sub>2</sub> transport and assimilation in a leaf. *International Journal of Finite Volumes* , .
- Génard M, Fishman S, Vercambre G, Huget J, Bussi C, Besset J, Habib R (2001) A biophysical analysis of stem and root diameter variations in woody plants. *Plant Physiol* **126**, 188–202.
- Gerlich G (1991) Einführung in die Prinzipien und Methoden der theoretischen Physik. Technische Universität Braunschweig, Braunschweig.
- Giovangigli V (1999) Multicomponent flow modeling. Birkhäuser.
- Goodwin RH, Stepka W (1945) Growth and differentiation in the root tip of *Phleum pratense*. *American Journal of Botany* **32**, 36–46.

- Großmann C, Roos HG (1994) Numerik partieller Differentialgleichungen., 2nd Edition B.G. Teubner.
- Halliday D, Resnick R (1988) Fundamentals of Physics., 3rd Edition John Wiley & Sons, Ch. 11, p. 244.
- Hammer Ø (1998) Diffusion and direct signaling models are numerically equivalent. *Journal of Theoretical Biology* **192**, 129–130.
- Haußecker H, Spies H (1998) Motion. In: Jähne B (Ed.), Handbook on computer vision and applications Academic Press, New York, pp. 310–369.
- Hejnowicz Z, Hejnowicz K (1991) Modeling the formation of root apices. *Planta* **184**, 1–7.
- Ishikawa H, Evans M (1993) The role of the distal elongation zone in the response of maize roots to auxin and gravity. *Plant Physiology* **102**, 1203–1210.
- Ishikawa H, Evans M (1997) Novel software for analysis of root gravitropism: comparative response patterns of *Arabidopsis* wild type and *axr1* seedlings. *Plant Cell Environ* **20**, 919–928.
- Ishikawa H, Hasenstein K, Evans M (1991) Computer-based video digitizer analysis of surface extension in maize roots - kinetics of growth rate changes during gravitropism. *Planta* **181**, 381–390.
- Ivanov VB, Maximov VN (1999) The change in the relative rate of cell elongation along the root meristem and the apical region of the elongation zone. *Russian Journal of Plant Physiology* **46**, 87–97.
- Jähne B (1997) Digital Image processing. Springer.
- Johnsson A (1965) Investigations of the reciprocity rule by means of geotropic and geoelectric measurements. *Physiol Plant* **18**, 945–967.
- Kauss H (1978) Osmotic regulation in algae. *Progress in Phytochemistry* **5**, 1–27.
- Kramer EM (2004) PIN and AUX/LAX proteins: their role in auxin accumulation. *TRENDS in Plant Science* **9**, 1360–1385, doi:10.1016/j.tplants.2004.10.010.
- Lai I, Scharr H, Chavarría-Krauser A, Küsters R, Wu J, Chou C, Schurr U, Walter A (2005) Leaf growth dynamics of two congener gymnosperm tree species reflect the heterogeneity of light intensities given in their natural ecological niche. *Plant Cell and Environment* **28**, 1496–1505.
- Landau LD, Lifschitz EM (1987) Statistische Physik Teil I., 3rd Edition Akademie Verlag, Berlin.

- Landau LD, Lifschitz EM (1991a) *Elastizitätstheorie.*, 7th Edition Akademie Verlag, Berlin.
- Landau LD, Lifschitz EM (1991b) *Hydrodynamik.*, 5th Edition Akademie Verlag, Berlin.
- Larsen P (1957) The development of geotropic and spontaneous curvatures in roots. *Physiologia Plantarum* **10**, 12–163.
- Lockhart JA (1965) An analysis of irreversible plant cell elongation. *Journal of Theoretical Biology* **8**, 264–75.
- Loreto F, Velikova V, Di Marco G (2001) Respiration in the light measured by  $^{12}\text{CO}_2$  emission in  $^{13}\text{CO}_2$  atmosphere in maize leaves. *Australian Journal of Plant Physiology* **27**, 1103 – 1108.
- Lüttge U, Kluge M (2002) *Botanik.* Wiley-VCH.
- Maurel C (1997) Aquaporins and water permeability of plant membranes. *Annual Review of Plant Physiology* **48**, 399–429.
- Morison JIL, Gallouët E, Lawson T, Cornic G, Herbin R, Baker NR (2005) Lateral diffusion of  $\text{CO}_2$  in leaves is not sufficient to support photosynthesis. *Plant Physiology* **139**, 254–266.
- Morris AK, Silk WK (1992) Use of a flexible logistic function to describe axial growth of plants. *Bulletin of Mathematical Biology* **54**, 1069–1081.
- Muday GK (2001) Auxins and tropism. *Journal of Plant Growth Regulation* **20(3)**, 226–243.
- Muday GK, DeLong A (2001) Polar auxin transport: controlling where and how much. *TRENDS in Plant Science* **6**, 535–542.
- Mullen JL, Ishikawa H, Evans ML (1998a) Analysis of changes in relative elemental growth rate patterns in the elongation zone of *Arabidopsis* roots upon gravistimulation. *Planta* **206**, 598–603.
- Mullen JL, Turk E, Johnson K, Wolverton C, Ishikawa H, Simmons C, Söll D, Evans ML (1998b) Root-growth behavior of the *Arabidopsis* mutant *rgr1*. *Plant Physiology* **118**, 1139–1145.
- Mullen JL, Wolverton C, Ishikawa H, Evans ML (2000) Kinetics of constant gravitropic stimulus response in *Arabidopsis* roots using a feedback system. *Plant Physiology* **123**, 665–670.
- Murphy R (2000) Some compartmental models of the root: Steady-state behavior. *Journal of Theoretical Biology* **207**, 557–576.

- Murphy R (2003) Steady-state water relations of soybean seedling roots. *Functional Plant Biology* **30**, 377–389.
- Neger F (1912) Spaltöffnungsschluß und künstliche Turgorsteigerung. *Berichte der Deutschen Botanischen Gesellschaft* **30**, 179–194.
- Neger F (1918) Wegsamkeit der Laubblätter für Gase. *Flora* **111**, 152–161.
- Niklas KJ (1992) Plant Biomechanics. An Engineering Approach to Plant Form and Function. The University of Chicago Press.
- Nobel PS (1999) Physicochemical & Environmental Plant Physiology. Academic Press, San Diego.
- Paciorek T, Zažímalová E, Ruthardt N, Petrášek J, Stierhof YD, Kleine-Vehn J, Morris DA, Emans N, Jürgens G, Geldner N, Friml J (2005) Auxin inhibits endocytosis and promotes its own efflux from cells. *Nature* **435**, 1251–1256, doi:10.1038/nature03633.
- Pages L, Jordan MO, Picard D (1989) A simulation model of the three-dimensional architecture of the maize root system. *Plant and Soil* **119**, 147–154.
- Parry G, Marchant A, May S, Swarup R, Swarup K, James N, Graham N, Allen T, Martucci T, Yemm A, Napier R, Manning K, King G, Bennett M (2001) Quick on the uptake: Characterization of a family of plant auxin influx carriers. *Journal of Plant Growth Regulation* **20**, 217–225, doi:10.1007/s003440010030.
- Passioura JB, Fry SC (1992) Turgor and cell expansion: Beyond the lockhart equation. *Australian Journal of Plant Physiology* **19**, 565–76.
- Pearcy RW, Krall JP, Sassenrath-Cole GF (1996) Photosynthesis in fluctuating light environment. In: Baker NR (Ed.), *Photosynthesis and the Environment* Kluwer Academic Press.
- Perbal G, Driss-Ecole D (2003) Mechanotransduction in gravisensing cells. *TRENDS in Plant Science* **8**, 498–504, doi:10.1016/j.tplants.2003.09.005.
- Perbal G, Jeune B, Lefranc A, Carnero-Diaz E, Driss-Ecole D (2002) The dose-response curve of the gravitropic reaction: a re-analysis. *Physiologia Plantarum* **114**, 336–342.
- Peters WS, Bernstein N (1997) The determination of relative elemental growth rate profiles from segmental growth rates. *Plant Physiology* **113**, 1395–1404.
- Pfitsch WA, Pearcy RW (1989) Daily carbon gain by *Adenocaulon bicolor* (asteraceae), a redwood understory forest herb, in relation to its light environment. *Oecologia* **80**, 465 – 470.

- Pieruschka R (2005) Effects of internal leaf structures on gas exchange of leaves. Ph.D. thesis, Universität Düsseldorf.
- Pieruschka R, Schurr U, Jahnke S (2005a) Lateral gas diffusion inside leaves. *Journal of Experimental Botany* **56**, 857–864.
- Pieruschka R, Schurr U, Jensen M, Wolff WF, Jahnke S (2005b) Lateral diffusion of CO<sub>2</sub> from shaded to illuminated leaf parts affects photosynthesis inside homobaric leaves. *New Phytologist* **In press**, doi: 10.1111/j.1469-8137.2005.01605.x.
- Potter D (1973) Computational Physics. John Wiley & Sons, London.
- Pritchard J (1994) The control of cell expansion in roots. *New Phytologist* **127**, 3–26.
- Pritchard J, Barlow PW, Adam JS, Tomos DA (1990) Biophysics of the inhibition of the growth of maize roots by lowered temperature. *Plant Physiology* **93**, 222–230.
- Pritchard J, Hetherington RP, Fry SC, Tomos DA (1993) Xyloglucan endotransglycosylase activity, microfibril orientation and the profiles of cell wall properties along growing regions of maize roots. *Journal of Experimental Botany* **44** (265), 1281–1289.
- Pritchard J, Winch S, Gould N (2000) Phloem water relations and root growth. *Australian Journal of Plant Physiology* **27**, 539–548.
- Prusinkiewicz P, Rolland-Lagan AG (2006) Modeling plant morphogenesis. *Current Opinion in Plant Biology* **9**, 83–88.
- Quarteroni A, Tuveri M, Veneziani A (2000) Computational vascular fluid dynamics: problems, models and methods. *Computing and Visualization in Science* **2**, 163–197.
- Roussel CJ, Roussel MR (2004) Reaction-diffusion models of development with state-dependent chemical diffusion coefficients. *Biophysics & Molecular Biology* **86**, 113–160, doi:10.1016/j.pbiomolbio.2004.03.001.
- Royle SJ, Murrell-Lagnado RD (2003) Constitutive cycling: a general mechanism to regulate cell surface proteins. *BioEssays* **25**, 39 – 46.
- Sachs J (1882) Über orthotrope und plagiotrope Pflanzenteile. *Arb Bot Inst Würzburg* **2**, 226–284.
- Sacks MM, Silk WK, Burman P (1997) Effect of water stress on cortical cell division rates within the apical meristem of primary roots of maize. *Plant Physiology* **114**, 519–527.

- Scharr H (2005) Optimal filters for extended optical flow. In: International Workshop on Complex Motion, LNCS 3417.
- Scheible WR, Lauerer M, Schulze ED, Caboche M, Stitt M (1997) Accumulation of nitrate in the shoot acts as a signal to regulate shoot-root allocation in tobacco. *The Plant Journal* **11**, 671–691.
- Schmundt D, Stitt M, Jähne B, Schurr U (1998) Quantitative analysis of local growth rates of dicot leaves at high temporal and spatial resolution, using image sequence analysis. *Plant Journal* **16**, 505–514.
- Selker JML, Sievers A (1987) Analysis of extension and curvature during the graviresponse in *Lepidium* roots. *American Journal of Botany* **74**, 1863–1871.
- Shabala SN, Newman IA (1997) Root nutation modelled by two ion flux-linked growth waves around the root. *Physiologia Plantarum* **101**, 770–776.
- Silk WK (1989) On the curving and twining of stems. *Environmental and Experimental Botany* **29**, 95–109.
- Silk WK (1992) Steady form from changing cells. *International Journal of Plant Sciences* **153**, S49–S58.
- Silk WK, Erickson RO (1978) Kinematics of hypocotyl curvature. *American Journal of Botany* **65**, 310–319.
- Silk WK, Lord EM, Eckard KJ (1989) Growth pattern inferred from anatomical records. *Plant Physiology* **90**, 708–713.
- Sitte P, Ziegler H, Ehrendorfer F, Bresinsky A (1998) Strasburger, Lehrbuch der Botanik., 34th Edition Gustav Fischer, Ch. 2.2, p. 371.
- Smirnow WI (1990) Lehrbuch der höheren Mathematik. Vol. II Verlag Harri Deutsch (VEB Deutscher Verlag der Wissenschaften), Berlin.
- Spollen WG, Sharp RE (1991) Spatial distribution of turgor and root growth at low water potentials. *Plant Physiology* **96**, 438–443.
- Stoer J, Burlisch R (2000a) Numerische Mathematik 1., 8th Edition Springer.
- Stoer J, Burlisch R (2000b) Numerische Mathematik 2., 4th Edition Springer.
- Swarup R, Friml J, Marchant A, Ljung K, Sandberg G, Palme K, Bennet M (2001) Localization of the auxin permease aux1 suggests two functionally distinct hormone transport pathways operate in the *Arabidopsis* root apex. *Genes & Development* **15**, 2648–2653.

- Swarup R, Kramer EM, Perry P, Knox K, Ottoline-Leyser HM, Haseloff J, Beemster GTS, Bhalerao R, Bennett MJ (2005) Root gravitropism requires lateral root cap and epidermal cells for transport and response to a mobile auxin signal. *Nature Cell Biology* **7**, 1057–1065.
- Taiz L, Zeiger E (1991) *Plant Physiology*, 1st Edition The Benjamin/Cummings Publishing Company, Ch. 16, pp. 405–407.
- Teale WD, Paponov IA, Ditengou F, Palme K (2005) Auxin and the developing root of *Arabidopsis thaliana*. *Physiologia Plantarum* **123**, 130–138.
- Turing AM (1952) The chemical basis of morphogenesis. *Philosophical Transactions of the Royal Society B* **237**, 37–72.
- Tyerman SD, Bohnert HJ, Maurel C, Steudle E, Smith JAC (1999) Plant aquaporins: their molecular biology, biophysics and significance for plant water relations. *Journal of Experimental Botany* **50**, 1055–1071.
- van der Weele CM, Jiang HS, Palaniappan KK, Ivanov VB, Palaniappan K, Baskin TI (2003) A new algorithm for computational image analysis of deformable motion at high spatial and temporal resolution applied to root growth. Roughly uniform elongation in the meristem and also, after an abrupt acceleration, in the elongation zone. *Plant Physiology* **132**, 1138–1148.
- Veytsman BA, Cosgrove DJ (1998) A model of cell wall expansion based on thermodynamics of polymer networks. *Biophysical Journal* **75**, 2240–2250.
- Vogel H (1995) *Gerthsen Physik*, 18th Edition Springer-Verlag, Heidelberg.
- von Caemmerer S (2000) *Biochemical Models of Leaf Photosynthesis*. CSIRO Publishing.
- von Caemmerer S, Farquhar GD (1981) Some relationships between the biochemistry of photosynthesis and the gas exchange of leaves. *Planta* **153**, 376–387.
- Wagner N (1937) Über die Mitosenverteilung in Wurzelspitzen bei geotropischen Krümmungen. *Planta* **27**, 751–773.
- Walter A, Feil R, Schurr U (2003) Expansion dynamics, metabolite composition and substance transfer of the primary root growth zone of *Zea mays* L. grown in different external nutrient availabilities. *Plant, Cell and Environment* **26**, 1451–1466.
- Walter A, Schurr U (2005) Dynamics of leaf and root growth: Endogenous control versus environmental impact. *Annals of Botany* **95**, 891–900.

- Walter A, Spies H, Terjung S, Küsters R, Kirchgeßner N, Schurr U (2002) Spatio-temporal dynamics of expansion growth in roots: automatic quantification of diurnal course and temperature response by digital image sequence processing. *Journal of Experimental Botany* **53**, 1–10.
- Wei C, Lintilhac PM, Tanguay JJ (2001) An insight into cell elasticity and load-bearing ability. Measurement and theory. *Plant Physiology* **126**, 1129–1138.
- Werner T, Motyka V, Laucou V, Smets R, van Onckelen H, Schmülling T (2003) Cytokinin-deficient transgenic *Arabidopsis* plants show multiple developmental alterations indicating opposite functions of cytokinins in the regulation of shoot and root meristem activity. *Plant Cell* **15**, 2532–2550.
- Wolverton C, Ishikawa H, Evans ML (2002a) The kinetics of root gravitropism: Dual motors and sensors. *Journal of Plant Growth Regulation* **21**, 102–112.
- Wolverton C, Mullen JL, Ishikawa H, Evans ML (2002b) Root gravitropism in response to a signal originating outside of the cap. *Planta* **215**, 153–157.
- Zieschang HE, Brain P, Barlow PW (1997) Modelling of root growth and bending in two dimensions. *Journal of Theoretical Biology* **184**, 237–246.
- Zieschang HE, Sievers A (1991) Gravitropism and the localization of its initiating cells in roots of *Phleum pratense* L. *Planta* **184**, 468–477.

# Publications

## Refereed

## Published

**Chavarría-Krauser A**, Schurr U (2004) A cellular growth model for root tips. *Journal of Theoretical Biology* **230** (1), 21–32.

**Chavarría-Krauser A**, Jäger W, Schurr U (2005) Primary root growth: a biophysical model of auxin-related control. *Functional Plant Biology* **32** (9), 849 – 862.

**Chavarría-Krauser A** (2006) Quantification of curvature production in cylindrical organs, such as roots and hypocotyls. To appear in *New Phytologist*.

Lai I, Scharr H, **Chavarría-Krauser A**, Küsters R, Wu J, Chou C, Schurr U, Walter A (2005) Leaf growth dynamics of two congener gymnosperm tree species reflect the heterogeneity of light intensities given in their natural ecological niche. *Plant Cell and Environment* **28**, 1496 – 1505

Matsubara S, Hurry V, Druart N, Benedict C, Janzik I, **Chavarría-Krauser A**, Walter A, Schurr U (2005) Nocturnal changes in leaf growth of *Populus deltoides* are controlled by cytoplasmic growth. *Planta*. DOI: 10.1007/s00425-005-0181-0

Schurr U, Blümmler P, **Chavarría A**, Christ M, Matsubara S, Nagel K, Scharr H, Walter A (2005) Mapping growth dynamics in a changing environment. *Journal of Experimental Botany* **56**(3), Suppl. 1, 127

## Submitted

**Chavarría-Krauser A**, Nagel KA, Scharr H, Palme K, Schurr U, Walter A (2006) Gravitropism in *Arabidopsis* is driven by two motors and the auxin efflux facilitator PIN3 regulates one of them. To be submitted to *The Plant Journal*.

## Poster

**Chavarría-Krauser A**, Nagel KA, Scharr H, Walter A, Jäger W, Schurr U (2004) A biophysical model for root growth: description of hormone-induced changes and

implications on the mechanisms of root gravitropism. Presented at *International Botanical Congress 2005* in Vienna.

# Index

- Auxin
  - distribution of, 41–42
  - transport model, 32–33, 35–36
  - transport, fountain model, 61–63
- Binormal  $\mathbf{b}$ , 50
- Cell division, 4
  - rate  $\theta$ , 36
- CO<sub>2</sub> assimilation rate, 82
- CO<sub>2</sub>- $\Phi_{PSII}$  calibration model
  - Hyperbolic, 81
  - Sigmoid, 81
- Cytokinin
  - role of in gravitropism, 78
  - transport model, 35–36
- Differential growth curvature rate
  - $DGCR$ , 51–52
  - determination of, 67
  - distribution of, 72–77
- Differential growth torsion rate
  - $DGTR$ , 55
- Expansins, 29–30
- Fick’s law, 2, 9
  - extended, 11
- Homo- and heterobaricity, 79–80
  - effect on photosynthesis, 88–89
- Lockhart Eq., 6
- Natural coordinate system, 50–51
- Net CO<sub>2</sub> exchange rate,  $NCER$ , 87
  - lateral diffusion effect on, 87–88
- Normal  $\mathbf{n}$ , 50
- Osmometer Eq., 6
- Ratio function  $\omega$  of auxin and cytokinin, 26
- Relative Elemental Growth Rate
  - $REGR$ , 5
  - and curvature, 49–51, 64–65
  - average of in root meristem, 36–37
  - determination of, 66–67
  - distribution of, 24–25, 39, 72–77
- Relative Growth Rate,  $RGR$ , 4–5
  - difference to  $REGR$ , 5
  - divergence definition of, 5
  - time derivative definition of, 5
- Root growth zone, 62, 64
- Spatio-temporal distributions, 74–77
  - denoising of, 67–68
- Species conservation Eq., 1, 8
  - applied to cell growth, 10
  - example of spherical cell, 17
  - applied to lateral CO<sub>2</sub> diffusion in leaves, 84
  - applied to root growth, 35
- Tangent  $\mathbf{t}$ , 50
- Turgor pressure  $p$ , 3
  - “working”, 6
  - approximated, 27
  - distribution of, 44
  - recovery in spherical cell, 18
- Wall extensibility, 29–30
  - distribution of, 45–46





